Stony Brook University

Characterization of Noble Metal Nanocatalysts from First-Principles Calculations and Classical Force Field Simulations

A Dissertation presented

by

Shangmin Xiong

to

The Graduate School

in Partial Fulfillment of the

Requirements

for the Degree of

Doctor of Philosophy

in

Materials Science and Engineering

Stony Brook University

December 2015

Stony Brook University

The Graduate School

Shangmin Xiong

We, the dissertation committee for the above candidate for the

Doctor of Philosophy degree, hereby recommend acceptance of this dissertation

Yan Li - Dissertation Advisor
Associate Editor, American Physical Society
Adjunct Assistant Professor, Institute for Advanced Computational Science

Dilip Gersappe, Chairperson of Defense
Professor, Department of Materials Science and Engineering

Alexander Orlov, Second Member
Associate Professor, Department of Materials Science and Engineering

Gary Halada, Third Member
Associate Professor, Department of Materials Science and Engineering

Qin Wu, Outside Member
Staff Scientist, Brookhaven National Laboratory

This dissertation is accepted by the Graduate School

Charles Taber
Dean of the Graduate School

Abstract of the Dissertation

Characterization of Noble Metal Nanocatalysts from First-Principles Calculations and Classical Force Field Simulations

by

Shangmin Xiong

Doctor of Philosophy

in

Materials Science and Engineering

Stony Brook University

2015

Nanoparticles (NPs) are useful in a wide variety of applications, such as sensors, catalysis, and biomedical materials. NPs often exhibit properties that are distinctively different from bulk materials, which are largely determined by their size, shape and surface modifications. Characterizing NP structures remains a challenge due to their small size, low symmetry, and the presence of defects and surface disorders, which often falls beyond the scope of experimental techniques. Work in this thesis focuses on characterizing bare and supported noble metal NPs towards a fundamental understanding of their structural, energetic and electronic properties, by a combined density function theory (DFT) and classical force field (FF) study.

The first half of the thesis is devoted to the study of the size-, shape- and temperature dependence of unsupported noble metal NPs. A series of nm-sized Au NPs were investigated using classical FF simulations, and the performance was evaluated by DFT calculations for small clusters up to 249 atoms. The trend of cohesive energy and bond length distribution as a function of size were extracted and analyzed. Larger NPs (3nm-10nm) were studied using the classical FF simulations with the embedded atom method (EAM) potentials. In particular, simulated annealing was performed to sys-

tematically study the temperature effects on structural features of crystalline and amorphous NPs. The thermal behaviors of spherical and cubic NPs were characterized by coordination numbers, mean interatomic distances and radial distribution functions.

In the second half of this thesis, we moved on study supported Pt clusters on semiconductor CdS surface by a comprehensive DFT study, which was motivated by the significantly enhanced photocatalytic activity of hydrogen production experimentally observed upon adsorption of Pt clusters on CdS. The trends of cohesive energy, bond length distribution, and excitation energy (e.g. ionization potential and electron affinity) as a function of size (10 atoms to 140 atoms) and shape (2D bilayer or 3D truncated octahedron) were extracted and analyzed for a series of sub-nm and nm-sized Pt NPs. The adsorption characteristics and interface electronic structure of a single Pt atom, a 2D Pt_{19} cluster, and a 3D Pt_{38} cluster on the nonpolar $CdS(10\bar{1}0)$ surface were investigated. Severe structural deformation in the supported cluster and the substrate were observed, accompanied by significant modifications of the surface electronic structure and shift in local surface potential. A comprehensive picture of the structural and electronic interactions at the metal NP-semiconductor interface was obtained towards better understanding of the role of supported NPs in photocatalytic reactions.

To my family...

Table of Contents

Contents

List of Figures

List of Tables

List of Abbreviations

NP: Nanoparticle
DFT: Density Functional Theory
FF: Force Field
EAM: Embedded Atom Method
MD: Molecular Dynamics
BO: Born-Oppenheimer
HK: Hohenberg-Kohn
KS: Kohn-Sham
LDA: Local Density Approximation
GGA: Generalized- Gradient Approximation
PBE: Perdew-Burke-Ernzerhorf
TB: Tight Binding
TB-SMA: Second Moment Approximation to Tight Binding
FS: Finnis-Sinclair
PES: Potential Energy Surface
UFF: Universal Force Field
FCC: Face Centered Cubic
XRD: X-Ray Diffraction
TEM: Transmission Electron Microscopy
RDF: Radial Distribution Function
PAW: Projected Augmented Wave
SOC: Spin-Orbit Coupling

Acknowledgements

I would like to take this opportunity to show my sincere appreciation to all the people who helped me throughout my graduate study. First and foremost, I would like to thank my advisor Dr. Yan Li for her generous guidance and support. Her expertise and understanding made it possible for me to work on interesting topics that I would never have a chance to get in touch with before. I have always been inspired by her enthusiasm and dedication, not only to research but also to family. She sets a great example for me.

I would like to express my great appreciation to Prof. Robert Harrison and IACS for the financial support throughout this year. I would like to thank my co-advisor and collaborator, Prof. Alexander Orlov, for his guidance and inspiring discussions. I learned a lot and enjoyed all the discussions with him and his student Qiyuan Wu. I also thank my committee members, Prof. Dilip Gersappe, Prof. Gary Halada and Dr. Qin Wu for all the help and advice. I am grateful to our collaborators, Prof. Cevdet Noyan and his student Dr. Hande Öztürk from Columbia University, Dr. Hanfei Yan, Dr. Sanjit Ghosh from Brookhaven National Laboratory and his student Christopher Wright for useful discussions. I also thank Eric Isaacs for helping to start the DFT project at the very beginning.

In addition, I am grateful to my friends Dr. Hualu Zheng, Dr. Lina Zhang, Dr. Liudi Zhang, Xiaoxi Zhu, Xia Lu and Wei Li for their help and support. I enjoyed the time with them and would like to thank them for being there whenever I needed a hand.

Last but not least, I would like to thank my parents for their everlasting understanding and support. I am so proud of being their daughter.

1 Introduction

Noble and transition metal nanoparticles (NPs) with structures at the nanoscale often exhibit unique optical, electronic, or mechanical properties that are distinctively different from the bulk materials, which stimulate the research interests in nanotechnology. They are useful in a wide variety of applications such as imaging, catalysis, biotechnology, and energy conversion due to their tunable properties depending on size, shape, crystallinity and chemical composition.[3, 4, 5] Determining the structure of a nanoparticle at the atomic level is vital in understanding the structure-properties relationship and further tuning the materials properties for optimal performance.

There are two challenges associated with the batch production and characterization of the NPs. First, it is difficult to synthesize identical NPs in experimental process. The particles produced in the batch reactions can vary in size, shape, surface morphology and defects, resulting in different physical and chemical properties. For example, it is possible that only a small portion of the particles produced for catalysis can be highly efficient and actually promote the reaction. Therefore, structural characterization is essential to distinguish between the performing and the non-performing particles, and in turn guide the synthesis to produce only the desirable particles. Second, while robust techniques, such as X-ray diffraction, have been developed to solve the structure problem of the bulk crystals, such robustness often breaks down when the size goes down to nanoscale.[6] Local structure of a nanomaterial can be extracted from experimental data, such as neutron and X-ray total scattering, and spectroscopy methods.[7] Spectroscopy methods, such as transmission electron microscopy (TEM) techniques, can be useful to examine the NPs one by one. However, it is time consuming and inefficient. On the other hand, the neutron and X-ray scattering techniques provide the structural information based on averaging over all particles. By doing inverse modeling using these experimental information (e.g. Reverse Monte Carlo method), one can generate the solutions of nanostructures. However, such structural solution is hardly unique, and sometimes even not physically plausible. Therefore, computational simulations, including classical and *ab initio* methods, are essential to provide alternative solutions to these two challenges.

In collaboration with experts in X-ray diffraction techniques, we combine computational simulations of noble metal NP structures and theoretical modeling of X-ray diffraction pattern to provide insight on structural solution of nanoparticles. In Chapter 3, we focus on classical molecular dynamics sim-

ulations of single crystalline Au NPs of 3 nm to 10 nm in diameter to probe their size- and shape-dependent temperature effects. As metal nanocatalysts often undergo temperature changes in annealing processes and catalytic reactions, it is important to study the overall expansion/contraction and the surface reconstructions at finite temperatures. Theoretically, thermal expansion is a direct measurement of the effect of anharmonicity, which plays a role in thermal vibration.[8, 9] In isotropic close-packed crystals, thermal expansion is only affected by the atomic vibration. For nanoparticles, the low coordination at the surface also changes the thermal expansion.[10] Moreover, an additional contribution from electronic excitations changes the thermal expansion for small Au NPs. It was found in experiments that thermal expansion occurs at low temperatures and thermal contraction occurs at temperatures higher than a transition point for bare and supported Au NPs of 4 nm or smaller.[11, 12] In addition to the effect of thermal expansion, higher kinetic energy at higher temperature provides an additional driving force for structural deformation and reformation, especially at the surface. High resolution TEM studies of spherical Au NPs about 5 nm in diameter indicate a clear surface reconstruction from high-index planes to low-index facets at annealing temperatures.[13] As the surface energies of the (100) and (111) facets are among the lowest in face centered cubic (FCC) crystalline, they are the preferred planes on constructing the nanoparticles.[14] At annealing temperature, the surface becomes (100) and (111) facets dominated, and thus the shape of the spherical NPs evolves from near sphere to truncated octahedron-like.[13] All these temperature effects will be investigated using computational simulations, so that we may evaluate the performance of the simulations according current experimental data, and provide further guidance and feed back to experiments from the results predicted in the simulations.

Ideally, first-principles calculations using the quasi-harmonic approximation can be a reliable method to study thermal expansion on nanoparticles, especially when electronic interactions are heavily involved at small sizes. However, such calculations are extremely computational demanding as size goes beyond hundreds of atoms. Therefore, classical molecular dynamics (MD) simulations at finite temperature were performed using a recently developed EAM potential [15] to study the thermal effects of spherical and cubic 3 nm, 5 nm and 10 nm Au NPs. Structural optimizations of small Au clusters up to 249 atoms using DFT were carried out to provide references for the FF simulations. By comparing with DFT and experimental results,

we aim to evaluate the performance of FF potentials and probe the lower size limit of FF simulations, so as to provide realistic models for X-ray forward simulations and to characterize Au NPs at this size range.

While classical FF simulations can be useful and reliable for larger NPs and bulk, first-principles calculations are essential to investigate the geometries and electronic structures of small-sized NPs and interfaces. Subnanometer- and nanometer-sized noble metal nanoparticles are of special research interest due to their applications in photocatalytic reactions. New photocatalysts are being developed to achieve improved quantum efficiency for hydrogen evolution. Since expensive noble metals, such as Pt, Rh and Au, are still crucial as the electrodes in the reaction, one strategy of developing new catalysts is to use metal nanoparticles as co-catalysts to increase the conversion rate and to reduce the total cost. It has been recently reported by Prof. Orlovs group at Stony Brook University that semiconducting CdS nanorods or nanoparticles decorated with subnanometer- and nanometer-sized Pt clusters showed promising applications in H_2 production under visible light.[5] Interestingly, the catalytic activity for Pt clusters on CdS was observed to be significantly enhanced for a particular cluster size, which was proposed to contribute from the energy level alignment of the Pt cluster and the CdS. Due to the unavailability of the experimental data on the sub-nm Pt clusters, theoretical studies, such as DFT calculations, can play an essential role of investigating the adsorption geometry of the supported clusters and probing into the interactions at the interface on the atomic and electronic scale. In Chapter 4, we carried out DFT studies of CdS supported sub-nm Pt clusters in an attempt to understand the structural and electronic interactions at the cluster/semiconductor interface and obtain new insights into the role of Pt in photocatalytic H_2 production.

A systematic investigation of unsupported 2D bilayer and 3D Pt clusters up to 1.5 nm yielded similar trends on their structural, energetic and electronic properties as functions of the cluster size. Detailed adsorption studies of a single Pt atom, a 2D Pt_{19} cluster and a 3D Pt_{38} cluster on the nonpolar CdS($10\bar{1}0$) surface revealed that both the cluster size/shape and the adsorption configuration have considerable influence on the surface structure, adsorption strength and other interface characteristics. Strong bonding interactions occur at the cluster/semiconductor interface, leading to severe structural deformation of the substrate and the adsorbed clusters, as well as modification of the electronic structure. In addition, significant charge redistribution occurs at the interface and results in shift of the local surface

potential. Our work highlights the importance of explicitly treating the interface with realistic structural models in order to obtain an accurate picture of the structural and electronic interactions at the interface and understand the observed enhancement in photocatalytic activities. [16]

2 Theory

This chapter focus on the theory and the approximations that will be applied in the thesis. We will give a broad introduction to the density functional theory in the first subsection, mostly following Ref.[17]. In the second subsection, we focus on the concepts in the classical force field simulation. Development of the FF potentials will be briefly introduced.

2.1 Density Functional Theory

The density functional theory (DFT) has been the most successful approach for quantum mechanical simulation of periodic system in the past decades, and its application now ranges from atoms, molecules and surfaces to solid and quantum and classical fluids. The simplest form of the time-independent Schrödinger equation is $H\Psi = E\Psi$ where $\hat{H}$ is the Hamiltonian, E is the total energy of the system, and Ψ is the wave function.

In the most general form, the Hamiltonian of interacting particles is

$$\begin{aligned}\hat{H} = -\frac{\hbar}{2m_e}\sum_i \nabla_i^2 + \sum_{i,I}\frac{Z_I e^2}{|\mathbf{r}_i - \mathbf{R}_I|} + \frac{1}{2}\sum_{i\neq j}\frac{e^2}{|\mathbf{r}_i - \mathbf{r}_j|} \\ - \sum_I \frac{\hbar}{2M_I}\nabla_I^2 + \frac{1}{2}\sum_{I\neq J}\frac{Z_I Z_J e^2}{|\mathbf{R}_I - \mathbf{R}_J|} \\ = \hat{T}_e + \hat{V}_{eI} + \hat{V}_{ee} + \hat{T}_I + \hat{V}_{II} \quad (1)\end{aligned}$$

where i and j are the ith and jth electrons, I and J are the Ith and Jth nuclei in the system, m_e and M_I are the mass of the electron and the nuclei, respectively, and Z_I is the nuclear charge. The first and the fourth terms, $\hat{T}_e$ and $\hat{T}_I$, describe the kinetic energy of the electrons and the nuclei in the system, respectively. The second term $\hat{V}_{eI}$ describes the potential due to the electrostatic interaction of the electrons with the nuclei. The third and the fifth terms are the Coulomb interactions between the electrons and the nuclei, respectively.

The many body interactions become complicated as the number of particles (electrons and nuclei) increases, making it impossible to solve the equation exactly. Therefore, the Born-Oppenheimer (BO) approximation, also called the adiabatic approximation, is applied to further simplify the Schrödinger equation. Due to the significant difference in mass between the

electrons and the nuclei, the kinetic energy proportional to the inverse mass of nuclei is small compared to the other terms. As a result, the kinetic energy of the nuclei can be neglected, or separated from the other Hamiltonians as a parameter. From this point, only the Hamiltonian for the electrons will be considered, and the electronic Hamiltonian is

$$\hat{H} = \hat{T}_e + \hat{V}_{ext} + \hat{V}_{int} + E_{II} \tag{2}$$

where the first term is the kinetic energy operator for the electrons, the second term is the external potential on the electrons due to the nuclei, the third term is the electron-electron interaction, and the last term includes the interaction of nuclei and any other terms that are not electron-related.

2.1.1 Homogeneous Electron Gas

Thomas and Fermi [18, 19] introduced the first idea of density functional theory in 1927. In this approximation, the electrons in the system were treated as free electron gas with uniform density, and the kinetic energy of the system was approximated as a functional of the density. The original Thomas-Fermi method neglected the exchange and correlations. Dirac [20] then introduced the approximation for local exchange to the energy functional

$$E_{TF}[n] = C_1 \int d^3r n(\mathbf{r})^{\frac{5}{3}} + \int d^3r V_{ext}(\mathbf{r}) n(\mathbf{r}) + C_2 \int d^3r n(\mathbf{r})^{\frac{4}{3}} + \frac{1}{2} \int d^3r d^3r' \frac{n(\mathbf{r}) n(\mathbf{r}')}{|\mathbf{r} - \mathbf{r}'|} \tag{3}$$

where the first term corresponds to the local Thomas-Fermi approximation to the kinetic electron energy with $\mathrm{C}_1 = \frac{3}{10}(3\pi^2)^{\frac{2}{3}}$, the second term is the external field, the third term is the local exchange with $\mathrm{C}_2 = -\frac{3}{4}(\frac{3}{\pi})^{\frac{1}{3}}$, and the last term is the electrostatic Hartree energy.

Thomas-Fermi-Dirac density functional formalism set the foundation of the density functional theory, which solves the energy as a functional of a smooth electron density. This approximation was remarkably simpler than the full many-body Schrödinger equation and thus lowered the computational cost significantly. The formulation of this idea was further developed with the Hohenberg-Kohn theorems followed by the Kohn-Sham ansatz, making DFT applicable to various systems.

2.1.2 Hohenberg-Kohn Theorems

Hohenberg and Kohn (HK) developed a formulation as an exact principle for the ground state energy of many-body systems. HK theorems can be stated as the following:

Theorem 1: For a system of interacting particles in an external potential $\mathrm{V_{ext}}(\mathbf{r})$, this potential term is uniquely determined by the ground state particle density, $\mathrm{n_0}(\mathbf{r})$.

Theorem 2: The energy $E[n]$ as a universal functional of the density $n(\mathbf{r})$ can be defined for any external potential $\mathrm{V_{ext}}(\mathbf{r})$. For any particular external potential, the global minimum value of this functional is the exact ground state energy of the system, and the exact ground state density $n_0(\mathbf{r})$ is the density that minimizes the functional.

The theorems demonstrate that the ground state density uniquely determines the external potential, and thus fully determines the hamiltonian. Therefore, the many-body wavefunctions for both ground and excited states are determined. Then all properties of the system are determined completely from the ground state density. If the exact form of the functional of the energy based on the ground state density is known, the exact ground state density and energy will be solved. However, HK theorems did not provide any exact form of the electronic energy functional.

2.1.3 Kohn-Sham Ansatz

To tackle the problem of the electronic energy functional, Kohn and Sham introduced an approach to replace the interacting many-body system with a system of non-interacting electrons, with a Hamiltonian of an effective local potential. The exact ground state electron density n_0 was represented by the ground state density of an auxiliary system of non-interacting particles, so that the hamiltonian can be solved more easily. In this ansatz, the many-body problem is replaced by the independent particle problem for the non-interacting system, which can be exactly solved. Then the many-body interacting terms can be included in an exchange-correlation functional. The accuracy of the solution for the ground state density and energy is then limited only by the approximation in the exchange-correlation functional.

The Kohn-Sham (KS) auxiliary hamiltonian is defined as (given in Hartree

atomic units $\hbar = m_e = e = 4\frac{\pi}{\epsilon_0} = 1$)

$$\hat{H}^{\sigma}_{aux} = -\frac{1}{2}\nabla^2 + V^{\sigma}(\mathbf{r}) \tag{4}$$

where the kinetic and the potential parts are separated.

For KS ansatz, it can be stated that the Kohn-Sham potential of the interaction between electron densities, V_{KS}, can be exactly determined if the ground state density of the system is known. Then the Kohn-Sham potential determines all the states of the system, in which the minimum would be the ground state. Then the ground state of non-interacting particles directly leads to the ground state density, which closing the cycle of HK theorems.

The Kohn-Sham equation of the ground state energy functional is in the form

$$E_{KS} = T_s[n] + \int d\mathbf{r} V_{ext}(\mathbf{r}) n(\mathbf{r}) + E_{Hartree}[n] + E_{II} + E_{xc}[n] \tag{5}$$

where $T_s[n]$ is the independent-particle kinetic energy, V_{ext} is the external potential due to the nuclei and any other applied fields, $E_{Hartree}[n]$ is the classical Coulomb interaction energy of the electron density interacting with itself, E_{II} is the interaction between the nuclei, and $E_{xc}[n]$ is the exchange-correlation energy. Thus the sum of the terms including V_{ext}, $E_{Hartree}[n]$, and E_{II} is well defined.

All many-body interactions from the exchange and correlations of the electron densities are embedded into $E_{xc}[n]$ term, which can be written in terms of the Hohenberg-Kohn functional as

$$\begin{aligned} E_{xc}[n] &= F_{HK}[n] - (T_s[n] + E_{Hartree}[n]) \\ &= \left\langle \hat{T} \right\rangle - T_s[n] + \left\langle \hat{V}_{int} \right\rangle - E_{Hartree}[n] \end{aligned} \tag{6}$$

where $[n]$ is a functional of the density $n(\mathbf{r}, \sigma)$. If $E_{xc}[n]$ term were known exactly, then the exact ground state energy and density of the system would also be determined by solving the KS equations for independent-particles.

Applying the variational equation to E_{KS} to solve for the ground state energy of the system

$$\frac{\delta E_{KS}}{\delta \psi_i^{\sigma *}(\mathbf{r})} = \frac{\delta T_s}{\delta \psi_i^{\sigma *}(\mathbf{r})} + [\frac{\delta E_{ext}}{\delta n(\mathbf{r}, \sigma)} + \frac{\delta E_{Hartree}}{\delta n(\mathbf{r}, \sigma)} + \frac{\delta E_{xc}}{\delta n(\mathbf{r}, \sigma)}] \frac{\delta n(\mathbf{r}, \sigma)}{\delta \psi_i^{\sigma *}(\mathbf{r})} = 0 \tag{7}$$

From the definition of the independent electron kinetic energy,

$$\frac{\delta T_s}{\delta \psi_i^{\sigma *}(\mathbf{r})} = -\frac{1}{2}\nabla^2 \psi_i^{\sigma}(\mathbf{r}) \tag{8}$$

and the electronic density is

$$\frac{\delta n^{\sigma}(\mathbf{r})}{\delta \psi_i^{\sigma *}(\mathbf{r})} = \psi^{\sigma}(\mathbf{r}) \tag{9}$$

Applying the Lagrange multiplier method, $\delta[\langle\psi|\hat{H}|\psi\rangle - E\langle\psi|\psi\rangle - 1] = 0$, 7 leads to the Schrödinger-like Kohn-Sham equation:

$$(H_{KS}^{\sigma} - \epsilon_i^{\sigma})\psi_i^{\sigma}(\mathbf{r}) = 0 \tag{10}$$

and thus the effective Hamiltonian H_{KS} is

$$\begin{aligned} H_{KS}^{\sigma}(\mathbf{r}) &= -\frac{1}{2}\nabla^2 + V_{KS}^{\sigma}(\mathbf{r}) \\ &= -\frac{1}{2}\nabla^2 + V_{ext}(\mathbf{r}) + \frac{\delta E_{Hartree}}{\delta n(\mathbf{r},\sigma)} + \frac{\delta E_{xc}}{\delta n(\mathbf{r},\sigma)} \\ &= -\frac{1}{2}\nabla^2 + V_{ext}(\mathbf{r}) + V_{Hartree}(\mathbf{r}) + V_{xc}^{\sigma}(\mathbf{r}) \end{aligned} \tag{11}$$

The Kohn-Sham density functional theory is an exact theory up to this point. In principle, it is possible to solve the interacting many-body problem if one knows all the density functionals of the Hamiltonian in Eqn. 11. Therefore, DFT is an *ab initio* theory.

2.1.4 Exchange and Correlation Functionals

The exchange-correlation energy expressed as a functional of the density $E_{xc}[n]$ is not known explicitly, and the development of approximations to these functionals is still a field in progress. E_{xc} is expressed in terms of the energy density ϵ_{xc}, a functional of the electron density:

$$E_{xc}[n] = \int d\mathbf{r} n(\mathbf{r}) \epsilon_{xc}([n], \mathbf{r}) \tag{12}$$

This section is devoted to several relevant approximate functionals, for example, the local density approximation (LDA) and different flavors of generalized-gradient approximations (GGAs).

Local density approximation (LDA)

Local density approximation [21] is the simplest approximation to the energy density. In LDA, ϵ_{xc} is assumed to be identical to the homogeneous electron gas energy density:

$$E_{xc}^{LDA}[n] = \int d^3r n(\mathbf{r}) \epsilon_{xc}^{hom}[n(\mathbf{r})] \tag{13}$$

For polarized systems, the LDA sets $\epsilon_{xc}^{hom}[n(\mathbf{r})]$ as $\epsilon_{xc}^{hom}[n^{\uparrow}(\mathbf{r}), n^{\downarrow}(\mathbf{r})]$. For unpolarized system, the LDA sets $n^{\uparrow}(\mathbf{r}) = n^{\downarrow}(\mathbf{r}) = n(\mathbf{r})/2$.

This approximation works best for solids that resemble homogeneous electron gas, with a smoothly varying electronic density. As a result, LDA fails for molecular systems, where the electron density goes to zero outside the molecular radius. For condensed matter, the accuracy of the energetics estimated from LDA is rather poor, although results from LDA give reasonable structural information.

Generalized gradient approximation (GGA)

The LDA has stimulated ideas for constructing functionals with improvement. To account for the non-homogeneity of the electron density in real systems, the gradient of density is considered in the generalized-gradient approximation (GGA). A Taylor-like expansion is applied to include the electronic density, $n(\mathbf{r})$, and the gradient of the density, $\nabla n(\mathbf{r})$ in the exchange and correlation energy density functional. A generalized form of GGA is

$$E_{xc}^{GGA}[n] = \int d^3r n(\mathbf{r}) \epsilon_{xc}^{GGA}[n(\mathbf{r}), \nabla n(\mathbf{r})] \tag{14}$$

By definition, GGA functionals work better for non-homogeneous systems. This form is further developed as

$$E_{xc}^{GGA}[n] = \int d^3r n(\mathbf{r}) \epsilon_{x}^{hom}[n(\mathbf{r})] F_{xc}[n(\mathbf{r}), \nabla n(\mathbf{r})] \tag{15}$$

where ϵ_x^{hom} s the exchange energy density functional of the electron gas, and F_{xc} is a dimensionless term. The lowest order terms in the Taylor-like expansion of F_x have been calculated analytically [22, 23]

$$F_x = 1 + \frac{10}{81} s_1^2 + \frac{146}{2025} s_2^2 + ... \tag{16}$$

where s_1 and s_2 are proportional to the first and the second order fractional variation in density normalized to the average distance between electrons. Wide variety of the forms for F_x have been proposed.

GGA methods are of the most popular methods used in heterogeneous systems. The performance of GGA is superior compared with LDA for non-periodic systems. It provides structures, energetics and electronic structures for such systems with a good accuracy. Therefore, GGA will be adopted in this thesis, where noble metals (Au or Pt), cadmium sulfide, and their interfaces will be studied. One of the most popular generalized gradient approximations used in the applications of the density functional theory, PBE [24] by Perdew-Burke-Ernzerhof, will be used as the standard GGA functional in Chapter 4.

2.1.5 Pseudopoentials

The wavefunctions of all-electron potential require enormous computational cost to solve. As non-valence core electrons are strongly bonded to the nuclei and usually chemically inert, the pseudopotential approximation replaces the explicit treatment of the inert core electrons and the nucleus with a pseudopotential, or an effective potential to reduce the computational cost.[25] The approximation describes the active valence electrons by pseudo-wavefunctions explicitly, and treats the rest of the atom within a certain cutoff radius as rigid non-polarized cores together with the frozen core electrons. The orbitals are strong oscillations near the nuclei and thus require a large number of plane waves to describe these oscillations if all electrons are involved. This method allows remarkably fewer wavefunctions to be calculated, and thus make it practical to apply plane-wave basis sets. Pseudopotential with large cutoff radius is considered soft, leading to faster convergence and less accuracy.

Norm-conserving and ultrasoft first-principle pseudopotentials are the most common forms applied in plane-wave DFT codes. Norm-conserving pseudopotential is constrained so that the norm of each pseudo-wavefunction is identical to the corresponding all-electron wavefunction outside the cutoff radius.[26] The norm-conserving pseudopotential will be applied in Chapter 4 for all the systems investigated.

2.1.6 Structural Relaxation

Kohn-Sham equations are solved in a self consistent way. An initial guess of the electronic density is applied to obtain the external potential. The densities were generated by either orthogonal single electron plane waves, or localized atomic orbitals. The simulation package VASP [27, 28] employed in

Chapter 4 is based on the former approach. Then the ground state from KS equations are determined using this external potential. The new electronic density is deducted from the ground state, and compared to the initial guess. The new density is used as the input to solve the KS equations again, until the output density is consistent with the input density within a small tolerance criteria set by the user.

From the output density, the ground state energy of the system is determined, then the forces on the system can be calculated. The force on the atoms as a function of energy is

$$F_I = -\frac{\partial E}{\partial \mathbf{R}_I} = -\langle\psi|\frac{\partial \hat{H}}{\partial \mathbf{R}_I}|\psi\rangle - \langle\frac{\partial \psi}{\partial \mathbf{R}_I}|\hat{H}|\psi\rangle - \langle\psi|\hat{H}|\frac{\partial \psi}{\partial \mathbf{R}_I}\rangle - \frac{\partial E_{II}}{\partial \mathbf{R}_I} \quad (17)$$

The ground state density corresponds to the total energy minimum, and the electron-electron interaction contributions leads to cancellation of the middle terms. The remaining terms are the external potential and ion-ion interactions, which explicitly depend on the ion positions. Then the force becomes

$$F_I = -\int d^3 r n(\mathbf{r}) \frac{\partial V_{ext}(\mathbf{r})}{\partial \mathbf{R}_I} - \frac{\partial E_{II}}{\partial \mathbf{R}_I} \quad (18)$$

Once the forces are determined for initial ionic positions, the forces can be then minimized along the energy gradient. As the force minimized, the atomic positions are updated to minimize the total energy. The energy of the system is considered converged, and the structure relaxed, until the forces acting on atoms are within a tolerance criteria.

2.2 Classical Force Field and Molecular Dynamics Simulations

First principal based method, such as DFT, can provide a good model to represent the interatomic forces, energetics, structures and electronic structures in a system of a reasonable size and time-scale. Under the current computational condition, it is affordable to study a system consisting up to several hundreds of atoms and a time scale of the order of hundreds of picoseconds. However, the size and/or time-scale of a real world system often go beyond the current limitation of DFT. Therefore, an approximation without solving Schrödinger equation for electrons is needed. The empirical, or classical force field (FF) based methods ignore the motions of the electrons and describes

the nuclear positions only, which sacrifice the accuracy comparing to DFT while allow to model systems and processes containing orders of magnitudes more atoms at a time scale of nanoseconds or even microseconds. The quality of a force field needs to be validated either using experiments, or by higher level of simulation methods such as DFT.

In the first part, I will briefly discuss the basic concepts of the FF. In the second part, I will specifically describe the potentials that are possibly suitable to investigate pure or alloy metal NPs.

2.2.1 Force Field

A classical force field, or potential energy function, is an mathematical expression describing the ground state potential energy as a function of the position of the particles (atoms). In the classical approximation, a system is defined by the position $\mathbf{r}$ and the momenta $\mathbf{p}$ of the atom:

$$\mathbf{r}^N = (x_1, y_1, z_1, ..., x_N, y_N, z_N) \tag{19}$$

$$\mathbf{p}^N = (p_{x,1}, yp_{y,1}, p_{z,1}, ..., p_{x,N}, p_{y,N}, p_{z,N}) \tag{20}$$

The Hamiltonian of a classical system is a function that describes the energy of a configuration:

$$H(\mathbf{p}^N, \mathbf{r}^N) = K(\mathbf{p}^N) + U(\mathbf{r}^N) \tag{21}$$

where the kinetic energy $K(\mathbf{p}^N)$ is simply a function of the momenta:

$$K(\mathbf{p}^N) = \sum_i^N \frac{|\mathbf{p}_i|^2}{2m_i} \tag{22}$$

and the potential energy $U(\mathbf{r}^N)$ depends on the positions. The classical potential energy is a simplified approximation to the ground state energy which would be the exact solution of Schrödinger equation for all the nuclei and the electrons in the system.

U consists of a summation of two terms, intramolecular contributions involving single atoms, and the intermolecular contributions involving pairs of atoms, triples of atoms, and so on. The intramolecular term describes local contribution (bonded forces) due to bond stretching, bond angle bending, and dihedral torsions, as shown in Eqn. 23 as the first three terms, respectively.

The intermolecular term consists of non-bonded forces associated with the electrostatic interactions and van der Waals interaction. It includes two-, three- and many-body interactions that require loop over pairs, triples and so on, and therefore require the computational cost scales as N^2, N^3, and higher orders, respectively, which make the simulation prohibitive as the scaling goes beyond N^3. Simplified intermolecular terms include the Coulombic interactions, and the repulsive and Van der Waals interaction described by pairwise potentials, as shown in Eqn. 23 as the last two terms, respectively. In general, a minimal form of the potential energy function would be:

$$U(\mathbf{r}) = \sum_{bonds\, i} \frac{1}{2} k_b (d_i - d_0)^2 + \sum_{angles\, j} \frac{1}{2} k_a (\theta_i - \theta_0)^2 + \sum_{torsions\, k} [\sum_n c_{k,n}[1 + cos(\omega_k n + \gamma_k)] + \sum_{elec\, ij} \frac{q_i q_j}{4\pi\epsilon_0 r_{ij}} + \sum_{L-J\, ij} 4\epsilon_{ij}[(\frac{r_{ij}}{\sigma_{ij}})^{-12} - (\frac{r_{ij}}{\sigma_{ij}})^{-6}] \quad (23)$$

where the bond distances d_i, angles θ_j, torsions ω_k and pairwise distances r_{ij} are functions of $\mathbf{r}^N$. The repulsive force and Van der Waals interaction is described by Lennard-Jones (L-J) potential in a simple form as shown in the last term in Eqn. 23. Reasonable values of the constants, equilibrium bond distance d_0, spring constants k_a and k_b, electric permittivity ϵ_0, can be obtained or estimated from experimental values. Of the terms included here, the last two pairwise sums, Coulomb potential and Lennard-Jones potential, respectively, are the most computationally expansive parts, which scale as N^2 instead of N in the other sums.

Lennard-Jones potential [29] describes the pairwise interaction in a neutral system with a weakly attractive term at long distances and a strongly repulsive term when the atoms or molecules get too close. The most common expression is

$$V_{LJ} = 4\epsilon[(\frac{\sigma}{r})^{12} - (\frac{\sigma}{r})^6] \quad (24)$$

where ϵ is the depth of the potential well at the equilibrium distance, σ is the distance at which the potential is zero, and r represents the distance between particles. The $-r^{-6}$ term describes the attractive interaction, the energy of which is proportional to $-r^{-6}$. The repulsive term r^{-12} is chosen for convenience and simplicity of computation as the square of the attractive term. The properties of the neutral atoms or molecules are not so sensitive to the repulsive energy, as long as it is a steep function. The parameters can be obtained by fitting to experimental data or DFT calculations. The force

is defined by $\mathrm{F}(\mathbf{r}) = -\frac{\partial \mathrm{U}}{\partial \mathbf{r}}$, so the force derived from Lennard-Jones potential is

$$F(r) = 4\epsilon[12(\frac{\sigma^{12}}{r^{13}}) - 6(\frac{\sigma^{6}}{r^{7}})] \tag{25}$$

Lennard-Jones potential has a wide applications in computational simulations due to its simplicity, including description of molecules in the fluids. In Chapter 3, we will test the parametrized Lennard-Jones potential available in GULP for bulk Au, although its accuracy is limited to describe the metallic system.

2.2.2 Manybody Potentials

The potential functions describing the intermolecular energy are formulated as a summation over the interaction energy of particles (atoms) in the system. In the case of the pairwise potentials, the potential energy is the summation of two-body interaction energy of atoms with indices i and j. The pairwise potential energy of the system consisting N particles is described as:

$$U(\mathbf{r}) = \sum_{i=1}^{N} \sum_{j<i}^{N} U(r_{ij}) \tag{26}$$

where r_{ij} is the distance between atoms with indices i and j:

$$r_{ij} = |\mathbf{r}_i - \mathbf{r}_j| = \sqrt{(r_{j_x} - r_{i_x})^2 + (r_{j_y} - r_{i_y})^2 + (r_{j_z} - r_{i_z})^2} \tag{27}$$

The force acting on ith particle is

$$\mathbf{F}_i = -\frac{\partial}{\partial \mathbf{r}_i} u(\mathbf{r}) = -\frac{\partial}{\partial \mathbf{r}_i} \sum_{i=1}^{N} \sum_{j<i}^{N} U(r_{ij}). \tag{28}$$

Common pairwise potentials include Coulomb potential and Lennard-Jones potentials as described in the previous section.

In the case of the many-body potentials, the potential energy is the summation of the interaction energy of the i-th atom with all other particles in the system. The many-body potential energy of the system consisting N particles is calculated as:

$$U(\mathbf{r}) = \sum_{i=1}^{N} U(\mathbf{r}_i) \tag{29}$$

where $\mathbf{r}_i$ is the position of all atoms in the system. The force acting on ith atom is

$$\mathbf{F}_i = -\frac{\partial}{\partial \mathbf{r}_i} U(\mathbf{r}) = -\frac{\partial}{\partial \mathbf{r}_i} \sum_{j \neq i}^{N} U_j(\mathbf{r}_j). \tag{30}$$

2.2.3 Embedded Atom Method (EAM)

Embedded atom method (EAM) is a many-body potential describing the energy between atoms.[30] The general form of the potential energy of atom i is given by

$$E_i = F_\alpha(\sum_{i \neq j} \rho_\beta(r_{ij})) + \frac{1}{2} \sum_{i \neq j} \phi_{\alpha\beta}(r_{ij}) \tag{31}$$

where ρ_β is the electron density at ith atom due to all the other atom j of type β, r_{ij} is the distance between ith and jth atoms, F_α is the embedding energy to place atom i of type α in an electron density ρ_β, and ϕ is the pair-wise potential between ith and jth atoms. The idea of applying the electron charge density in the interatomic potential was adopted from first-principles, which was particularly appropriate for metallic systems with delocalized electrons. Therefore, various forms of EAM potentials have been developed and the method is widely applied in molecular dynamics simulations.

In this section, we will focus on several many-body EAM or EAM-analogous potentials for Au available in General Utility Lattice Program (GULP) [31] simulation package. Several potentials discussed here were developed based the idea of EAM, while others adopted the ideas of Finnis-Sinclair (FS) model or the second moment approximation to the tight binding model (TB-SMA). These models were proofed to be analogous in the expressions and the results, although the terms have different physical meanings.[32] The functional expressions of the Finnis-Sinclair and TB-SMA models are out of the focus of this work, and thus will not be discussed in detail.

Glue Potential

Ercolessi and Adams [33] developed a force-matching method based on fitting the potential to the first-principles atomic forces of various atomic configurations at finite temperature. The Glue potential is

$$V = \frac{1}{2}\sum_{ij}\phi(r_{ij}) + \sum_{i}U(\sum_{j}\rho(r_{ij})) \tag{32}$$

where $\phi(r)$ is a pair potential, $\rho(r)$ represents the atomic density, and $U(n)$ is a glue function. The glue function acts in the transformations (a) $\rho(r) \to A\rho(r), U(n) \to U(n/A)$, and (b) $\phi(r) \to \phi(r) + 2B\rho(r), U(n) \to U(n) - Bn$. Initially (a) and (b) were calculated with arbitrary inputs with constraints, and then the parameters are evaluated and recalculated after transformations until A and B were converged.

In the model, the variable functions were defined as cubic splines (third-order polynomials), which was a rough approximation. The results on applying such potential to Au particles will be discussed in Chapter 3.

Sheng Potential

Potential energy surface (PES) describes the energy of a system as a function of atomic positions, and can be used to study the thermodynamics and kinetics of the system.[34] A recent developing method for interatomic potentials is to parameterize the potential based on fitting the PES of small systems derived by first-principles calculations.[35, 31] The recently developed EAM potential by Sheng *et al* [15] used the force-matching method to optimize the semiempirical potential to match the slopes of the PES generated by first-principles simulations. The embedded atom method was used to fit the PES as

$$E_{tot} = \sum_{i,j}\phi(r_{ij}) + \sum_{i}F(n_i) \tag{33}$$

where $n_i = \sum_j \rho(r_{ij})$, $\phi(r_{ij})$, $F(n_i)$, and $\rho(r_{ij})$ are the pair, embedded, and density functions, respectively. These three functions were expressed as high-order quintic spline functions (fifth order polynomials).[36] The EAM potential was obtained from the recursive fitting process until several transformation parameters converge. These parameters were determined as a function of lattice constants and cohesive energy at room temperature, and the liquid density at the melting temperature, which were obtained from experiments. The forces on atoms, total energies and stress tensors of several hundreds

of configurations obtained from DFT calculations were included in the fitting database. The PES was generated using linear scaling to eliminate the discrepancies between DFT results and experimental data. This highly optimized EAM potential will be applied to the study of Au particles.

Universal Force Field Potential

The Universal force field (UFF) [37] was developed for the full periodic table in 1992. The fundamental parameters were based on the element, its hybridization and the connectivity. The potential energy is described as

$$E = E_R + E_\theta + E_\phi + E_\omega + E_{vdw} + E_{el} \tag{34}$$

where E_R corresponds to the valence interactions from bond stretching, E_θ from bond angle bending, E_ϕ for dihedral angle torsion, E_ω as inversion terms, and E_{vdw} describes the nonbonded interaction contributed from van der Waals, E_{el} from electrostatic terms.

In the UFF method, bond stretch interaction E_R is described as a harmonic oscillator:

$$E_R = \frac{1}{2} k_{IJ}(r - r_{IJ})^2 \tag{35}$$

or as the more accurate Morse function:

$$E_R = D_{IJ}[e^{-\alpha(r-r_{IJ})} - 1]^2 \tag{36}$$

where k_{IJ} is the force constant in units of (kcal/mol)/Å^2, r_{IJ} is the bond length in Å, D_{IJ} is the bond dissociation energy (kcal/mol), and $\alpha = (k_{IJ}/2D_{IJ})^{1/2}$.

The force is

$$F = G(Z_I^* Z_J^* / r_{IJ}^2) \tag{37}$$

where Z_I^* and Z_J^* are effective charges, G is 332.06, and the force constant becomes $k_{IJ} = 2G(Z_I^* Z_J^* / r_{IJ}^3)$.

The angular distortions, can be described as a general form:

$$E_\gamma = K \sum_{n=0}^{m} C_n cos(n\gamma) \tag{38}$$

where K and C_n are coefficients, and γ corresponds to θ as in bond angle bending, ϕ as in dihedral angle torsion and ω as in inversion terms.

The van der Waals interaction in the UFF is described as

$$E_{vdw} = Ae^{-Bx} - C_6/x^6 \tag{39}$$

where B is the repulsive exponential parameter and C_6 is the dispersive attractive term, both of which is determined for the entire periodic table.

The final term, the electrostatic interactions, is described as:

$$E_{el} = 332.0637(Q_i Q_j / \epsilon R_{ij}) \tag{40}$$

The UFF was developed to predict structures of main group, transition metal, inorganic, and organometallic compounds. The accuracy of the structural prediction on bulk Au and Au particles will be discussed in Chapter 3.

Sutton-Chen Potential

Sutton-Chen potential was considered as long-range Finnis-Sinclair potentials,[38] and was first developed to model mechanical interactions between atomic clusters.[39] The total energy was written in the form:

$$E_T = \epsilon[\frac{1}{2}\sum_{ij} V(r_{ij}) - c\sum_i \rho_i^{1/2}] \tag{41}$$

where

$$V(r) = (a/r)^n \tag{42}$$

and

$$\rho_i = \sum_{i \neq j} (\frac{a}{r_{ij}})^m \tag{43}$$

Here r_{ij} is the distance between ith and jth atoms, ϵ is a parameter in the unit of energy, c is a positive dimensionless parameter, a is a parameter in the dimension of length, and m and n are positive integers where $m < n$. It is obvious that Finnis-Sinclair potential has the same form to those developed in EAM potential, although the physical interpretation is different. The FS equations are based on the tight-binding method, while the EAM is based on DFT.

The effective pair potential obtained was

$$V_{eff}(r) = \epsilon[(\frac{a^f}{r})^n - \frac{nS_n^f}{mS_m^f}(\frac{a^f}{r})^m] \tag{44}$$

Obviously the Sutton-Chen potential is a Lennard-Jones m-n potential, where S_n^f was defined as the lattice sum in the FCC crystal as $\sum_j [a^f/r_j]^n$. Similar term was defined for S_m^f. The origin of Sutton-Chen determined that

the range of this potential was the same as Lennard-Jones potential, with improvement by adopting the density term from Finnis-Sinclair formalism.

Johnson Potential

The fundamental equation of EAM was applied in developing this potential. The basic equations simplified by Johnson [40] are

$$E_{tot} = \sum_i F(\rho_i) + \frac{1}{2}\sum_{i,j} \phi(r_{ij}) \tag{45}$$

$$\rho_i = \sum_j f(r_{ij}) \tag{46}$$

where E_i is the total energy, ρ_i is the electron density at ith atom due to all the other atoms, r_{ij} is the distance between ith and jth atoms, $f(r_{ij}$ is the electron density at ith atom contributed from jth atom as a function of r_{ij}, $F(\rho_i)$ is the embedding energy to put atom i in an electron density ρ_i, and ϕ is the two-body potential between ith and jth atoms.

In Johnson potential, the electron density and the two-body potential were taken into consideration:

$$f(r) = f_e e^{-\beta(\frac{r}{r_e}-1)} \tag{47}$$

and

$$\phi(r) = \phi_e e^{-\gamma(\frac{r}{r_e}-1)} \tag{48}$$

The embedding function was fitted to a universal equation of state, derived as

$$F(\rho) = -E_c(1 - lnx)x - 6\phi_e y \tag{49}$$

where $x = (\rho/\rho_e)^{\alpha/\beta}$, $y = (\rho/\rho_e)^{\gamma/\beta}$ and $\alpha = 3(\Omega B/E_c)^{1/2}$. The parameters in the model, equilibrium lattice constant a, atomic volume Ω, the bulk modulus B, the cohesive energy E_c, were evaluated from quantum calculations for FCC metals. Unrelaxed vacancy-formation energy and Voigt-average shear modulus were used as physical input as well.

Cleri-Rosato Potential

Cleri-Rosato potential was developed for transition metal alloys using the second-moment approximation of the tight-binding scheme [41] based on the original tight-binding (TB) method.[42, 43] The total cohesive energy of the system is

$$E_c = \sum_i (E_R^i + E_B^i) \tag{50}$$

where the ion-ion repulsive term is

$$E_R^i = \sum_j A_{\alpha\beta} e^{-p_{\alpha\beta}(r_{ij}/r_0^{\alpha\beta}-1)} \tag{51}$$

and the band energy is

$$E_B^i = -\{\sum_j \xi_{\alpha\beta}^2 e^{-2q_{\alpha\beta}(r_{ij}/r_0^{\alpha\beta}-1)}\}^{1/2} \tag{52}$$

where r_{ij} is the distance between atoms i and j, $r_0^{\alpha\beta}$ is the first-neighboring distance in the $\alpha\beta$ lattice, A, p, q and ξ are parameters depending on the interacting atomic species α and β. The Eqn. 52 is considered equivalent to the embedding energy term in the EAM potential. The parameters were fitted to the experimental cohesive energy, lattice parameters and independent elastic constants. Cleri-Rosato potential applied the TB-SMA model to longer range, resulting in a quite good agreement with experimental results.

2.2.4 Conclusion

In this section, we have briefly explained the classical force field simulations, and the functions of the force field potentials are described. First, pair-wise potentials are introduced to describe the basic concepts in force field. Next, the many-body potentials are introduced, with emphasis on the embedded atom method potentials. The EAM potentials are then described in terms of the formulations of energy and force. In this way, the basic concepts of the potentials to be utilized in Chapter 3 are provided.

3 Atomistic Simulations of Au Nanoparticles

3.1 Introduction

Relating the properties of a material to its atomic structure through characterization is the basis of materials science. The structure problem can be simply stated as the problem of finding the atomic arrangement given a new material. In the case of bulk crystals, there are reliable solutions to the problem. For example, X-ray diffraction (XRD) provides a robust tool to identify the atomic structure of a crystal by measuring the angles and intensities of the diffraction beams. Computational simulations, including both classical and quantum mechanical approaches, are capable of predicting bulk structures with high accuracy. In the case of nanomaterials, however, the structure problem becomes complex. Characterizing their structure is crucial and remains a great challenge, due to the facts that their structures are inherently complex, and the structures at nanoscale cannot be exactly solved using the experimental techniques. Powder X-ray diffraction techniques are frequently used for characterizing nanostructures. However, the structural parameters obtained through diffraction techniques can yield multiple structural solutions with equal validity, due to the diffraction averaging of different structural parameters in the nanoparticle ensemble. To tackle this problem, we combine computational simulations of NP structures and theoretical modeling of X-ray diffraction pattern in collaboration with Prof. I. C. Noyan at Columbia University and Dr. H. Yan at NSLS-II Hard X-ray Nanoprobe beam line at Brookhaven National Laboratory. First, classical molecular dynamics (MD) simulations were carried out to elucidate the trends of the structural, energetic and thermal properties of NPs as a function of NP size, shape and temperature. Next, the MD-generated structural models were fed as input structures to the highly parallel forward diffraction code scaling up to thousands of GPU nodes. Finally, the synthetic diffraction datasets were analyzed to extract the average structural parameters. By comparing these parameters with the input structures, we aim to benchmark and improve the accuracy, precision and resolution of X-ray diffraction analysis, and extend the applicability of X-ray powder diffraction and nanodiffraction into a wider range.

In this chapter, the performance of MD simulations using classical force field potentials was evaluated based on experimental data for bulk and first-principles calculations for small clusters. This is to ensure the robustness of

the potential for generating reliable atomistic structures. Then the structures were analysed and characterized both qualitatively and quantitatively by examining the coordination numbers, mean interatomic distance, and radial distribution functions. The lower limit in particle size that classical MD simulations can be trustworthy was probed based on the structural analysis of structure models.

3.2 Benchmarks

As discussed in the previous chapter, the classical force field potentials have a wide variety of functional forms, which are parametrized to serve specific purposes. In this chapter, our main goal is to generate and characterize realistic models and therefore we will mainly focus on the structural properties, such as interatomic distances, bond length distribution, coordination numbers, and atomic displacement contributed from surface effect, finite size effect and/or thermal effect. The selection of a robust FF potential to well reproduce the structural features of unsupported metal nanoparticles is a non-trivial task. As developing a new semiempirical potential is out of our current scope, we compare the performance of several popular choices of force field potentials for Au and apply the most trusted potential in our simulations throughout subsequent studies presented in this chapter.

3.2.1 Bulk Au

Structure relaxations for benchmarking were carried out using General Utility lattice Program (GULP) [31]. Conjugate gradients were applied to optimize the geometry. The cohesive energy, lattice constant and elastic properties of bulk Au estimated from simulations at 0 K using these FF potentials are listed in Table 1. In general, different reference data used in the development of potentials, for example, experimental cohesive energies, resulted in discrepancy among the simulation results. The Sheng potential, UFF potential and L-J potential have used the same reference for cohesive energy (3.93 eV/atom), which is different from 3.78 eV/atom or 4.07 eV/atom used for the other potentials implemented in GULP. Moreover, the structural optimization was carried out at 0 K, resulting in further systematic discrepancy in lattice constant and elastic constants, of which references were obtained at 300 K. Nonetheless, the discrepancy of lattice constant predicted by each potential was within 0.5%, and the estimated elastic properties were within

Table 1: Properties of bulk Au predicted by FF potentials at 0 K. Reference for cohesive energy (E_{coh}) is obtained at 0 K in the unit of eV/atom, those of the other properties at 300 K. a_0 represents lattice constant in Å, c_{11}, c_{12} and c_{44} are elastic moduli in GPa. K is bulk modulus in GPa, G shear modulus in GPa, E Young's modulus in GPa, and ν Poisson's ratio (unitless).

	Reference	Potential						
		Sheng	UFF	S-C	Johnson	C-R	Glue	L-J
E_{coh}	3.93	3.93	3.93	3.78	4.07	3.78	3.78	3.93
a_0	4.08	4.06	4.08	4.08	4.07	4.08	4.07	4.08
c_{11}	193	214	183	180	195	187	220	416
c_{12}	163	177	159	148	170	154	160	238
c_{44}	42	51	45	42	42	45	60	238
K	180.3	189.5	166.9	158.5	178.1	165.4	180.4	297.2
G	27	29.7	21.6	25.5	21.6	26.5	42.8	142.4
E	78	53.1	35.7	46.6	36.8	47.9	85.2	242.6
ν	0.44	0.45	0.46	0.45	0.47	0.45	0.42	0.36

a reasonable range, except for L-J potential as expected. We are to continue the selection process using all the potentials except L-J potential.

3.2.2 Au Nanoparticles

It is well-known that DFT calculations can provide robust references in structural analysis at small NPs and a relatively good reference for energetics, which serves the primary goal of this work to characterize realistic structural models. Due to significantly increasing cost at larger particle sizes, DFT-PBE optimizations were carried out on Au_{55}, Au_{249} and bulk Au as reference. The cohesive energy of bulk Au estimated from spin-polarized DFT calculation is 3.07 eV/atom, which is 23 % smaller than the experimental value. The lattice constant calculated from DFT was overestimated by 2 %.

A series of Au NPs from 1.2 nm to 4 nm in diameter were spherically cut from bulk FCC Au, and optimized at energy minimum at 0K using the selected potentials, as shown in Fig. 1. As shown in Fig. 2, the cohesive energies (E_{coh}) as a function of inverse radius (r^{-1}) were fitted to $E_0 + Ar^{-1}$, with fitted E_0 being the cohesive energy at bulk, and fitted slope A being -3.16, -3.97, -3.13, -2.11, -2.86, -1.96, -6.67 in the unit of eV/Å, for DFT-

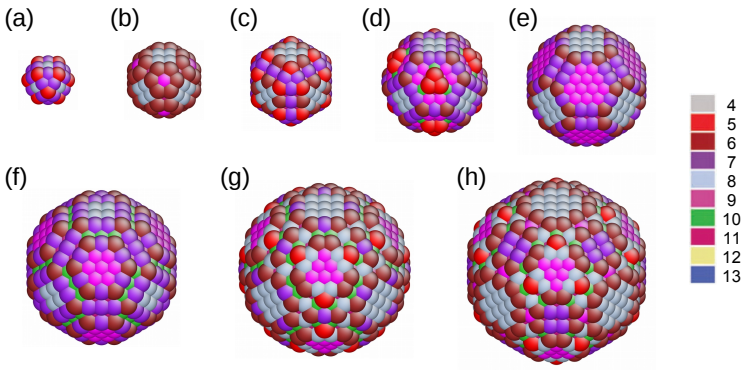

Figure 1: Views of optimized structures of Au NPs. Sizes (radius, r) of the NPs through (a) to (g) are Au_{55} (6 Å), Au_{135} (8 Å), Au_{249} (10 Å), Au_{429} (12 Å), Au_{675} (14 Å), Au_{959} (16 Å), Au_{1433} (18 Å), and Au_{1985} (20 Å). Atoms were colored according to the coordination numbers.

PBE, Sheng, UFF, Sutton-Chen, Johnson, Cleri-Rosato, and Glue potential, respectively. The trend of cohesive energy predicted by DFT is similar to that of UFF with an almost constant shift down of 0.9 eV/atom. Among the FF potentials, the predicted slope by Glue potential has the largest discrepancy from that by DFT. Lack of DFT data points at intermediate sizes may introduce minor errors, which however should not effect the overall trend in energetics significantly.

Structural analysis by radial distribution functions (RDFs) assisted further comparisons among different potentials. As reference, the RDF peaks of PBE-optimized Au_{55} and Au_{249} were reduced by 2 %, to compensate for the fact that PBE overestimates the bond length by 2 % in bulk Au. The first RDF peaks, which shows the distribution of the first nearest neighbor distances, i.e., bond length, are plotted for Au_{55} and Au_{249} in Fig. 3 and Fig. 4, respectively. The first RDF peaks are discrete in the plots due to small number of atoms and small bin width (0.002 Å). Discrepancies between PBE and each potential in the lower bound, the upper bound, and the highest intensity peak position were computed and added up as an index for judgement. In summary, the performance of the Sheng potential scores the highest, with an accumulative error of 2.3 % for Au_{55} and 2.8 % for Au_{249}. RDF peaks of the Sutton-Chen and Cleri-Rosato potentials show similar bond length distributions, with accumulative errors in the range of 3.2 % to 4.1 %. The RDF peaks of the UFF and Johnson potentials show similar behaviours as

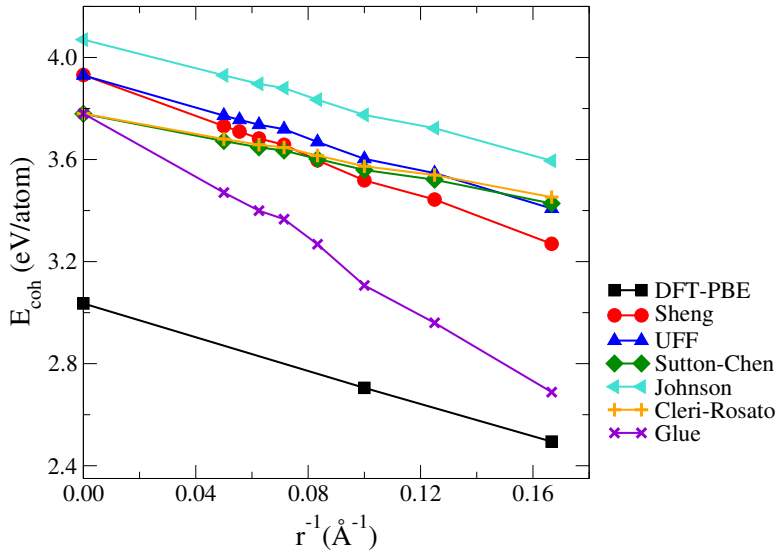

Figure 2: The computed cohesive energies (E_{coh}) as a function of inverse radius (r^{-1}) using DFT-PBE (black squares), Sheng (red circles), UFF (blue up triangles), Sutton-Chen (green diamonds), Johnson (cyan triangles left), Cleri-Rosato (orange pluses), and Glue (violet crosses).

well and have larger discrepancy from DFT results. The glue potential predicts a wide spread of bond length, which fails to reproduce the bond length distribution from PBE.

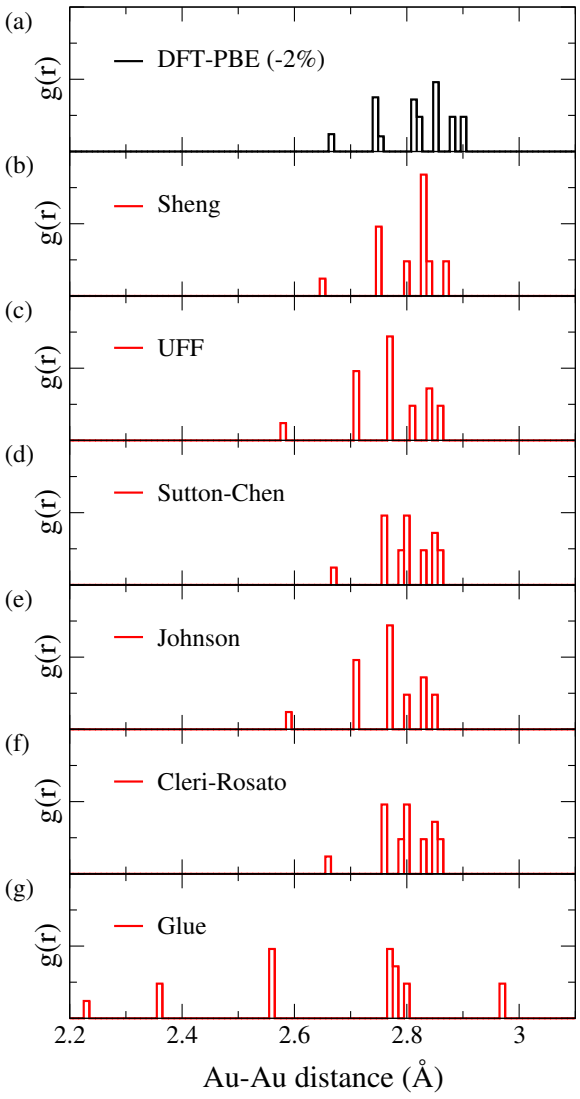

Figure 3: Radial distribution functions of Au_{55}. Structures optimized using DFT-PBE (a), Sheng (b), UFF (c), Sutton-Chen (d), Johnson (e), Cleri-Rosato (f), and Glue (g). Peaks of DFT-PBE were reduced by 2 % for comparison.

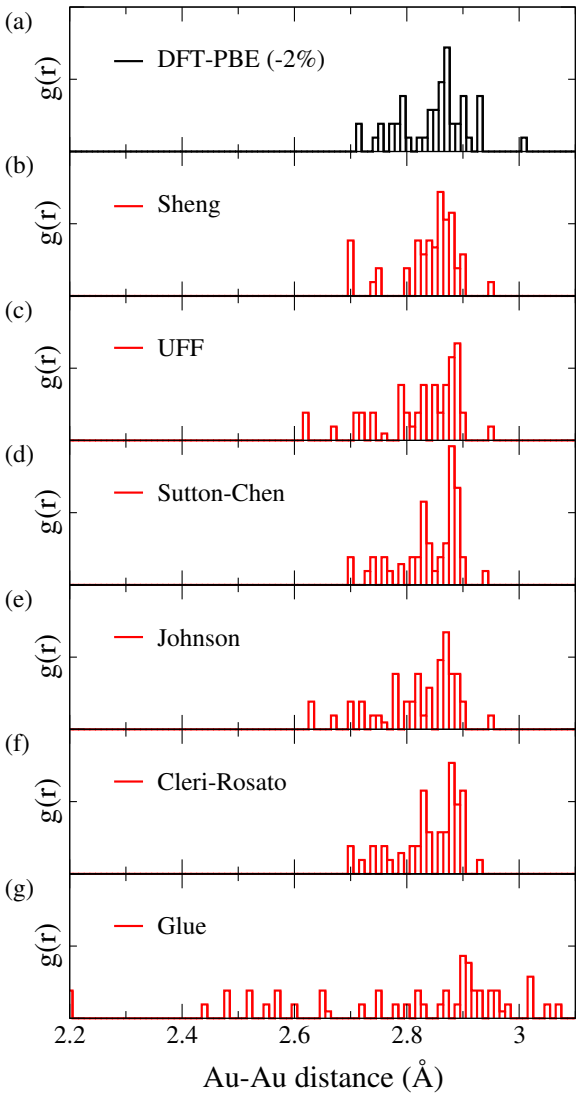

Figure 4: Radial distribution functions of Au_{249}. Structures optimized using DFT-PBE (a), Sheng (b), UFF (c), Sutton-Chen (d), Johnson (e), Cleri-Rosato (f), and Glue (g). Peaks of DFT-PBE were reduced by 2 % for comparison.

3.2.3 Surface Effect

The first peaks in radial distribution functions were generated and compared for optimized Au NPs at 0 K from 1.2 nm to 4.0 nm in diameter using the Sheng potential, as shown in Fig. 5. The peak position, which indicates the most abundant bond length in the particle, increases as particle size increases, and approaches the bond length at 2.884 Å in bulk Au. The sharpness of the peak increases as size increases, resulting in quickly decreased full width at half maximum. These deviations from bulk Au are mainly contributed from the surface atoms. While the coordination number is 12 for atoms in bulk FCC crystal, all the surface atoms of the investigated spherical NPs at 0 K are undercoordinated, as shown in Fig. 1, resulting in increasing surface strain and thus overall decreasing bond length. As particle sizes increases from 1.2 nm to 4.0 nm, the percentage of the surface atoms decreases from 76.4 % to 35.7 %. As a result, the bulk-like core atoms become dominant in larger particles and the overall contraction of bonds contributed from the undercoordinated surface atoms becomes limited as shown in the peaks. It is noticed that the range of first distance peaks increases in larger particles, indicating a general trend of wider distribution in bond length. This is contributed from the wider variety of the surface morphology as size increases, from a combination of (100) and (111) facets in Au_{55} to more complex combination of higher order facets in larger particles. The coordination numbers of surface atoms in Au_{55} varies from 5 to 8, and that in Au_{1985} varied from 5 to 11.

To further study the surface effect, a series of hollow particles were generated by cutting the core atoms out of a Au particle of 3.2 nm in diameter. The structures were relaxed at 0 K using Sheng potential in GULP, as shown in Fig. 6. The thickness of the shell in these hollow particles were 4 Å, 6 Å, 8 Å to 10 Å in Fig. 6 a to d, respectively. The solid particle was included in Fig. 6 (e) as reference. The bond length distribution along the radius in Fig. 6 clearly showed that the bond length at both inner and outer surfaces had the tendency to be smaller than the bulk value, in accordance with the smaller coordination numbers at both surfaces. We defined the $\pm$ 2 % of the bond length in bulk Au as cut-off distances, so that the region where the bond length frequently fell outside the bounds was defined as the penetration zone. As shown in Fig. 6, the penetration zone at the outer surface was about 2 Å, which includes the first to the second atomic layer normal to the surface, and the bond length in the penetration zone showes large diversity

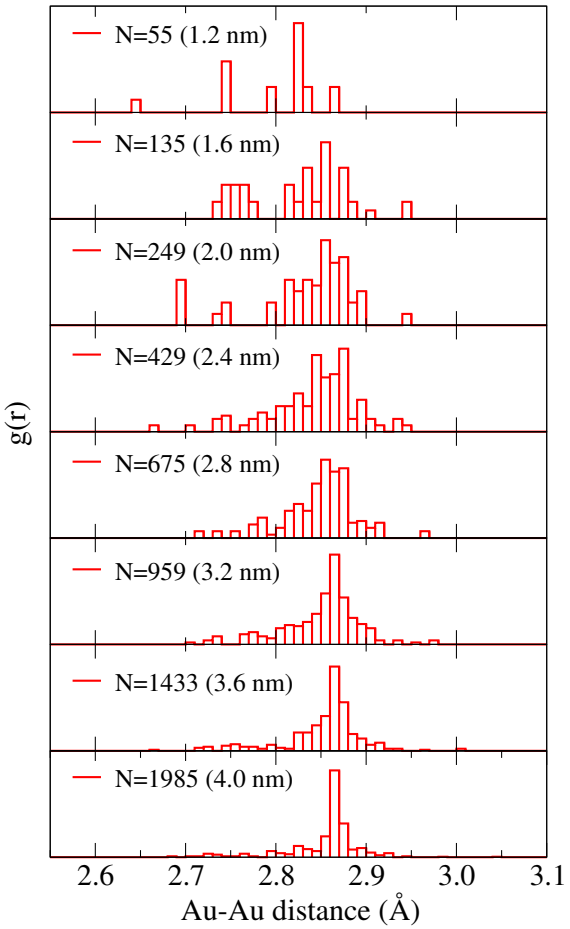

Figure 5: Radial distribution functions generated from Sheng potential for Au_{55} (1.2 nm), Au_{135} (1.6 nm), Au_{249} (2.0 nm), Au_{429} (2.4 nm), Au_{675} (2.8 nm), Au_{959} (3.2 nm), Au_{1433} (3.6 nm), and Au_{1985} (4.0 nm).

from the bulk value. Bond contraction at the inner surface is less severe than that at the outer. The difference in bond distribution at the outer surface and at the inner surface can be explained by smaller coordination numbers in average at the positively curved outer surface than at the negatively curved inner surface, resulting in larger bond contraction in the former.

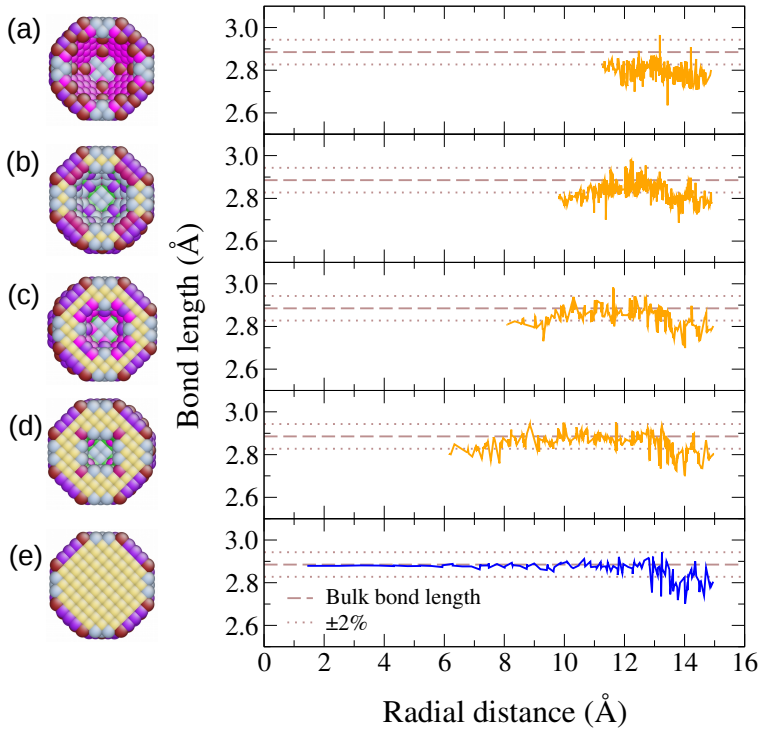

Figure 6: Cross-section views of hollow Au particles (left) and bond length distributions along radial distance (right) for Au_{578} with 12 Å $\leq r \leq$ 16 Å (a), Au_{734} with 10 Å $\leq r \leq$ 16 Å (b), Au_{824} with 8 Å $\leq r \leq$ 16 Å (c), Au_{904} with 6 Å $\leq r \leq$ 16 Å (d), and Au_{959} with $r \leq$ 16 Å (e). Atoms were colored according to the coordination number. Bond length in bulk Au was labeled in dashed line, with $\pm$ 2 % as the upper and lower bounds in dotted lines.

3.3 Au NPs at Finite Temperatures

Catalytic reactions operate at elevated temperatures and often undergo the annealing process. Therefore, it is of great interest to study the structural evolution of the nanoparticles at finite temperature. In this section, classical MD simulations were performed to investigate how the structures of NPs with different sizes (3 nm to 10 nm) and shapes (sphere and cube) evolve with temperatures.

3.3.1 Computational Methods

Classical molecular dynamics simulations [44] were carried out using LAMMPS [45] with a highly optimized embedded atom method potential developed by Sheng, *et al* [15]. Energy minimization at 0 K was performed until the total energy and the forces were converged to 10^{-12} eV and 10^{-12} meV/Å, respectively. MD simulations at selected finite temperature were performed at constant temperatures for the canonical (NVT) ensemble for 5 ns. Thermodynamic data (e.g. temperature, energy, pressure) were computed every 10^{-3} ps and recorded every 10^{-1} ps. A total of 1000 configurations was collected every 1 ps in the last 1 ns for structural analysis. Coordination number was calculated with a cutoff distance of 3.3 Å for all geometry.

To study the size dependence of energetics and structural features, Au NPs in the size of 3 nm (N = 736), 5 nm (N = 3589) and 10 nm (N = 28897) in diameter were investigated, as shown in Fig. 7. The spherical shape were adopted by truncating spheres out of the bulk Au FCC crystal. To probe the shape effect, cubic Au NPs with side length of 3 nm (N = 1688), 5 nm (NN = 7813) and 10 nm (N = 66326) were generated by truncating along the (100), (010) and (001) planes of bulk Au. The spherical and cubic structures adopted here do not correspond to the most stable structures found in the experiments.

Fig. 8 shows a typical plot of the total energy per atom (E) at finite temperatures as a function of time for the spherical 3 nm Au NP. By definition, E is the negative value of E_{coh} in classical FF simulation. Large energy fluctuation occurred at the initial stage, normally within 0.2 ns before converging to a moderate oscillation around the average value. Significantly larger energy fluctuation was observed at the crystalline to amorphous transition temperature , in this case around 880 K. Nevertheless, structural parameters were extracted from 1000 configurations at transition temperature as well, even

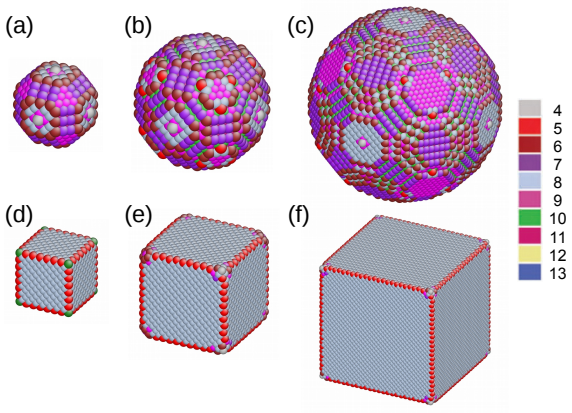

Figure 7: Optimized structures of spherical 3 nm (a), 5 nm (b) and 10 nm (c) Au NPs, and cubic 3 nm (d), 5 nm (e) and 10 nm (f) Au NPs. Atoms were colored according to coordination numbers.

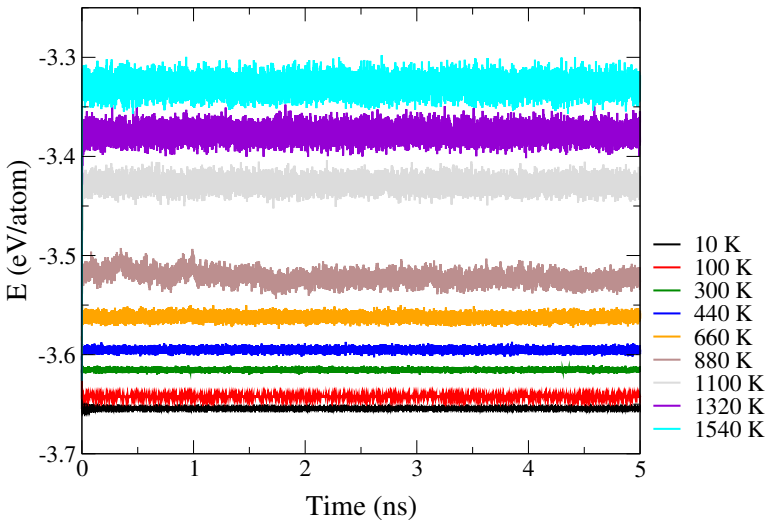

Figure 8: Energy of spherical 3 nm Au NPs at various temperatures. Each simulation was maintained at a constant temperature for 5 ns.

though such system may not have reached its equilibrium at the investigated time frame.

Temperatures during heating in experiments undergo an elevated process, and thus simulations often include heating at a constant rate or step-heating at the initial stage to mimic the realistic heating process. However, tem-

perature in this work was set at constant during the entire MD simulation and the relatively large time duration (5 ns) used in MD simulations allows the single particle system reaching equilibrium well before data collection (except at transition temperatures), as shown in Fig. 8. Indeed, results from simulations for the spherical 3 nm Au NP at different heating rates showed that the averaged energy of 1000 configurations and the standard deviation were within 0.05 % and 7 %, respectively. Therefore, we are confident that NP structures obtained using the simplified constant-temperature procedure are representative at given temperatures and can be reliable for subsequent structural analysis.

3.3.2 Spherical Au NPs

In this section, we will focus on characterization of spherical Au NPs using a combination of different structural properties. The overall size and temperature effect contributed from all atoms in 1000 configurations will be investigated.

Spherical single-crystalline Au NPs with diameter of 3 nm, 5 nm and 10 nm were equilibrated at finite temperatures up to above the melting temperature of bulk gold of 1337 K. Fig. 9 shows the equilibrium structures of 5 nm NPs at each temperature. The temperatures goes from 10 K to beyond the bulk melting points and therefore produces both crystalline and amorphous NP structures. The melting points of spherical 3 nm, 5 nm and 10 nm NPs can be roughly estimated from Fig. 10 as 900 K, 1100 K and 1250 K, respectively. For the 5 nm particle, the near perfect spherical shape was maintained at temperatures up to 660 K. At 880 K, the surface of the particle became (100) and (111) facet dominated. The surface of an ideal spherical particle contains multiple high-index planes as shown in Fig. 9, resulting in high surface energy. Increasing annealing temperature provided energy high enough to conquer the energy barrier for bond-breaking and reforming, so that the surface underwent evolution from high-index planes to low-index facets to minimize its surface energy. The (111) and (100) facets have the lowest surface energy for Au FCC crystal, and therefore are the dominant facets after annealing. Similar evolution of surface structure has been observed in experiments at 373 K and 473 K for Au particle about 5 nm in diameter.[13] At temperatures above its melting point at 1100 K, the shape of 5 nm particle became amorphous. The overall shape is near spherical with irregular surfaces. Similar structure transition were observed for 3 nm and

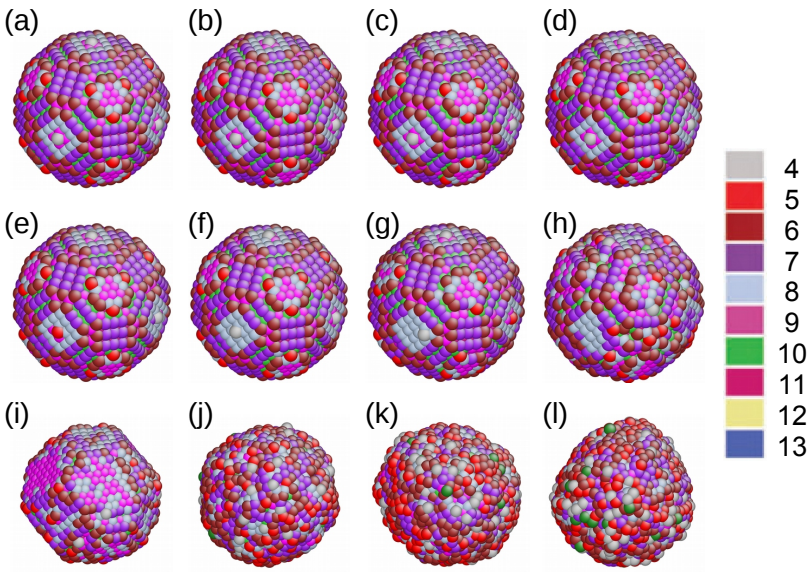

Figure 9: Views of spherical 5 nm Au NPs at 5.00 ns at 10 K (a), 50 K (b), 100 K (c), 150 K (d), 200 K (e), 300 K (f), 440 K (g), 660 K (h), 880 K (i), 1100 K (j), 1320 K (k) and 1540 K (l). Atoms were colored according to coordination numbers.

10 nm particles at different temperatures due to different melting points.

Fig. 11 shows the averaged energy over 1000 configurations at finite temperatures for spherical 3 nm, 5 nm and 10 nm particles. Dramatic increase in energy is observed as temperature raises above experimental melting temperature. The energies (E) as a function of temperature for Au crystallines were fitted to $E_0 + a * T$, with fitted E_0 being -3.66, -3.77 and -3.86 eV/atom, and fitted slope a being 1.47×10^{-4}, 1.44×10^{-4} and 1.55×10^{-4} in the unit of eV/K for 3 nm, 5 nm and 10 nm particles, respectively. For the amorphous structures, the energies were also fitted to $E_0 + a * T$, with fitted E_0 being -3.67, -3.77 and -3.82 eV/atom, and fitted slope a being 2.25×10^{-4}, 2.20×10^{-4} and 2.15×10^{-4} in the unit of eV/K for 3 nm, 5 nm and 10 nm particles, respectively. The discrepancy in fitted E_0 for crystalline and amorphous particles is negligible for each size, indicating the energy at either phase will converge at 0 K. The slope in amorphous region at each size is significantly higher than that in crystalline, indicating a higher heat capacity in amorphous particle.

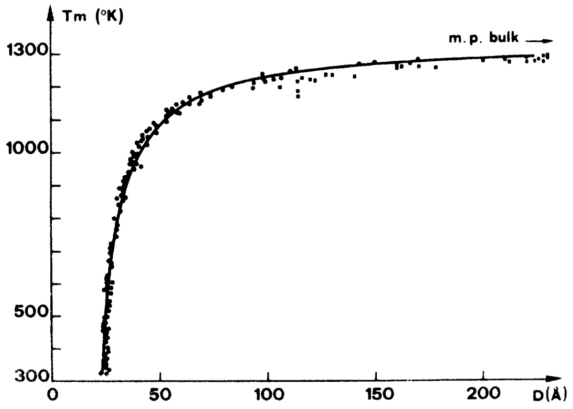

Figure 10: Experimental (circles) and theoretical (line) melting temperatures of Au particles as a function of size (Reproduced from Buffat [1]). The solid line represents a least-square fit to a model based on the starting assumption that solid-liquid particles having the same mass coexist at the melting point.

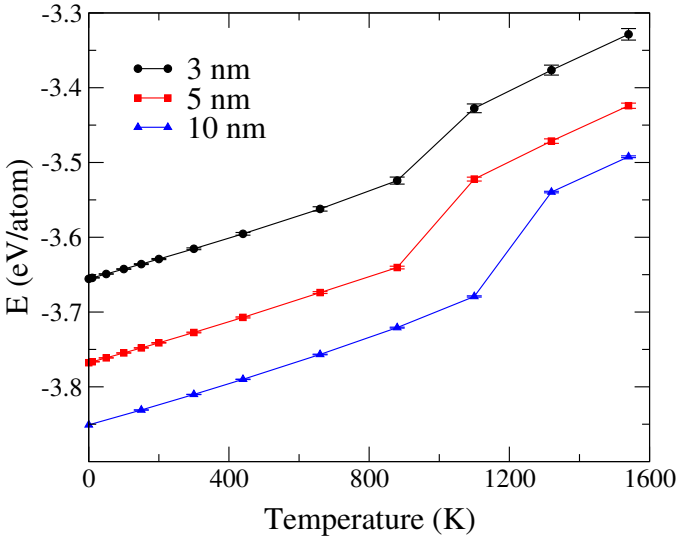

Figure 11: Energy of spherical 3 nm (black circles), 5 nm (red squares) and 10 nm (blue up triangles) Au NPs as a function of temperature. Standard deviation of each data point was included. Energies were fitted to $E = E_0 + a * T$ with different E_0 and a for crystalline region and for amorphous phase.

Coordination Numbers. Spherical Au crystalline possesses complex surface structures, including facets, edges, steps and corners of different coordination numbers, as shown in Fig. 9 for the spherical 5 nm Au NP. Similar surface structures were also found for 3 nm and 10 nm Au NPs. Coordinate-dependent bond length contraction at surface has been observed in experiments [46] and was confirmed in the previous subsections at 0 K. At temperatures up to 200 K, the coordination numbers almost remain constant, which are shown as overlapping circles in Fig. 12, Fig. 13 and Fig. 14 for 3 nm, 5 nm and 10 nm NPs, respectively. Core atoms with a coordination number of 12 dominates at low temperature, being 53.5 %, 70.7 % and 84.7 % of the total atoms for 3 nm, 5 nm and 10 nm NPs, respectively. Coordination numbers of surface atoms are under 12, depending on its morphology, where center atoms on (111) facet have coordination numbers of 9, edge atoms 8, corner atoms 5 to 6, and near center atoms on (100) facet have coordination numbers of 8, edge atoms 7, corner atoms 6. A total of 6 atoms in each particle are on top of (100) facets, with a coordination number of 4. Step atoms have coordination numbers of 10 or 11. The coordination numbers generally followed bimodal distributions where two distinct peaks occurred at 7 and 12 at low temperatures.

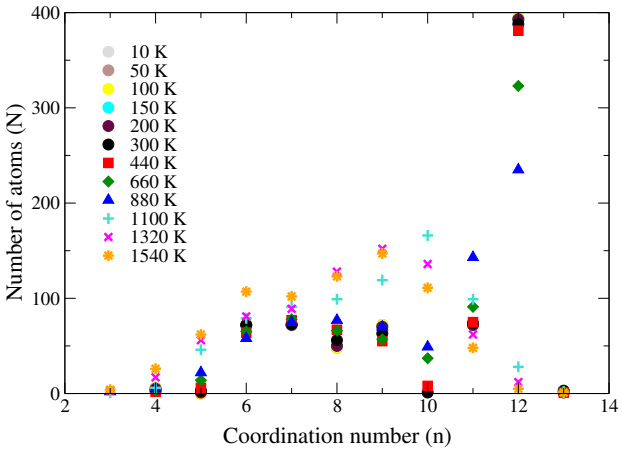

Figure 12: Coordination number of spherical 3 nm NPs at 10 K (grey circles), 50 K (brown circles), 100 K (yellow circles), 150 K (circle, cyan), 200 K (maroon circles), 300 K (black circles), 440 K (red squares), 660 K (green diamond), 880 K (blue up triangles), 1100 K (cyan pluses), 1320 (magenta crosses) and 1540 K (orange stars).

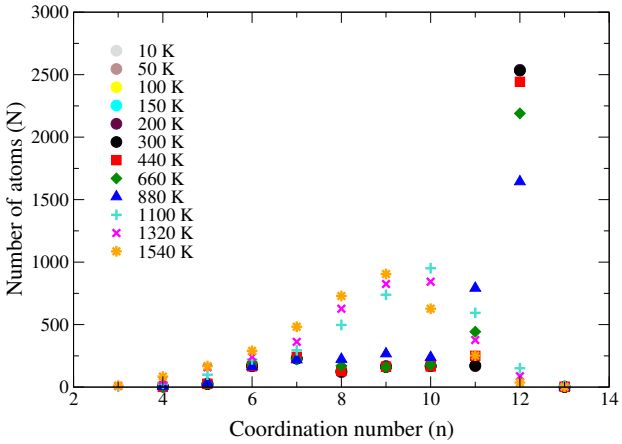

Figure 13: Coordination number of spherical 5 nm Au NPs at at 10 K (grey circles), 50 K (brown circles), 100 K (yellow circles), 150 K (circle, cyan), 200 K (maroon circles), 300 K (black circles), 440 K (red squares), 660 K (green diamond), 880 K (blue up triangles), 1100 K (cyan pluses), 1320 (magenta crosses) and 1540 K (orange stars).

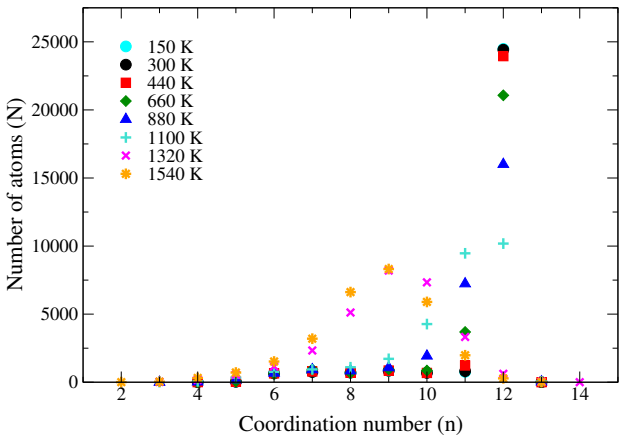

Figure 14: Coordination number of spherical 10 nm Au NPs at 150 K (circle, cyan), 300 K (black circles), 440 K (red squares), 660 K (green diamond), 880 K (blue up triangles), 1100 K (cyan pluses), 1320 (magenta crosses) and 1540 K (orange stars).

Starting from 300 K up to 880 K, population with 12 coordination numbers decreases as temperature increases, indicating a general trend of increase

in bond length beyond the cutoff of 3.3 Å. For example, the percentage of atoms with 12 neighbors at 880 K is 31.9 %, 45.8 % and 55.5 % for 3 nm, 5 nm and 10 nm NPs, respectively. In the meantime, population with smaller coordination numbers increases as temperature increases, and two distinct peaks start to merge at higher temperatures.

At temperatures above melting points, the distribution of the coordination numbers becomes unimodal. For both the 3 nm and 5nm particle, the coordination number distribution peaks at 10 for 1100 K, and 9 for 1320 K and 1540 K. For 10 nm particle with a melting point above 1200 K, coordination number below and above 1100 K shows a clear transition from bimodel to unimodel distribution, with significant reduction of population at 12 and increased population at low numbers.

Radial Bond Length Distribution. Bond length distribution along radial direction for spherical 5 nm particles shows the trend of particle expansion as temperature increases, as shown in Fig. 15. The cutoff distance for calculating bond length was set to be 3.5 Å, which is 20 % larger than bond length in bulk Au and yet smaller than the second nearest neighbor distance at 4.08 Å for bulk FCC Au. As temperature increases, the upper limit of atomic bonds along radius extends, indicating an increase of about 15 % in particle radius from 100 K to 1320 K. The first lowest and the second lowest limit of atomic bonds along radius are about 1.4 Å and 2.88 Å at temperatures up to 880 K, responding to half and full length of an atomic bond in FCC crystalline Au, respectively. Disappearance of these two characteristic bond lengths at 1100 K or higher indicated the disappearance of crystalline structures. Bond length distribution at 100 K is comparable to that observed in 3.2 nm particle at 0 K in Fig. 6, with similar penetration depth at about 2 Å and wider distribution of bond length at core. Not only contraction occurs at the surface, bond expansion occurs from about second layer beneath the surface and eventually extending to the whole particle. The spectrum of bond length becomes significantly wider at increased temperatures. The maximum bond length goes beyond the cutoff distance of 3.5 Å at higher temperatures, and the minimum bond length decreases below 2.4 Å.

Linear Thermal Expansion Coefficient. Although the bond length distribution provides a qualitative way to evaluate the thermal effect on particle size, a quantitative method to identify the characteristic length of the particle is in demand. In the bulk, the characteristic length is obviously the

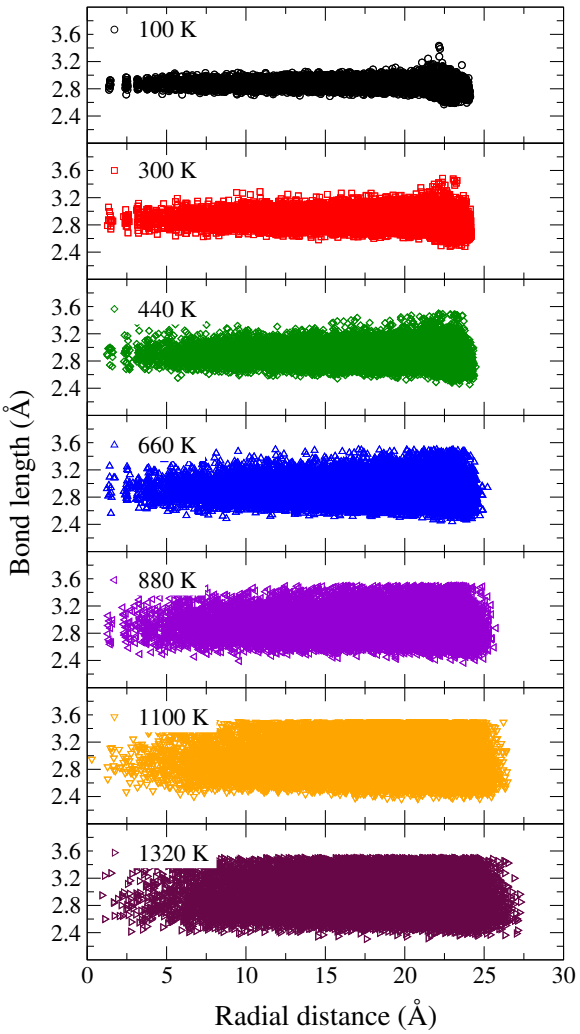

Figure 15: Bond length distribution along radial direction for spherical 5 nm Au NPs at 100 K (black circles), 300 K (square, red), 440 K (diamond, green), 660 K (up triangles, blue), 880 K (left triangles, violet), 1100 K (triangle down, orange), and 1320 K (triangle right, maroon). Bond length was calculated with a cutoff distance of 3.5 Å.

lattice constant, and the linear thermal expansion coefficient is defined as

$$\alpha_{\mathrm{L}} = \frac{1}{l}\frac{dl}{dT} \tag{53}$$

where l is the lattice constant in the bulk. However, there exists no such uniform lattice constant for finite systems due to atomic displacement from the perfect periodic lattice. A commonly applied length is the mean interatomic distance[47]

$$l_{miad} = \frac{1}{N(N-1)} \sum_{i,j=1}^{N} |\mathbf{r}_i - \mathbf{r}_j| \tag{54}$$

where $\mathbf{r}_i$ is the position of the ith atom of the N total atoms in the particle. The characteristic length, l_{miad}, measures the average pairwise atomic distance, and thus describes the average "extension" of the atomic structure. We calculated l_{miad} for 1000 configurations obtained at each finite temperature for each size, and the averaged l_{miad} with standard deviations as error bars were plotted as shown in Fig. 16. l_{miad} of the optimized structure at 0 K was also included. For near spherical particles at 3 nm, 5 nm and 10 nm in diameter, l_{miad} has the value of 14.68 Å, 24.94 Å and 50.06 Å at 0 K, respectively, approaching the radius of each particle. At $\mathrm{T} < \mathrm{T_{melt}}$ for all sizes, l_{miad} increases smoothly as a function of T. At $\mathrm{T} > \mathrm{T_{melt}}$ region, similar trend with larger slope is observed for all sizes. There are remarkable increases in l_{miad} as the temperature increases from below melting point to above, indicating significant structural deformations occurs when melting.

From Eqn. 53 where l_{miad} was applied as l, the linear thermal expansion coefficients were derived for all three sizes as shown in Fig. 17. The predicted linear thermal expansion coefficients of bulk Au using Sheng potential from MD simulations overlap with the experimental results at 160 K to 300 K, with increasing discrepancies up to 8.9 % as temperature increases. α_{L} for spherical particles are all positive at all investigated temperatures, indicating positive thermal expansion occurs at all three sizes. The positive trends for 5 nm and 10 nm particles are in general consistent with experimental observations for supported 5 nm particles [12]. However, the predicted trend for 3 nm particles fails to agree with experimental results for bare Au particles of 4 nm, where a crossover from a positive thermal expansion at lower temperatures to a negative thermal expansion at higher temperatures occurs at around 125 K [11]. The phenomena was proposed to contribute from the discrete electronic energy levels induced by the finite particle sizes.[48, 12] The vibrational and electronic energy of the system, are temperature-dependent, contributing to the positive thermal expansion and the negative thermal expansion as T increases, respectively. As particle size decreases, the contribution from the electronic energy due to thermally excited valence electrons

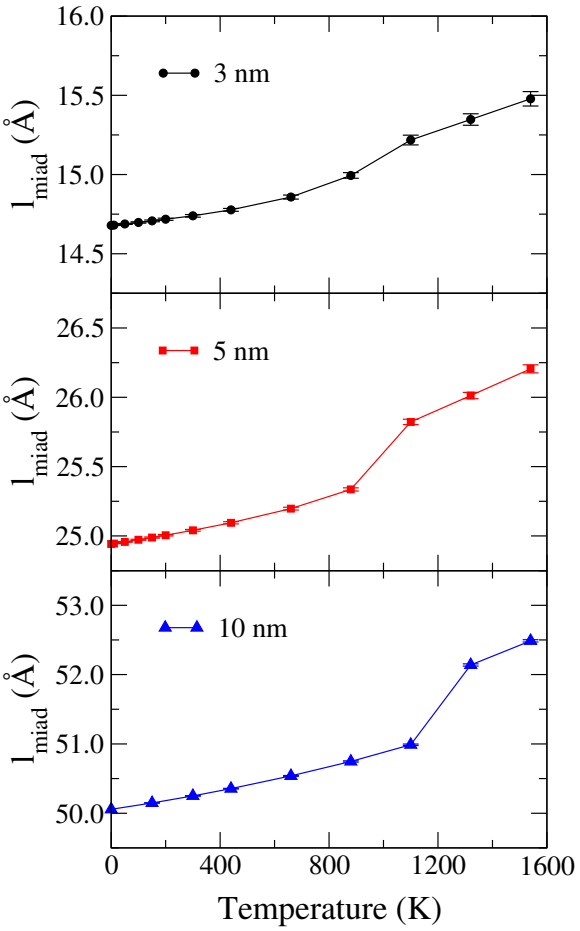

Figure 16: Averaged mean interatomic distances (l_{miad}) of spherical 3 nm (black circles), 5 nm (red squares) and 10 nm (blue up triangles) Au NPs as a function of temperature. l_{miad} was averaged over 1000 configurations at each temperature. Standard deviations were shown as error bars.

at increasing temperatures becomes significant, resulting in an overall negative thermal expansion. Unfortunately, classical EAM potential is limited to include only contribution from thermal vibrational energy, not the electronic energy. Therefore, the discrepancy of the predicted thermal behavior from the experimental results decreases as size increases. Nonetheless, the EAM potential successfully predicts the overall positive thermal expansions at larger sizes, approaching to bulk behavior as size increases. In addition,

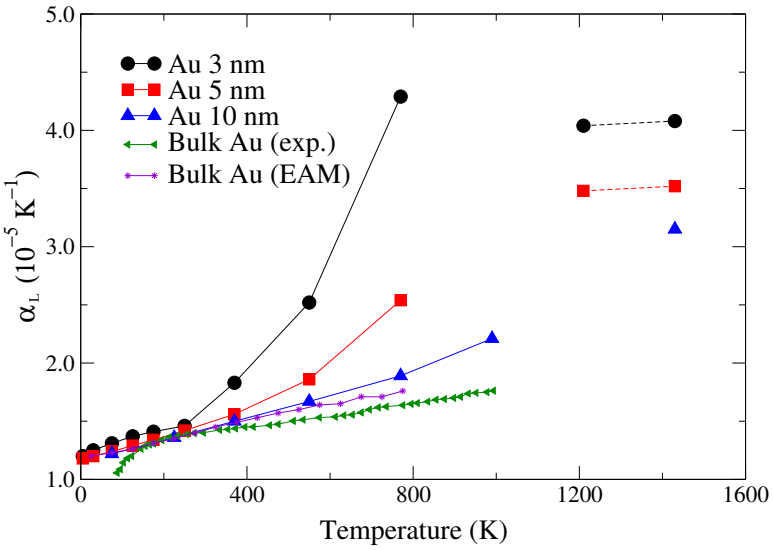

Figure 17: Linear thermal expansion coefficient (α_{L}) of spherical 3 nm (black circles), 5 nm (red squares) and 10 nm (blue up triangles) Au NPs as a function of temperature. Experimental reference for bulk Au (green left triangles) was reproduced from Nix and MacNair [2]. Coefficients of bulk Au calculated from Sheng potential were included (violet stars). α_{L} at melting temperature region for each particle was omitted. Data points at $\mathrm{T} < \mathrm{T}_{\mathrm{melt}}$ were connected with solid lines, those at $\mathrm{T} > \mathrm{T}_{\mathrm{melt}}$ with dashed lines.

the predicted α_{L} of amorphous particles are higher than those in crystalline-like particles, similar to the thermal behavior of liquid versus solid.

Raidal Distribution Function. Radial distribution function (RDF), $g(r)$, describes the atomic density as a function of distance from a reference particle, which provides detailed structural information about dynamical changes of the structures. Fig. 18 shows the first four RDF peaks averaged from 1000 configurations at each temperature. These four peaks correspond to the atomic densities at the nearest neighbour distances at [110] direction (bond length, d), [100] direction (lattice constant, $\sqrt{2}d$), [112] direction ($\sqrt{3}d$), and [110] direction ($2d$) in perfect FCC crystal, respectively. As temperature increases, the intensity of RDFs decreases and the peaks broaden due to thermal fluctuations. The coordination number reduces significantly as temperature increased, indicating decrease in the number of nearest neighbors within the cutoff distances (3.3 Å) and thus an increase

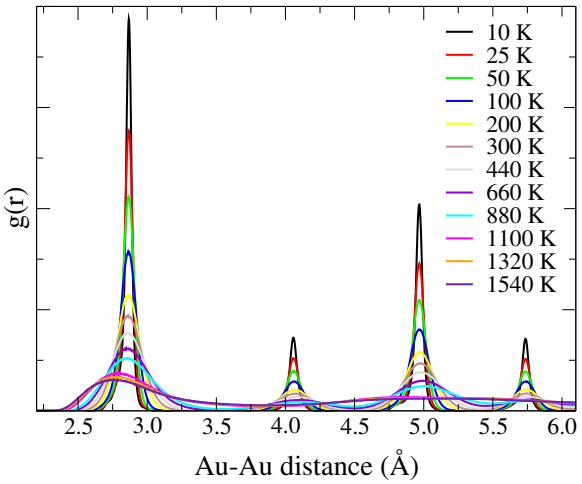

Figure 18: Averaged radial distribution functions of spherical 5 nm Au NPs at finite temperature. Peaks were averaged over 1000 configurations equilibrated at each temperature.

in nearest neighbor distances. The broad peak at smaller coordination numbers also indicates a broadening in bond length distribution. These facts correspond to the decreasing intensity of RDF peaks, and the broadening of the first peaks. A close investigation shows an increasing positive skewness of the first peaks at higher temperature, indicating more population of the bonds with larger bond lengths than the mode (maximum). The other peaks shows increasing asymmetries as well, partly due to the addictive effect from broadening neighboring peaks. The second and the fourth peak vanish at temperatures above melting point, indicating the absence of longer range order in the amorphous particles. Notable decrease in the positions of the first peak and the almost vanished third peak are observed at $T > T_{melt}$. Similar trends are found in 3 nm and 10 nm particles.

More detailed information was extracted from the RDF peak positions at the maximum points. The maximum, the breadth and the skewness of the RDF peaks should all be taken into consideration when evaluating the structures. Extracting the maximum seems straightforward. However, the breadth and the skewness are difficult to evaluate due to lack of fitting functions for RDFs. Due to the asymmetric nature of RDF peaks at elevated temperatures, fitting the peaks to Gaussian function resulted in increasing error at higher temperature. It is even more difficult to fit the peaks at larger

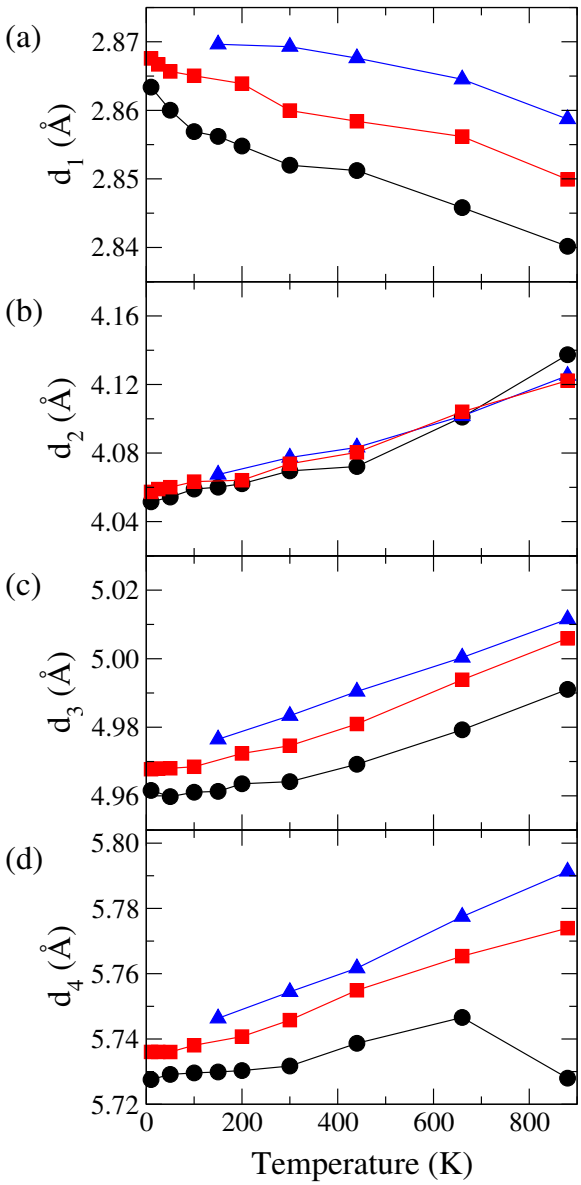

Figure 19: Peak positions (maxima) of the averaged radial distribution functions for spherical 3 nm (black circles), 5 nm (red squares) and 10 nm (blue up triangles) Au NPs as a function of temperature. Positions of the first peak d_1 (a), second peak d_2 (b), third peak d_3 (c) and fourth peak d_4 (d) were extracted from the averaged RDF plots.

distances due to significant background noises. To avoid such fitting errors, the peak positions in Fig. 19 were read from the 10-point averaging plots of the original RDF peaks at the maxima. As shown in Fig. 19, the first peak positions (d_1) of all three sizes decrease as temperature increases at $T < T_{melt}$, whereas d_2, d_3 and d_4 show positive trends. As concluded in the previous section that the simulated particles at all three sizes shows positive thermal expansion, it is easy to understand that the peak positions d_2, d_3 and d_4 increase as a function of temperature. The negative trend of the first peak positions indicated the balance resulting from the positive lattice expansion due to increasing vibrational energy and the (negative) contraction due to increasing local strain, which is also shown as decreasing coordination numbers as a function of temperature.

It is interesting that the RDF peak positions provide additional information of distinguishing the particle sizes. All the peaks except d_2 show that the peak positions shift up as size increased, and the difference among sizes slightly increased as temperature increased in general. It is most explicit in the first peak positions, where the shift-up in d_1 is about 3.5 % as size increases from 3 nm to 10 nm at moderate to high temperatures. The averaged lattice parameters d_2 overlap as size varied. A rough estimation of linear thermal expansion coefficient based on d_2 in the temperature range of 10 K to 880 K is 2.0×10^{-5} K^{-1}, in the same order of magnitude of the estimated α_L. For d_3 and d_4, the discrepancies between 3 nm and 5 nm were obviously larger than those between 5 nm and 10 nm, indicating the convergence of peak position as particle size approaching bulk.

3.3.3 Cubic Au NPs

Cubic Au particles containing (100) facets at all six surfaces were studied to compare with the spherical particles. To avoid confusion, the nominal size of the cubic particle defined in this work is the length of the side. By this definition, the cubes have far more atoms than the spheres having the same nominal sizes. As a result, the melting temperature of the cubic particle at a given size is significantly higher than the corresponding spheric one. As shown in Fig. 20, the corner atoms with low coordination numbers deform quickly as temperature increased from 10 K, forming small (111) facets at each corner. The (111) facets become one of the two dominating facets as temperature goes up to 1100 K, similar to the (111) and (100) dominated surfaces at 880 K for spherical 5 nm shown in Fig. 9 (i). At $T > T_{melt}$, the

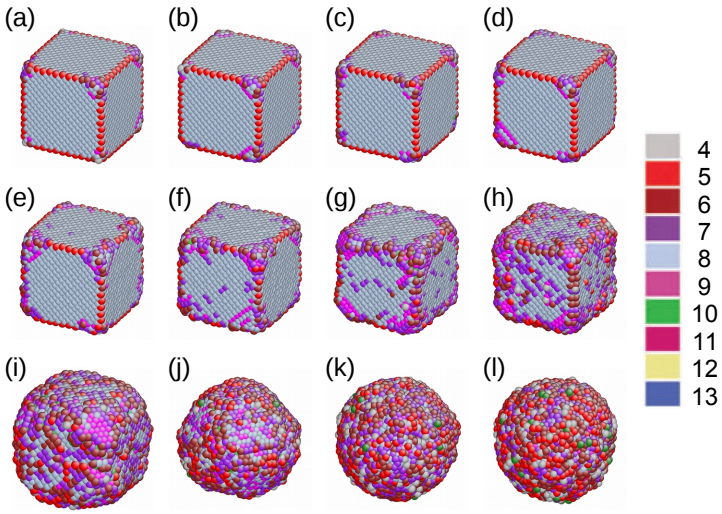

Figure 20: Views of cubic 5 nm Au NPs at 5.00 ns at 10 K (a), 50 K (b), 100 K (c), 150 K (d), 200 K (e), 300 K (f), 440 K (g), 660 K (h), 880 K (i), 1100 K (j), 1320 K (k) and 1540 K (l). Atoms were colored according to coordination numbers.

cubic shape completely disappears and becomes spherical, comparable to the amorphous structures from spherical particles. Similar trends are found in cubic 3 nm and 10 nm particles. Transitions from perfect cube to truncated octahedron-like structure with (111) and (100) dominated surfaces occur at lower temperatures in 3 nm particles.

The averaged energies over 1000 configurations for cubic 3 nm, 5 nm and 10 nm particles are shown in Fig. 21. Similar to the spherical particles, the energies (E) as a function of temperature for Au crystallines were fitted to $E_0 + a*T$, with fitted E_0 being -3.69, -3.79 and -3.86 eV/atom, and the fitted slope a being 1.19×10^{-4}, 1.39×10^{-4} and 1.45×10^{-4} in the unit of eV/K for 3 nm, 5 nm and 10 nm particles, respectively. The absolute value of fitted E_0 is slightly larger in cubic particle at the same nominal size comparing to spherical one due to increased number of atoms, which is consistent with the size-dependent trend. For the amorphous structures, the fitted E_0 is -3.73 and -3.79 eV/atom, and fitted slope a being 2.25×10^{-4} and 2.15×10^{-4} in the unit of eV/K for the cubic 3 nm and 5 nm particles, respectively. The absolute value of the fitted E_0 for crystalline-like particles is larger than that for the amorphous one, indicating the cubes are less stable than the spheres.

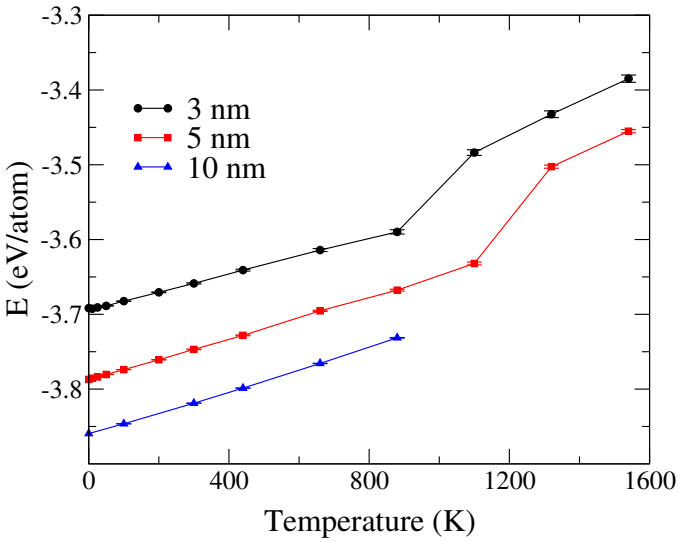

Figure 21: Energy of cubic 3 nm (black circles), 5 nm (red squares) and 10 nm (blue up triangles) Au NPs as a function of temperature.

Coordination Number. The coordination numbers in cubic 3 nm particles show two modes: 8 from surface atoms on (100) facets and 12 from core atoms at low temperatures, as shown in Fig. 22. Similar to spherical particles, the distribution of coordination numbers transforms from bimodal to monomodal as the particles transferred from crystalline to amorphous structures. Again, the coordination numbers of the amorphous particles at maximum shift down as temperature increases, indicating an increase in bond length. Similar transitions are observed in 5 nm and 10 nm cubic particles, as shown in Fig. 23 and Fig. 24, respectively.

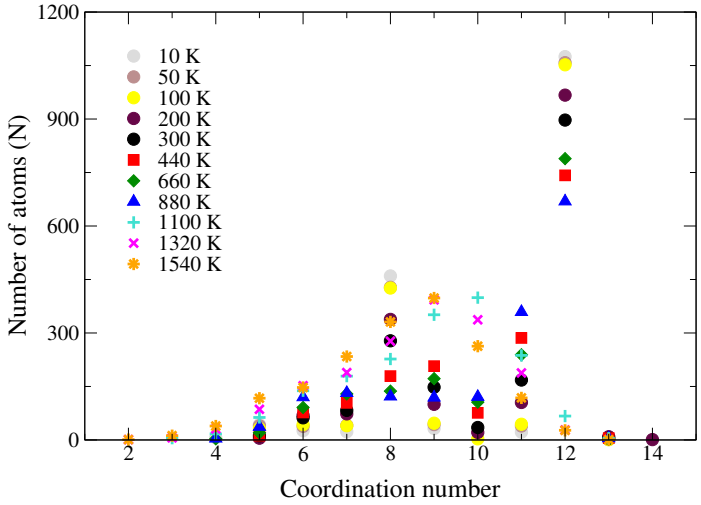

Figure 22: Coordination number of cubic 3 nm Au NPs at 10 K (grey circles), 50 K (brown circles), 100 K (yellow circles), 200 K (maroon circles), 300 K (black circles), 440 K (red squares), 660 K (green diamond), 880 K (blue up triangles), 1100 K (cyan pluses), 1320 (magenta crosses) and 1540 K (orange stars).

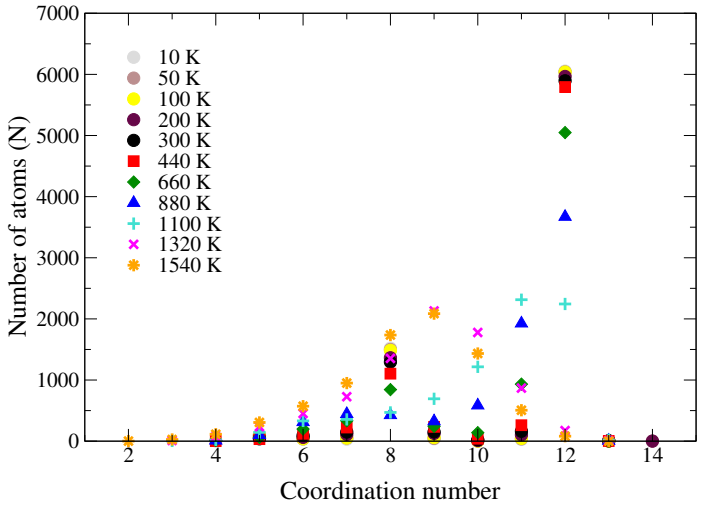

Figure 23: Coordination number of cubic 5 nm Au NPs at 10 K (grey circles), 50 K (brown circles), 100 K (yellow circles), 200 K (maroon circles), 300 K (black circles), 440 K (red squares), 660 K (green diamond), 880 K (blue up triangles), 1100 K (cyan pluses), 1320 (magenta crosses) and 1540 K (orange stars).

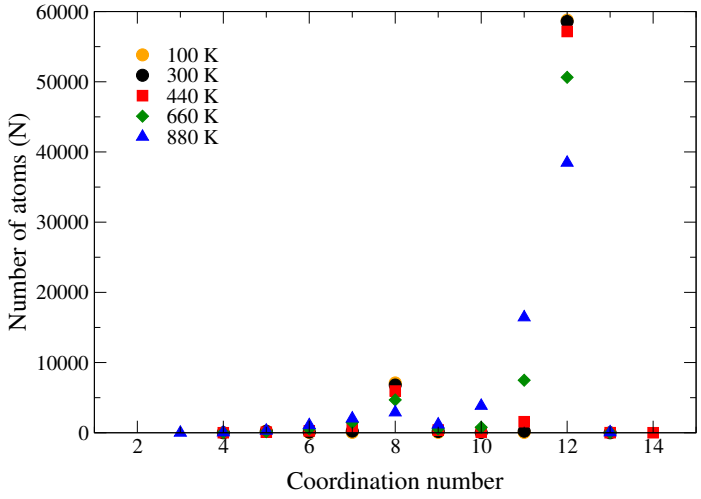

Figure 24: Coordination number of cubic 10 nm Au NPs at 100 K (orange circles), 300 K (black circles), 440 K (red squares), 660 K (green diamonds) and 880 K (blue up triangles).

Linear Thermal Expansion Coefficient. The mean interatomic distances of cubic Au particles were extracted following the same procedure as in spherical particles. Based on the previous analysis of spherical particles, the thermal response of cubic particles should be positive as a function of temperature as well. However, l_{miad} obviously failed to describe the positive thermal effect on cubic particles, as shown in Fig. 25. Accompanied with the structural transition from cubic to octahedron-like structure, l_{miad} decreases as temperature increases for 3 nm particle at all temperatures below melting point, and for 5 nm particles from 660 K to 1100 K. Severe geometry change overcomes the minor contribution from thermal expansion, resulting in dramatic decrease in l_{miad}. As a result, the calculated linear thermal expansion coefficient based on l_{miad} is totally unreliable, as shown in Fig. 26.

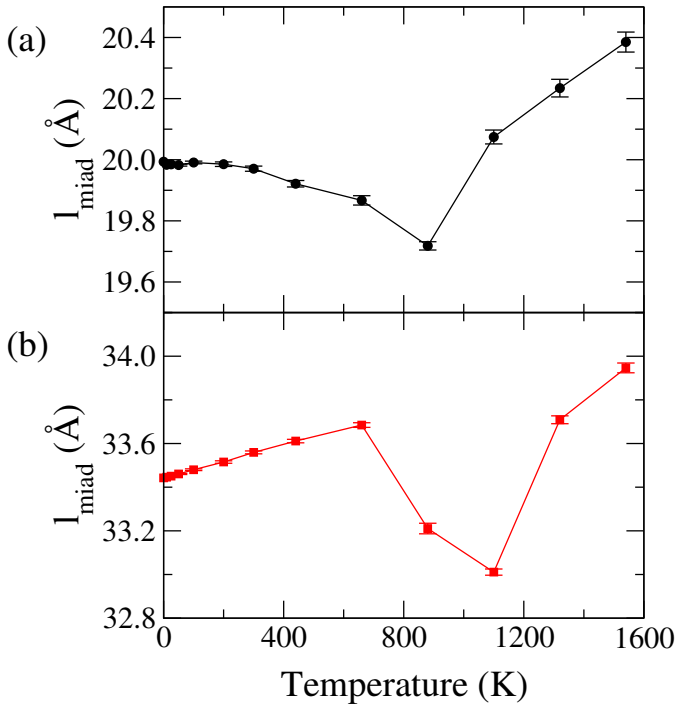

Figure 25: Mean interatomic distances of cubic 3 nm (black circles) and 5 nm (red squares) Au NPs as a function of temperature.

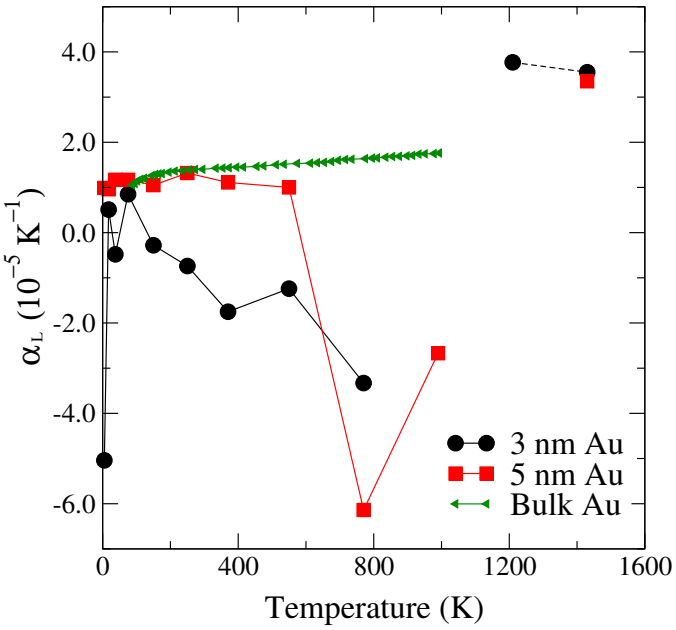

Figure 26: Linear thermal expansion coefficient (α_L) of cubic 3 nm (black circles) and 5 nm (red squares) Au NPs as a function of temperature. Experimental reference for bulk Au (green left triangles) reproduced from Nix and MacNair [2]. α_L at melting temperature region for each particle was omitted. Data points at $T < T_{melt}$ were connected with solid lines, those at $T > T_{melt}$ with dashed lines.

Radial Distribution Function. An alternative way to characterize the thermal effect in the cubic particles is to extract structural information from the RDF peaks. Fig. 27 shows the averaged RDFs of cubic 5 nm particle at varying temperatures. Although it is unfair to compare the RDFs of those from the spherical particles directly due to different number of atoms, the trends observed for the cubic particles are similar to those in the spherical NPs. Increases in d_2, d_3 and d_4 indicate thermal expansion in cubic particles. Although the peak positions of d_1, d_3 and d_4 increased as size increased, The difference in peak positions for 5 nm and 10 nm became much smaller in cubic particles, indicating the convergence to bulk value as size increases and possible difficulty in distinguishing particles with larger sizes. Nonetheless, the RDF peak positions successfully predict the similar thermal and size effects of the cubic particles comparing to the spherical particles.

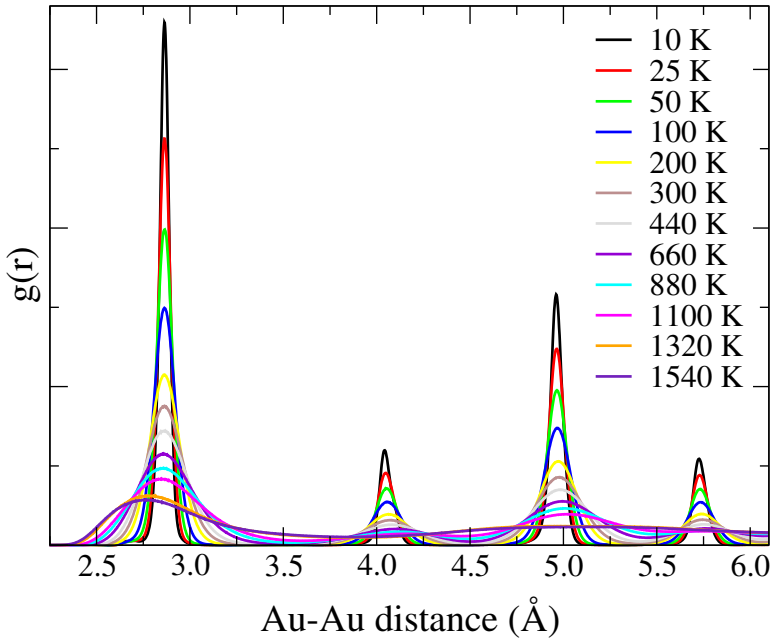

Figure 27: Averaged radial distribution functions of cubic 5 nm Au NPs at finite temperature. Peaks were averaged over 1000 configurations at each temperature.

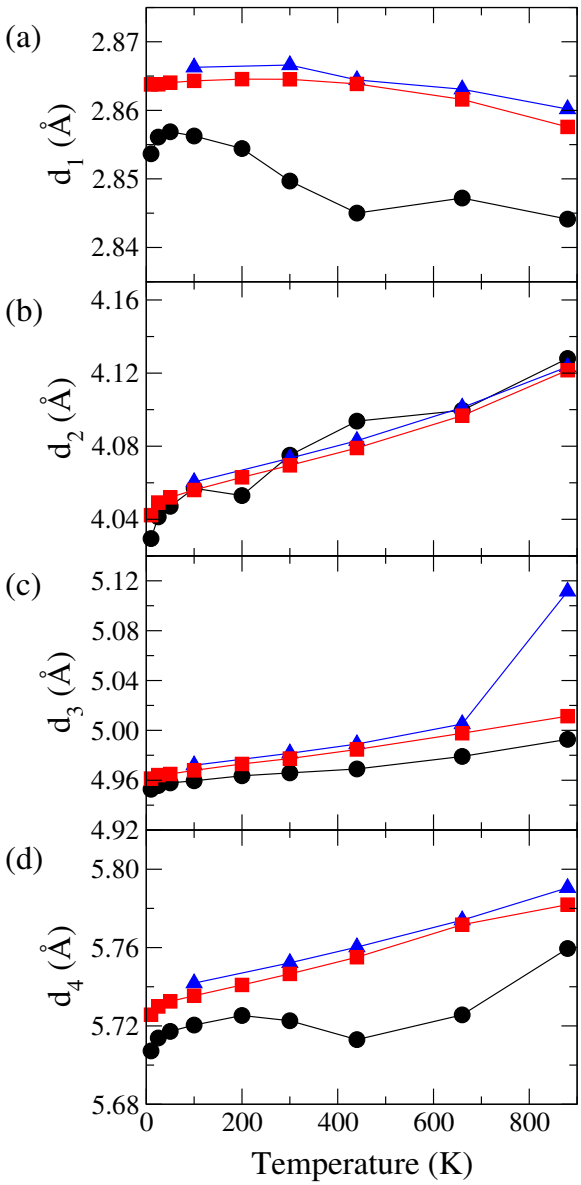

Figure 28: RDF peak positions of cubic 3 nm (black circles), 5 nm (red squares) and 10 nm (blue up triangles) Au NPs as a function of temperature. Positions of the first peak d_1 (a), second peak d_2 (b), third peak d_3 (c) and fourth peak d_4 (d) were extracted from the averaged RDF plots.

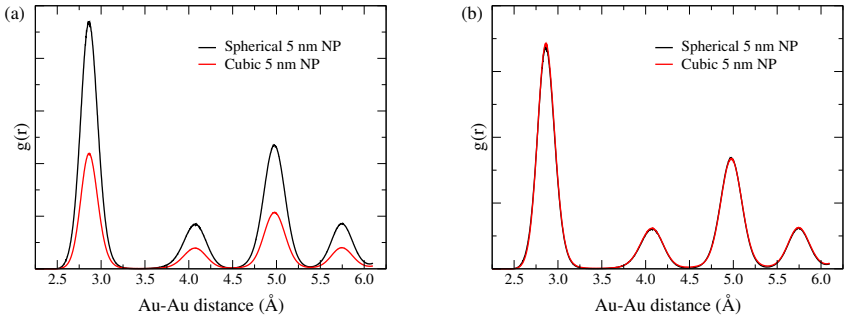

Figure 29: The original (a) and scaled (b) radial distribution functions of spherical 5 nm Au NP (black) and cubic 5 nm Au NP (red) at 300 K.

Finally, the RDFs of spherical 5 nm NP and cubic 5 nm NP at 300 K were compared in Fig. 29. Due to their different numbers of atoms, the original RDFs of spherical and cubic 5 nm differ in intensities, as shown in Fig. 29 (a). The intensity of the peaks was multiplied by the number of atoms for each particle, as shown in Fig. 29 (b). The peak positions of the original and scaled RDF peaks for spherical and cubic 5 nm NPs indicate negligible difference resulting from different shapes. The scaled RDF peaks almost overlap with each other, except a slight increase in peak intensity from cubic 5 nm particle, probably contributed from the corners in the cubes. In conclusion, the RDF peaks are an alternative way to characterize the nanostructures based on averaging structural information. Shift in peak positions reflects the effect of thermal expansion. However, RDF peaks provides little information of the shape, resulting in difficulties in differentiating the spherical and cubic NPs solely from RDFs.

3.4 Conclusion

The size-, temperature- and shape-dependent properties of Au particles up to 10 nm were investigated using a highly optimized EAM potential by Sheng, *et al* [15]. As size increases, the thermal properties approaches the bulk value due to less impact from the surface effect at finite sizes. For both spherical and cubic Au particles, the thermal effects on the structures are always positive, which is consistent with the experimental results on particle sizes of 5 nm or larger. The thermal contraction for 4 nm or smaller Au NPs at temperatures beyond a turnover point is contributed from the electron exci-

tation, and thus it is impossible to reproduce the same trend using classical force field potential that ignores the contribution from the excited electrons. First-principles based MD simulations are needed to further investigate the thermal behavior of small Au particles. Nonetheless, the MD simulations with the EAM potential are reliable for generating realistic atomic structures of sizes larger than 5 nm.

The structural analysis is based on coordination number distribution, mean interatomic distances, and radial distribution functions. Mean interatomic distances (l_{miad}) provide quantitative information to characterize the thermal effect and the size effect, leading to calculations of linear thermal expansion coefficients. However, l_{miad} is highly shape-dependent, which is only applicable for perfect spherical particles and/or for particles without shape deformation. The coordination number distribution reflects the changes in size, temperature, and shape, providing supplementary information for structural analysis, especially the coordinate-dependent bond length distribution at surface layers [46]. The radial distribution functions provide information on atomic density, which can be reliable for structural analysis. Extracted peak positions quantitatively characterize the thermal expansion of particles as a function of temperature and size, which are valid for both shapes. Should there exists reliable fittings to the RDF peaks, the analysis on the intensity and breadth of the RDF peaks would provide more information for structural characterization.

4 Nanoparticles for photocatalysis

This section was published in J. Phys. Chem. C 2015, 119 (9), 4834-4842 and partly in Catal. Sci. Technol. 2015, 20592064 (5).

4.1 Introduction

Noble metal nanoparticles in the range of a few nm to a few tens of nm often exhibit properties that are distinctively different from the bulk materials, and are useful in a wide variety of applications such as imaging, catalysis, biomedicine, etc. due to their tunable properties depending on size, shape and chemical composition. Physical or chemical processing, such as sonication[49], annealing[50], ligandation[51] and deposition on the substrate[52], may further modify the NP structures and functionalities. In particular, for catalytic applications, adsorption of the NPs on semiconductor or insulator substrates can play an important role in determining the overall catalytic activity of the combined system. It has been recently reported that semiconducting CdS nanorods or nanoparticles decorated with sub-nm and nm-sized noble metal clusters show promising applications in photocatalysis such as H_2 production under visible light [53, 54, 5, 55]. Interestingly, the catalytic activity for Pt clusters on CdS was observed to be significantly enhanced for a particular cluster size [55]. It was proposed that this cluster-size selectivity stems from the alignment of the lowest unoccupied molecular orbital (LUMO) of the cluster between the hydrogen reduction potential and the CdS conduction band edge (CB) based on the idea that photo-excited electrons are first transferred from CB of CdS to the cluster LUMO and then to the H^+ ions, both steps being downhill energetically. In order to evaluate the validity of this proposed model, it is necessary to understand not only the quantitative trend of the cluster electronic structure as a function of cluster size, but also very importantly the influence from the substrate. Furthermore, the adsorption of the metal cluster is also expected to modify the structural and electronic properties of the substrate, and in turn the energy level alignment at the cluster/substrate interface. Such cluster/support interactions are additionally subject to the influence of finite temperature [56] and chemical environment [57, 58], which adds to the complexity of the surface reactions environment.

Several density functional theory (DFT) studies on supported noble metal clusters have been reported previously [59, 60, 58]. The adsorption of Ag

atom and small Ag_N clusters ($N = 2, 4, 7$) on polar CdS surfaces was studied [59], and the computed adsorption energy on the Cd-terminated (0001) surface ranges from -2.5 eV (Ag_1) to -4.6 eV (Ag_7). The adsorption-induced work function shifts of the Cd-terminated (0001) and S-terminated $(000\bar{1})$ surfaces were found to be of opposite signs, consistent with the relation of Pauli electronegativity of S < Ag < Cd. Whereas similar adsorption studies of sub-nm Pt clusters on CdS have not been reported in the literature, the atomic structure of a Pt_{246} nanoparticle adsorbed on the nonpolar CdS $(10\bar{1}0)$ surface was studied using *ab initio* molecular dynamics simulations [60], which revealed a strong bonding accompanied by atomic diffusion of substrate atoms into the Pt cluster, in contrast with the much weaker interaction found between CdS and the amorphous or epitaxial slab of Pt. In addition, profound substrate effects have been observed on the atomic structure of the supported noble metal clusters. For example, a dispersion-corrected DFT study of Pt cluster on graphite [61] showed that van der Waals interactions contribute significantly to the overall adsorption energy and, despite its weak nature, dramatically influence the structure (e.g., expansion and wetting) and electronic properties (e.g., enhanced metallicity) of the supported Pt clusters. A recent study that combines DFT calculations with high-resolution TEM and extended X-ray absorption fine structure spectroscopy [58] also revealed a strong dependence of the crystallinity and energetic stability of the supported Pt cluster on the supporting materials (graphene or γ-Al_2O_3) and adsorbate (H_2).

In this Chapter, we investigate the adsorption characteristics of supported Pt clusters on CdS surface as a first step toward understanding the enhanced photocatalytic activity at the cluster/semiconductor interface. We focus on CdS-supported Pt clusters of approximately 1 nm in size, which were found by several experiments to be most active for photocatalytic hydrogen production[5, 62, 55]. In particular, we examine the influence from the cluster size and shape on the adsorption geometry and energetics, and analyze in detail the structural deformation on both the cluster and the substrate, as well as the influence on their electronic structures. For comparison, systematic studies of unsupported Pt cluster up to 1.5 nm were also carried out. Our results indicate that realistic structural models which explicitly treat the interactions between the clusters and the substrate are essential for properly describing the electronic structure at the interface and better understanding the role of Pt clusters in improving reactivity of CdS towards photocatalytic water splitting.

4.2 Computational Methods

Spin-polarized DFT calculations were carried out using the Vienna ab initio simulation package (VASP) [27, 28] within the generalized gradient approximation with the Perdew-Burke-Ernzerhof (PBE) exchange-correlation functional [24]. The projected augmented wave (PAW) method [63] and a kinetic energy cutoff of 400 eV were used. Geometry optimization was performed without any symmetry constraint until the total energy and the ionic forces were converged to 10^{-6} eV and 10 meV/Å, respectively. For selected systems, we examined the spin-orbit coupling (SOC) effect as implemented in VASP by Kresse and Lebacq. [27, 28]

The computed lattice constant and cohesive energy of bulk face centered cubic (fcc) Pt are 3.97 Å and 5.57 eV, in good agreement with experimental values of 3.92 Å [8] and 5.84 eV [64], respectively. To probe the structural and electronic features of Pt clusters in the sub-nm to nm range, unsupported Pt clusters with diameter of 0.7-1.5 nm in both 2D bilayer and 3D structures were investigated. The 3D structures of Pt_N (N = 13, 38, 55, 85, 140) adopting the truncated octahedron shape (O_h symmetry) were generated by truncating along the (111) and (100) planes of bulk Pt. These 3D Pt clusters were further truncated along the (111) plane to obtain the corresponding bilayer structures of Pt_N (N = 10, 19, 31, 46). For a given size the structure adopted in this work does not necessarily correspond to the most stable one as has been found, for example, for Pt_{38} and Pt_{55} which possess lower symmetry in the lowest-energy configurations[65, 66]. Nevertheless, the cluster structures adopted here are convenient for investigating the general influence of shape and size on the adsorption geometry, energetics, and interface electronic properties. In addition, we have estimated the vertical ionization potential (IP) and electron affinity (EA) by computing the total energy differences between neutral and charged Pt clusters. For the Pt atom, IP and EA were estimated as 9.52 eV and 2.16 eV, in comparison to the measured values of 8.96 eV [67] and 2.13 eV [68], respectively.

The calculated bulk lattice constants of wurtzite CdS are 4.20 Å and 6.84 Å, which are within 2% of the experimental parameters of 4.14 Å and 6.71 Å [69], respectively. As is common for (semi-) local exchange-correlation functionals, PBE severely underestimates the band gap, yielding direct band gap of 1.10 eV at the Γ-point compared to the experimental gap of 2.42 eV [70]. Clean nonpolar $(10\bar{1}0)$ and $(11\bar{2}0)$ surfaces are modeled using the symmetric periodic slab model of 8 atomic layers, with $9 \times 6 \times 1$ and $6 \times 6 \times 1$

k-grids, respectively. At least 20 Å of vacuum space is inserted to separate slabs in neighboring supercells. Dependence of the surface energy and band gap on the slab thickness is examined by varying the number of atomic layers (n_L) from 4 to 28. The adsorption of Pt clusters on CdS($10\bar{1}0$) is modeled using a (5×3) surface unit cell with a single Γ-point for the Brillouin zone sampling. The bottom four layers are fixed at their bulk positions while the top four atomic layers and the adsorbate are fully relaxed. The broken symmetry of the slab leads to a net surface dipole moment of $\mu^0_{CdS} = -7.4$ Debye for the relaxed surface in the absence of the adsorbate.

4.3 Results and Discussion

4.3.1 Unsupported Pt clusters

We first study the structural and energetic properties of unsupported Pt clusters and their dependence on the cluster size and shape. As shown from the relaxed geometries (Fig. 30), the bilayer structure of the 2D clusters are preserved except for Pt_{10}, which relaxes into a more stable 3D structure. Overall, the intra-layer bonds and inter-layer bonds at the cluster edges contract by up to 0.3 Å relative to the computed bulk value, whereas the rest of the interlayer bonds expand by up to 0.5 Å. For 3D Pt clusters, similar trends can be observed within and between (111) layers, but the bond length variations are less severe (within ±0.2 Å). The average Pt-Pt bond length in 2D and 3D Pt clusters increases towards the bulk value (2.81 Å) as the cluster size increases.

Fig. 31 illustrates the computed cohesive energy per atom (E_{coh}), which increases monotonically with cluster size. E_{coh} can be roughly fitted to $E_0 + AN^{-\alpha}$ with the choice of α based on the approximate perimeter-to-area ratio for 2D structures ($N^{-\frac{1}{2}}$) and surface-area-to-volume ratio for 3D structures ($N^{-\frac{1}{3}}$), respectively. The fitting parameter E_0 corresponds to the cohesive energy at the limit $N \to \infty$. $E_0^{2D} = 5.2$ eV is slightly larger than the computed E_{coh} of a periodic bilayer of Pt(111) (5.0 eV). Similarly, $E_0^{3D} = 5.9$ eV is higher than the computed bulk cohesive energy (5.6 eV). The discrepancies are caused partly by the small sampling size of the clusters, and partly by the numerical errors from directly comparing total energies of isolated systems with those of periodic systems (with different k-point sampling and choice of supercells). It was reported [71] that the SOC effect plays an important role in determining energetics of Pt clusters, and the inclusion of SOC

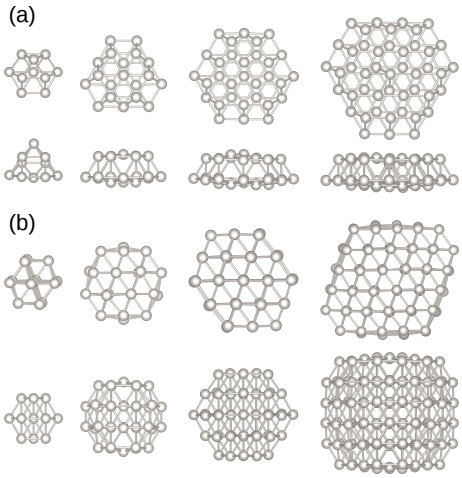

Figure 30: Top and side views of optimized Pt_N clusters of (a) 2D bilayer structures (N = 10, 19, 31, 46) and (b) 3D structures (N = 13, 38, 55, 140).

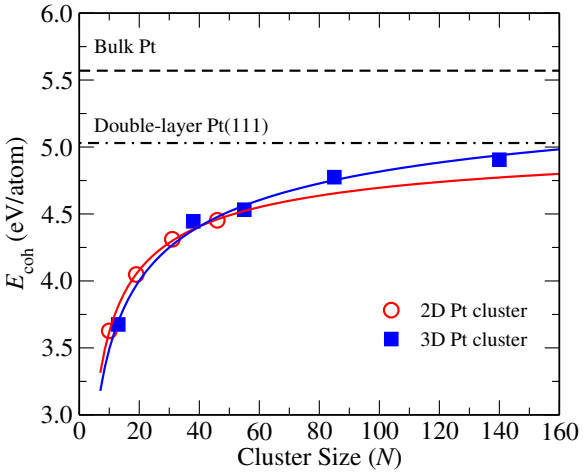

Figure 31: The computed cohesive energies ($E_{\rm coh}$) as a function of cluster size (N) for 2D bilayer structures (empty circles) and 3D structures (filled squares) of Pt_N. The solid lines represent fitting of $E_{\rm coh}$ to E_0+$AN^{-\alpha}$ for 2D ($\alpha = \frac{1}{2}$) and 3D ($\alpha = \frac{1}{3}$) structures, with fitted parameter E_0= 5.2 eV (2D) and 5.9 eV (3D). Horizontal dashed line and dashed-dotted line correspond to computed $E_{\rm coh}$ of a periodic double-layer Pt(111) slab (5.0 eV) and of bulk Pt (5.6 eV), respectively.

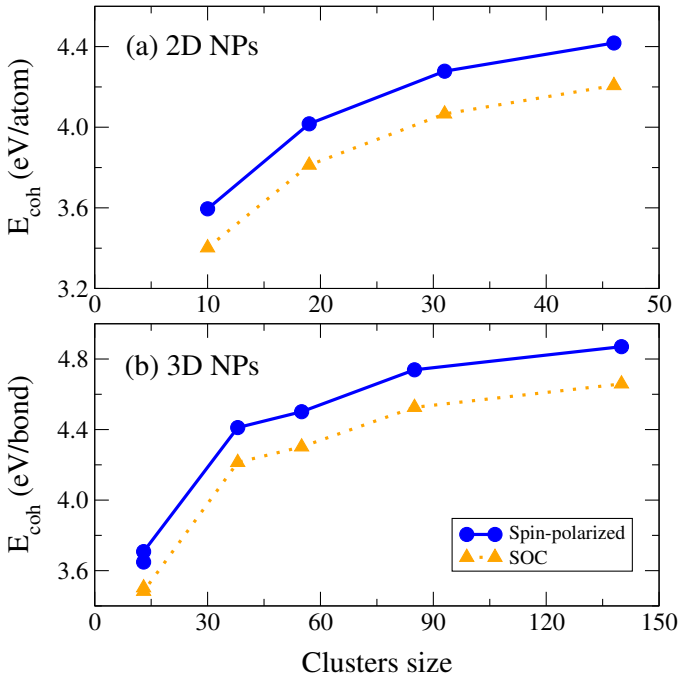

Figure 32: Computed cohesive energy (E_{coh}) for 2D and 3D structures of Pt clusters obtained from spin-polarized calculations with (orange triangles) or without (blue circles) inclusion of spin-orbit coupling effects.

effect systematically decreases $E_{\rm coh}$. Indeed, we found the same trend for all Pt clusters examined (Fig. 32), in good agreement with previous results on smaller Pt_N clusters ($N = 2 - 6$)[71]. In particular, the total energy of a single Pt atom decreases by 0.63 eV and that of Pt clusters decreases by 0.41-0.46 eV when SOC is included, resulting in an almost constant reduction of $E_{\rm coh}$ by 0.2 eV for both 2D and 3D Pt clusters. The subtle difference of SOC effects may also change the energetic ordering of isomers. For example, Pt_{13} was found to be more stable when adopting in the D_{4h} symmetry than in the O_h symmetry without SOC with $\Delta E_{\rm coh} = 61$ meV; with SOC the trend is reversed with $\Delta E_{\rm coh} = -11$ meV.

Estimates of the electron removal and addition energies of the Pt clusters, or equivalently IP and EA, are an important factor in determining the interfacial energy level alignment with the substrate. Fig. 33 shows the computed IP and EA as functions of the cluster size (N), which roughly fall on the curves $\Phi_0 + BN^{-1/3}$. The power law of $N^{-1/3}$, or equivalently

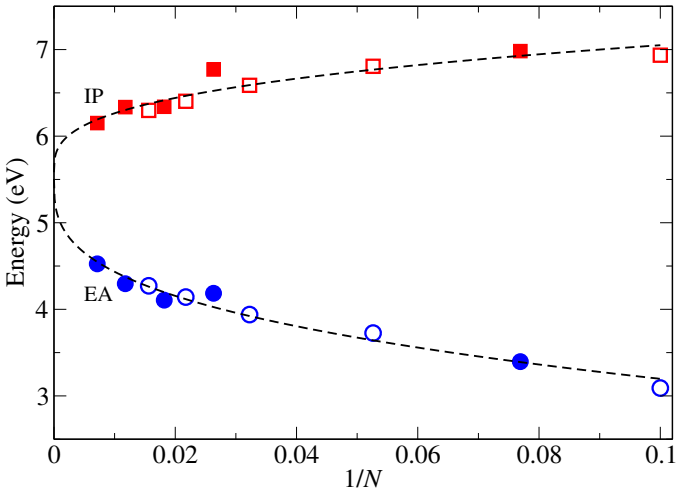

Figure 33: Computed ionization potential (IP, red squares) and electron affinity (EA, blue circles) of Pt clusters as a function of cluster size. Open and filled symbols represent 2D and 3D structures, respectively; dashed lines are fittings to $\Phi + BN^{-1/3}$.

R^{-1} for 3D clusters, is consistent with the liquid-drop model of metal clusters [72] in which the asymptotic expressions for IP and EA take the form IP= $\Phi + c_1 e^2/R$ and EA= $\Phi - c_2 e^2/R$, where Φ is the bulk work function. The fitted parameters from Fig. 33, $\Phi_0^{\rm IP}$=5.58 eV and $\Phi_0^{\rm EA}$=5.50 eV, are in excellent agreement with work functions of low-index Pt surfaces computed from DFT [73], $\Phi_{(111)} = 5.69$ eV and $\Phi_{(100)} = 5.66$ eV. As will be shown later, the adsorption on the CdS surface modifies the cluster structure, and in turn its IP and EA.

The density of states (DOS) of 2D and 3D Pt clusters become discrete as size decreases, as shown in Fig. 34. States in black are for spin-up, red for spin-down. Filled states (up to Fermi level) are shown in solids, empty states in hollows. The finite small band gap near Fermi level at small clusters approaches zero as size increases.

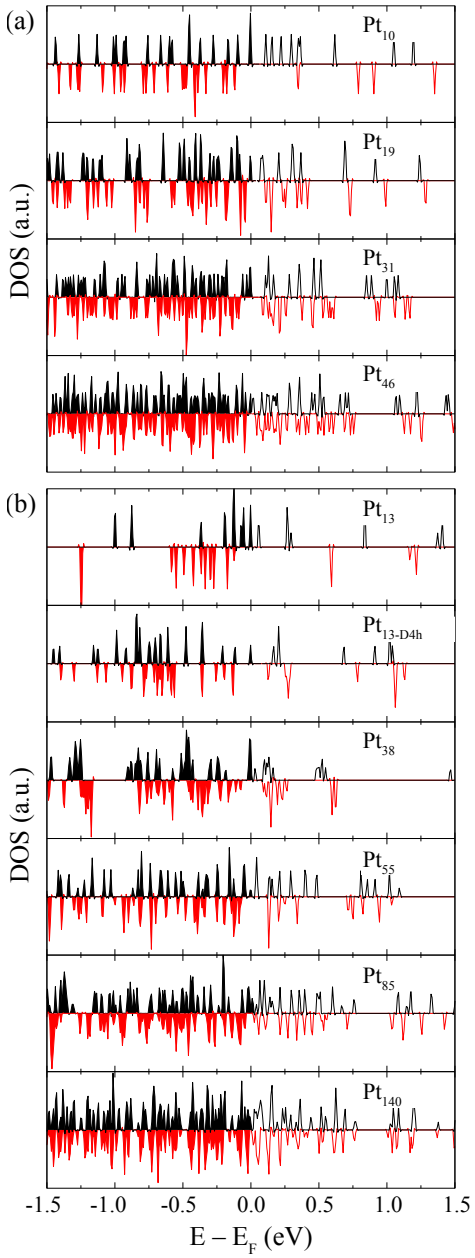

Figure 34: Computed density of states (DOS) of bare 2D (a) and 3D (b) Pt clusters.

4.3.2 Low Index CdS Surfaces

The structures of relaxed clean CdS $(10\bar{1}0)$ and $(11\bar{2}0)$ surfaces are shown in Fig. 35. Significant atomic displacements are observed for the under-coordinated surface atoms in which S atoms move towards the surface and Cd atoms move away from the surface. The extent of the displacement decays moving away from the surface. For instance, the average displacement of an 8-layer CdS$(10\bar{1}0)$ slab is 0.65 (0.20) Å for the unsaturated Cd (S) atoms in the top layer, and only 0.19 (0.07) Å in the second layer. The displacements at subsequent layers are reduced to below 0.1 Å. For the convenience of discussion, we label Cd and S atoms at the top two layers of CdS$(10\bar{1}0)$ as shown in Fig. 35. The lateral distance between Cd and S atoms along [0001] direction (denoted as x) are $D_{12,x}$ = 2.32 Å, $D_{13,x}$ = 0.69 Å and $D_{14,x}$ = 3.53 Å; the perpendicular distance along $[10\bar{1}0]$ direction (denoted as z) are $D_{12,z}$ = 0.76 Å, $D_{13,z}$ = 1.25 Å, $D_{14,z}$ = 1.46 Å. These results are in good agreement with previously reported values [74] of 2.29 Å, 0.65 Å, 3.50 Å, 0.78 Å, 1.31 Å and 1.57 Å calculated using DFT/PBE. Similar trend of atomic displacements was found for the CdS$(11\bar{2}0)$ surface.

Next we examine the influence of the finite slab thickness on the surface

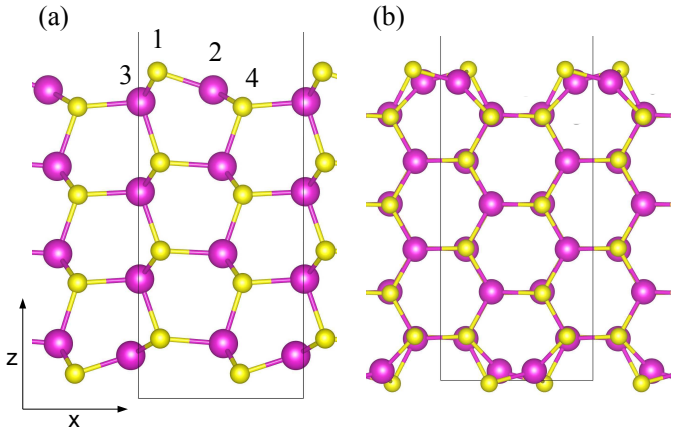

Figure 35: Side views of relaxed (a) nonpolar $(10\bar{1}0)$ and (b) $(11\bar{2}0)$ CdS surfaces. The magenta and yellow spheres represent Cd and S atoms, respectively. The same color scheme is used throughout the paper. The black frames define the boundary of the unit cells.

energy and band gap. The surface energy is defined as:

$$\gamma = \frac{E_{\text{slab}} - nE_{\text{bulk}}}{2S_0} \tag{55}$$

where E_{slab} is the total energy of a slab with n CdS formula units and E_{bulk} is the total energy of the bulk crystal per CdS formula unit. S_0 is the surface area of the slab and the factor of 2 accounts for the two surfaces of the slab. In order to avoid the divergence problem with computing surface energy from separately computed slab and bulk energies, we used the method suggested by Fiorentini and Methfessel [75] and extracted E_{bulk} from a linear fitting of E_{slab} as a function of the slab thickness n_{L}. The calculated surface energy converges rapidly with n_{L}, as shown for the $(10\bar{1}0)$ surface in Fig. 36(a). The converged surface energies are $\gamma_{(10\bar{1}0)} = 20.2$ meV/Å^2 and $\gamma_{(11\bar{2}0)} = 20.0$ meV/Å^2. These values agree with the previously reported data of 20.3 meV/Å^2 and 19.7 meV/Å^2 using PW91[76]; however, the energetic order of $\gamma_{(10\bar{1}0)}$ and $\gamma_{(11\bar{2}0)}$ is opposite to that obtained by Barnard et al.[74] using PBE, where $\gamma_{(10\bar{1}0)} = 17.5$ meV/Å^2 and $\gamma_{(11\bar{2}0)} = 18.1$ meV/Å^2, perhaps due to difference in slab thickness and the procedure of estimating E_{bulk}. The averaged surface energy for the polar (0001) and $(000\bar{1})$ surfaces of CdS has been previously estimated as 56.2 meV/Å^2 [74], about three times larger than that of the nonpolar surfaces. Since we are most interested in dominating facets of CdS nanostructures used in photocatalytic applications [55, 62, 5], we chose the CdS$(10\bar{1}0)$ surface in our adsorption studies of the Pt/CdS systems because of its low surface energy and relatively simple structure.

Fig. 37 displays the total and projected density of states (DOS) of bulk CdS and that of the $(10\bar{1}0)$ and $(11\bar{2}0)$ surfaces evaluated at $n_{\text{L}} = 8$. All three DOS plots look similar, and the valence and conduction band edge states are dominated by S p orbitals and Cd s orbitals, respectively. The computed gaps are 1.10, 1.35 and 1.48 eV for bulk, $(10\bar{1}0)$ and $(11\bar{2}0)$, respectively. A closer inspection of the projected DOS of the $(10\bar{1}0)$ surface (Fig. 37(b)) reveals the existence of surface states arising from the filled S p dangling bonds, which reside below the Fermi level and slightly above the bulk-like valence band maximum (VBM). The computed band gap, E_{g}, of the CdS$(10\bar{1}0)$ surface as a function of the slab thickness is plotted in Fig. 36(b) for $n_{\text{L}} = 4$-28. The extrapolated band gap for an infinitely thick slab, $E_{\text{g}}^{\infty} = 0.9$ eV, is slightly smaller than the computed bulk gap of 1.1 eV, perhaps due to the surface relaxation effects and the existence of the in-gap surface states.

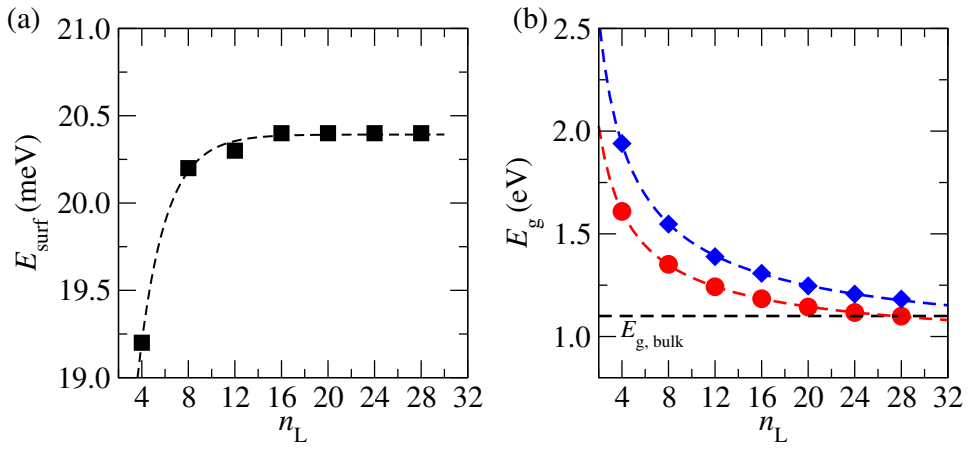

Figure 36: Computed (a) surface energy and (b) band gap of the CdS($10\bar{1}0$) surface as a function of the slab thickness n_L. Filled diamonds and circles correspond to energy gap from the bulk-like VBM state and surface state to the CBM state, respectively.

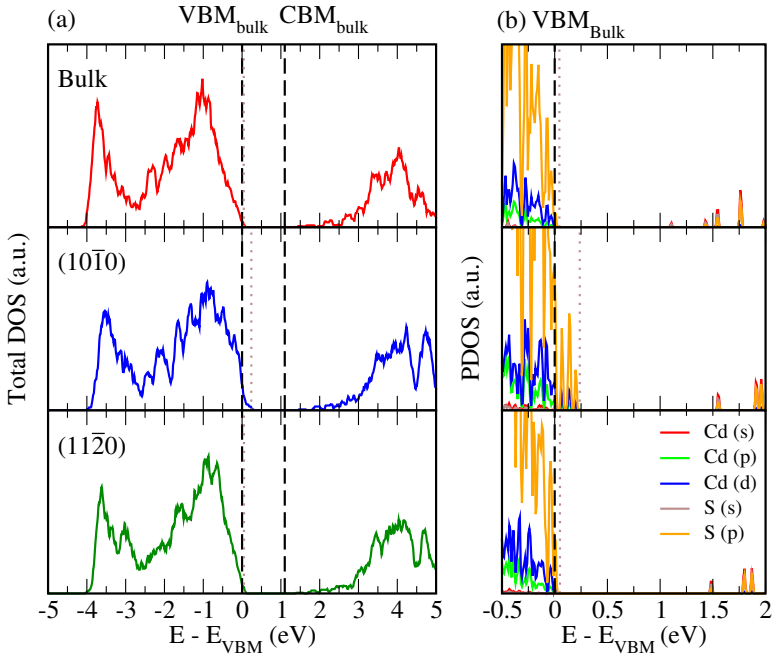

Figure 37: The (a) total and (b) projected density of states (DOS) of bulk CdS, the (10$\bar{1}$0) surface, and the (11$\bar{2}$0) surfaces. The DOS plots are aligned such that $E = 0$ correspond to the position of the bulk-like VBM states, whereas the vertical dotted lines indicate the Fermi level for each case. $n_{\mathrm{L}} = 8$ for the surface slabs.

4.3.3 Adsorption of Pt clusters on CdS surface

We study the adsorption characteristics of Pt_{19} and Pt_{38}, both of which are approximately 1 nm in diameter and correspond to the dominating size found in recent experiments of photocatalytic H_2 evolution [5]. Despite the similar lateral size, the interface area and the interaction strength may differ significantly due to the different dimensionality (Pt_{19}: 2D bilayer; Pt_{38}: 3D O_h symmetry). A 8-layer slab of the nonpolar CdS$(10\bar{1}0)$ is chosen as the substrate, and the Pt clusters are placed on above the slab with different initial position and orientation. In most configurations, the (111) plane of the Pt clusters is placed parallel to CdS surface, since it is the most abundant facet of Pt nanoparticles and also has the largest surface area in both clusters. We have also examined configurations in which the (111) or (100) plane is tilted such that it is parallel to the relaxed surface CdS bonds, labeled as $T_{1,2}$ in Fig. 40 and Fig. 43. For comparison, adsorption of a single Pt atom (Pt_1) is also considered, as shown in Fig. 38 and Fig. 39. The adsorption energy, $E_{\rm ad}$, is defined as

$$E_{\rm ad} = E_{{\rm Pt}_N/{\rm CdS}} - (E_{{\rm Pt}_N} + E_{\rm CdS}) \tag{56}$$

where the terms on the right hand side correspond to total energies of Pt_N/CdS$(10\bar{1}0)$, of the unsupported Pt_N cluster, and of the clean CdS$(10\bar{1}0)$ surface, respectively. The SOC effect was found to have a negligible influence on $E_{\rm ad}$ and therefore was ignored in adsorption studies presented below. The structural deformation of the substrate is quantified via $E_{\rm def,CdS}$, the total energy difference between the surface in the adsorption geometry and the clean surface. The deformation energy of the cluster $E_{\rm def,Pt}$ is similarly defined. The adsorption configurations presented below are by no means exhaustive or most stable. Nevertheless, these results clearly demonstrate the influence of cluster size, shape, and adsorption configurations on the adsorption energetics and the overall interface electronic structures as will be discussed in detail below.

Pt_1/CdS$(10\bar{1}0)$. The energetic and structural properties of different configurations (displayed in Fig. 39) of a single Pt atom adsorbed on CdS$(10\bar{1}0)$ are summarized in Table 2. Starting from ten different initial adsorption positions (see Fig. 38(a)), each adsorption system relaxes into one of four stable configurations as shown in Fig. 38(b). Config. A, in which the Pt adsorbs on the S-S bridge site and form two Pt-S bonds and one Pt-Cd bond, is found to be most stable with $E_{\rm ad} = -4.1$ eV. The other three configurations

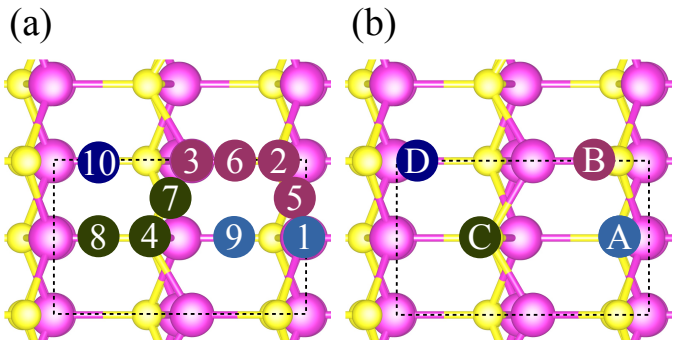

Figure 38: Top views of (a) initial and (b) final adsorption positions of Pt_1 on $CdS(10\bar{1}0)$.

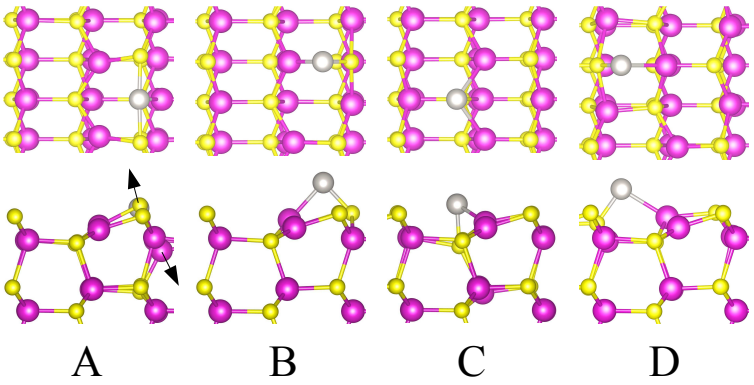

Figure 39: Top and side views of relaxed geometries of $Pt_1/CdS(10\bar{1}0)$. Black arrows in "A" indicate the Cd and (two) S atoms bonded to the adsorbed Pt atom, which is blocked by the S atoms and cannot be seen.

have only a single Pt-S bond and values of E_{ad} are higher by about 1 eV. The binding energy in Pt-S, Pt-Cd and Cd-S dimers are estimated from our DFT calculations to be 4.8 eV, 1.4 eV, and 1.2 eV, respectively. Although the chemical environment is different for the dimers and the Pt_1/CdS system, we expect a similar trend of the inter-atomic binding energies. As such, the stability of config. A can be understood from the fact that it contains the most Pt-S bonds. The bond lengths in the adsorption systems, $\langle d_{Pt-S} \rangle = 2.2 - 2.3$ Å and $\langle d_{Pt-Cd} \rangle = 2.6 - 2.8$ Å, are slightly larger than the calculated values of 2.05 Å and 2.50 Å for the dimers.

Upon Pt_1 adsorption there is also structural deformation in the CdS sur-

Table 2: Energetics and structural properties of $Pt_1/CdS(10\bar{1}0)$. E_{ad} is the adsorption energy; $E_{def,CdS}$ is the deformation energy with respect to the clean surface. $\langle d \rangle$ is the bond length averaged over the number of bonds (n) formed at the interface. $\Delta\mu_{tot}$ and $\Delta\mu_{CdS}$ denote changes in the total and substrate dipole moment normal to the surface in the adsorption geometry relative to that of the clean surface. All energies are in eV, dipole moments in Debye, and bond lengths in Å.

	A	B	C	D
E_{ad}	-4.1	-3.1	-3.1	-2.9
$E_{def,CdS}$	1.9	1.2	0.6	0.8
$\langle d_{Pt-S} \rangle$ (n_{Pt-S})	2.30 (2)	2.15 (1)	2.19 (1)	2.16 (1)
$\langle d_{Pt-Cd} \rangle$ (n_{Pt-Cd})	2.56 (1)	2.59 (1)	2.74 (2)	2.79 (1)
$\Delta\mu_{tot}$	-1.2	0.4	0.3	0.9
$\Delta\mu_{CdS}$	-1.7	0.3	0.9	1.1

face. It can be observed from Table 2 that $E_{def,CdS}$ follows roughly the trend of E_{ad}, suggesting that the surface tends to deform to a larger degree in order to accommodate more and/or stronger bonds with the Pt atom. For example, in config. A, the two S atoms bonded to the Pt atom are pushed up towards the surface whereas the Cd atom is pushed down away from the surface (see Fig. 39), leading to a deformation energy as large as 2 eV. Such atomic movement also results in a negative surface dipole moment relative to that of the clean surface, with $\Delta\mu_{CdS} = \mu_{CdS} - \mu^0_{CdS} = -1.7$ Debye. In contrast, a positive $\Delta\mu_{CdS}$, although smaller in magnitude, is observed in configs. B, C, and D. In addition, electron transfer between Pt_1 and the surface leads to an induced dipole moment μ_{ind}. In config. A, the positive value of μ_{ind} indicates that electrons are transferred from Pt to CdS, which is consistent with the formation of two Pt-S bonds and the relatively larger electronegativity of S than Pt. The trend is opposite in config. C, which can be explained by the formation of two Pt-Cd bonds and the smaller electronegativity of Cd than Pt. Configs. B and D both have one Pt-S bond and one Pt-Cd bond, and therefore much smaller μ_{ind}. The total dipole moment relative to μ^0_{CdS}, defined as $\Delta\mu_{tot} = \mu_{ind} + \Delta\mu_{CdS}$, varies from -1.2 to 0.9 Debye and contains contributions from both the structural deformation of the substrate and the electron transfer at the interface.

Pt_{19}/CdS(10$\bar{1}$0). Next we examine the Pt_{19}/CdS(10$\bar{1}$0) system (displayed in Fig. 40), and the adsorption energetics, structural properties, and dipole moments are summarized in Table 3. The computed E_{ad} are -10.6, -7.6, -9.2, -6.4, -10.1 and -8.6 eV for C_1, C_2, C_3, C_4, C_5, and T_1, while the total number of Pt-S (Pt-Cd) bonds are 10 (13), 6 (12), 9 (15), 4 (3), 8 (16) and 8 (10), respectively. Again a clear correlation between the formation of interfacial bonds and the overall energetic stability of the adsorption system can be observed. The adsorption energy per unit area can be roughly estimated assuming a contact area of 40 Å for the 12-atom bottom layer of Pt_{19}, and the calculated values of -0.16 to -0.27 eV/Å^2 is consistent with the reported DFT result of -0.23 eV/Å^2 for Pt_{246} on CdS(10$\bar{1}$0) [60]. The average bond lengths, $\langle d_{Pt-S} \rangle$ = 2.3 Å and $\langle d_{Pt-Cd} \rangle$ = 2.8 Å, are consistent with those of Pt_1/CdS(10$\bar{1}$0), and $\langle d_{Pt-Pt} \rangle$ = 2.7 Å is similar to that of the unsupported Pt_{19}. However, as illustrated for configs. C_1 and C_4 in Fig. 41, which correspond to the maximum and minimum magnitude of E_{ad} respectively, the distribution of d_{Pt-Pt} becomes significantly broader after adsorption, indicating a decrease in local crystallinity similar to the case of supported Pt_{37} on γ-Al_2O_3 [58].

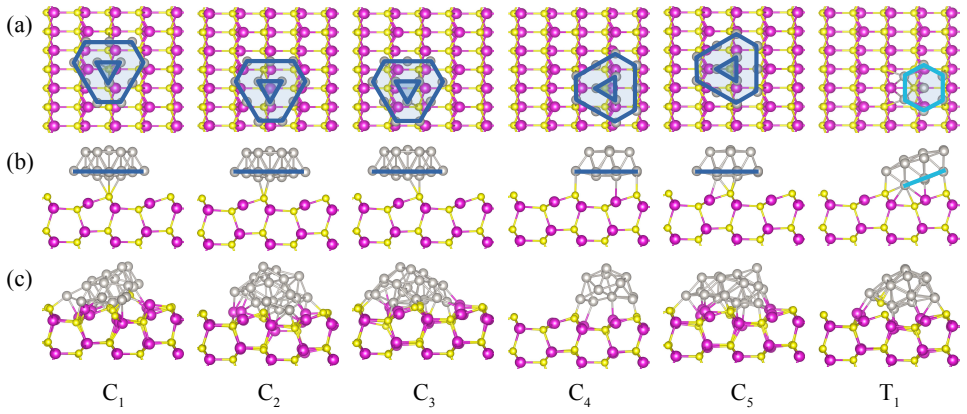

Figure 40: (a) Top and (b) side views of starting geometries of Pt_{19} on CdS(10$\bar{1}$0). (c) Side views of relaxed geometries.

Table 3: Energetics and structural properties of $Pt_{19}/CdS(10\bar{1}0)$. Definition of symbols is the same as in Table 2. $\mu_{Pt_{19}}$ denotes the dipole moment of Pt cluster normal to the surface in the adsorption geometry.

	C_1	C_2	C_3	C_4	C_5	T_1	T_1'
E_{ad}	-10.6	-7.6	-9.2	-6.4	-10.1	-8.6	-10.9
$E_{def,CdS}$	11.3	6.1	8.8	1.8	8.1	9.0	12.3
$E_{def,Pt}$	2.0	0.2	2.9	0.9	2.1	0.9	7.9
$\langle d_{Pt-Pt}\rangle$ (n_{Pt-Pt})	2.71 (52)	2.70 (54)	2.75 (55)	2.69 (53)	2.73 (53)	2.73 (54)	2.70 (47)
$\langle d_{Pt-S}\rangle$ (n_{Pt-S})	2.31 (10)	2.31 (6)	2.31 (9)	2.28 (4)	2.29 (8)	2.31 (8)	2.29 (10)
$\langle d_{Pt-Cd}\rangle$ (n_{Pt-Cd})	2.78 (13)	2.84 (12)	2.83 (15)	2.77 (3)	2.83 (16)	2.79 (10)	2.80 (17)
$\Delta\mu_{tot}$	-1.4	-1.2	-2.1	-1.0	-1.7	-2.6	-2.1
$\Delta\mu_{CdS}$	1.8	3.1	2.6	1.0	3.5	-1.7	-2.3
$\mu_{Pt_{19}}$	-0.8	-0.1	-1.6	-1.3	-1.1	0.0	-2.7

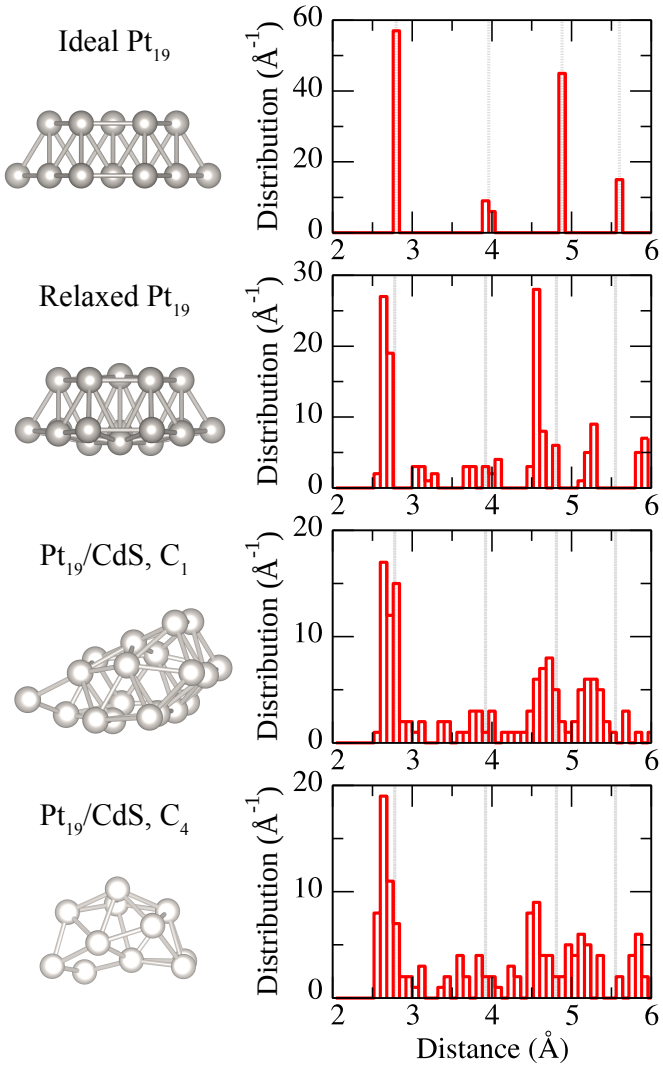

Figure 41: Side views (left) and radial distribution functions (right) of ideal, unsupported, and supported Pt_{19} on $CdS(10\bar{1}0)$ with adsorption configs. C_1 and C_4.

The formation of interfacial Pt-S and Pt-Cd bonds is accompanied by severe deformation of the substrate, and in some cases even the breaking of Cd-S bonds. In general, the surface atoms at the fringe of Pt_{19} are pulled upwards to form bonds with Pt atoms whereas those right underneath Pt_{19} are

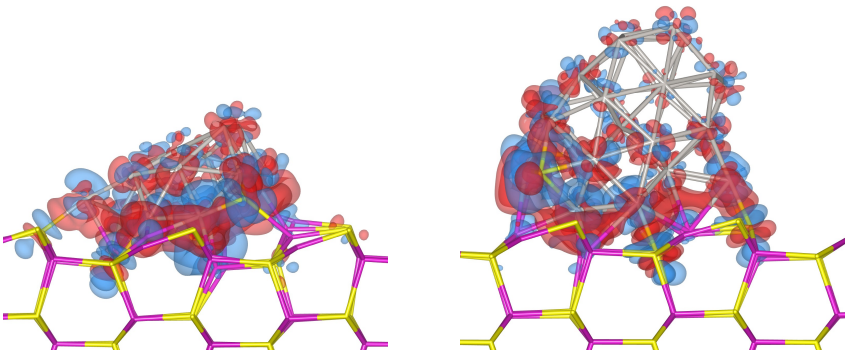

Figure 42: Electron density difference isosurfaces after the adsorption of Pt_{19} (C_1) (left) and Pt_{38} (T_1) (right) on CdS($10\bar{1}0$). Red and blue denote electron gain and loss, respectively, with isovalues of ± 0.02 eÅ^{-3}.

slightly pushed downwards as if the cluster is "sinking" into the substrate. In config. T_1, two surface S atoms are even pulled from the substrate and diffuse into Pt_{19}, similar to the observed atomic diffusion for Pt_{246} on CdS($10\bar{1}0$) from DFT molecular dynamics simulations [60]. As a result, $\Delta\mu_{CdS}$ is negative (-1.7 Debye). In contrast, the surface Cd atoms are pulled up away from the substrate in configs. C_1-C_5, leading to a positive $\Delta\mu_{CdS}$. For the adsorption configurations considered here, $E_{def,CdS}$ ranges from 1.8 eV to 11.3 eV and is roughly correlated with the magnitude of E_{ad} (Table 3), similar to the case of Pt_1 adsorption. The structure of the supported Pt_{19} cluster is also distorted and $E_{def,Pt}$ is about an order of magnitude smaller than $E_{def,CdS}$, showing less correlation with E_{ad}. Due to the atomic rearrangement of the cluster, the dipole moment of Pt_{19} ($\mu_{Pt_{19}}$) varies from -1.6 to nearly zero Debye, in contrast to the value of -1.8 Debye in the unsupported case. Interestingly, $E_{def,Pt}$ in C_2 is computed to be as small as 0.2 eV, despite the fact that the cluster is completely changed from the original 2D bilayer structure. In this case, the perturbation from the interfacial interactions is strong enough to drive the cluster out of its local energy minimum into an energetically more stable 3D shape. By subtracting $E_{def,CdS}$ and $E_{def,Pt}$ from E_{ad}, we obtain the "net" binding energies of 23.9, 13.9, 20.9, 9.1, 20.3, and 18.5 eV for C_1, C_2, C_3, C_4, C_5, and T_1, respectively, which directly reflects the strong cluster-substrate interaction strength in the adsorption geometries.

The electron density difference contour map for Pt_{19} on CdS($10\bar{1}0$) in config. C_1 is displayed in Fig. 42, which illustrate the complex re-distributions

of electrons in Pt cluster and at the top two layers of CdS. Bader charge analysis reveals that the supported Pt_{19} cluster gains 1.34 electrons, and the predicted direction of charge transfer is consistent with the larger number of Pt-Cd bonds than Pt-S bonds and the larger electronegativity difference between Pt (2.2) and Cd (1.7) than that between Pt and S (2.5). Indeed, for all the adsorption configurations examined here, $\mu_{\rm ind}$ is always negative, indicating an overall electron transfer from CdS to the cluster. $\Delta\mu_{\rm tot}$, as a sum of $\Delta\mu_{\rm CdS}$, $\mu_{\rm Pt_{19}}$ and $\mu_{\rm ind}$, varies from -1.0 to -1.6 Debye, indicating an overall *downward* shift of the local surface potential relative to the vacuum level.

Pt_{38}/CdS(10$\bar{1}$0). Below we present the computed adsorption characteristics of the Pt_{38}/CdS(10$\bar{1}$0), which enable us to examine the influence of cluster shape on adsorption geometry and energetics since Pt_{38} is 3D unlike the 2D Pt_{19}. As shown in Fig. 43, Pt_{38} preserves its shape except in config. T_1 in which it is severely deformed. Comparison between the radial distribution functions of Pt_{38} in T_1 and C_2 (Fig. 44) illustrates the significant structural distortion in T_1 as well as the largely preserved local crystallinity in C_2 (as in the other configurations). This observation is consistent with the small magnitude of $E_{\rm def,Pt}$ in all the configurations except T_1 (3.0 eV). The same trend is found in $E_{\rm def,Pt}$ and $E_{\rm ad}$, as listed in Table 4. The averaged bond lengths of Pt-Pt, Pt-S and Pt-Cd bonds are similar to the adsorption cases of a single Pt atom and Pt_{19}.

Table 4: Energetics and structural properties of Pt_{38}/CdS(10$\bar{1}$0). Definition of symbols is the same as in Table 2.

	C_1	C_2	C_3	T_1	T_2
$E_{\rm ad}$	-6.0	-5.7	-6.9	-10.7	-6.0
$E_{\rm def,CdS}$	6.8	0.8	7.7	10.5	2.9
$E_{\rm def,Pt}$	0.9	0.5	1.6	3.0	0.8
$\langle d_{\rm Pt-Pt}\rangle$ ($n_{\rm Pt-Pt}$)	2.75 (144)	2.74 (144)	2.74 (136)	2.71 (123)	2.74 (144)
$\langle d_{\rm Pt-S}\rangle$ ($n_{\rm Pt-S}$)	2.25 (4)	2.33 (4)	2.27 (6)	2.33 (11)	2.34 (6)
$\langle d_{\rm Pt-Cd}\rangle$ ($n_{\rm Pt-Cd}$)	2.89 (12)	2.84 (4)	2.85 (10)	2.82 (17)	2.77 (6)
$\Delta\mu_{\rm tot}$	-0.2	-3.4	-2.2	-3.4	-2.5
$\Delta\mu_{\rm CdS}$	1.8	0.1	0.3	-3.4	0.4
$\mu_{\rm Pt_{38}}$	-0.3	-0.5	0.0	-1.1	-0.5

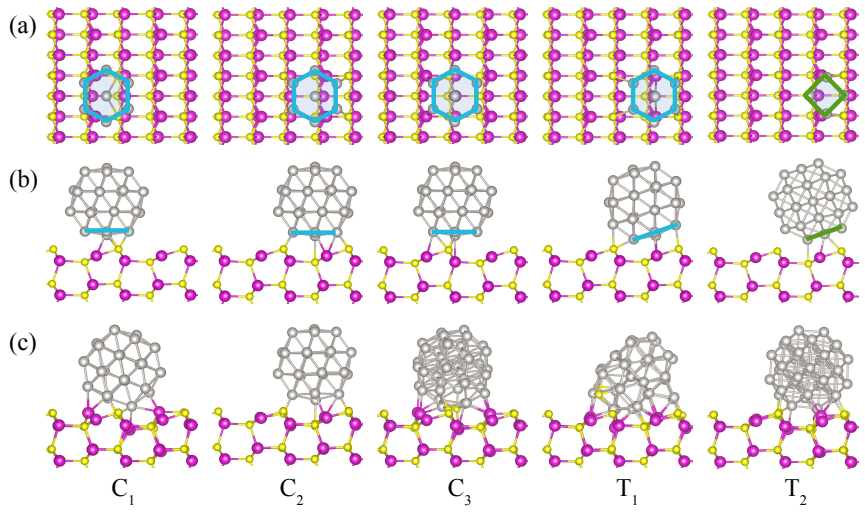

Figure 43: (a) Top and (b) side views of starting geometries of Pt_{38} on $CdS(10\bar{1}0)$. (c) Side views of relaxed geometries.

Although Pt_{19} and Pt_{38} have similar cross sectional area, the area directly in contact with the substrate is smaller for Pt_{38} due to its 3D shape, which directly influences the adsorption structure and strength. For example, the total numbers of Pt-Cd and Pt-S bonds formed at the interface are 23, 18, 24, 7, 24 and 18 for Pt_{19} in configs. C_1-C_5 and T_1, and 16, 8, 16 and 12 for Pt_{38} in configs. C_1-C_3 and T_2, respectively; as a result, smaller magnitude of E_{ad} is found for the latter in general. The only exception is the T_1 configuration, in which the tilted orientation allows the Pt_{38} cluster to interact with the substrate on more than one facet and form a total of 28 interfacial bonds, with $E_{ad} = -10.7$ eV. In contrast, the Pt_{19} cluster forms substantially fewer interfacial bonds (18 in total) with $E_{ad} = -8.6$ eV, although the initial position and orientation of Pt_{19} and Pt_{38} are identical except for the extra two (111) layers in Pt_{38} (see Figures S5 and S6). A closer inspection of the interface structure reveals that while two surface S atoms diffuse into the Pt_{19} as observed above, the same two S atoms migrate farther into the cluster surface in the case of Pt_{38} and one of them become completely detached from the substrate. On the other hand, the degree of "sinking" is larger for Pt_{38} than for Pt_{19}, allowing the former to come to closer proximity to the substrate atoms underneath and form more interfacial bonds. In order to examine whether such differences are caused by the existence of the

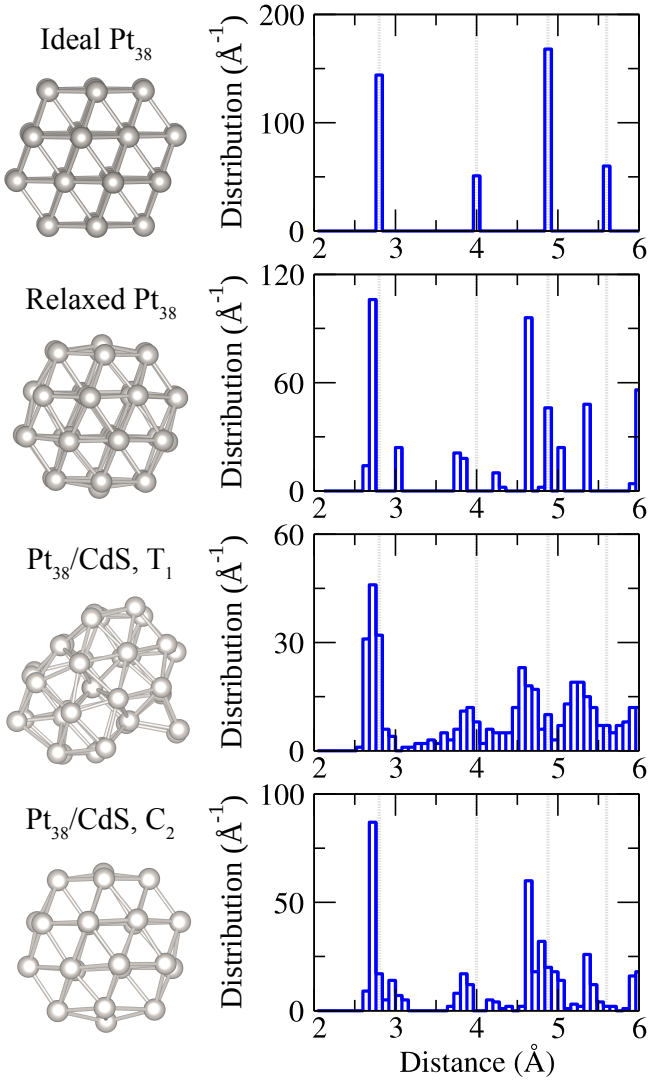

Figure 44: Side views (left) and radial distribution functions (right) of ideal, unsupported, and supported Pt_{38} on $CdS(10\bar{1}0)$ with adsorption configurations T_1 and C_2.

extra two top layers in Pt_{38}, which are not in contact with the substrate, we removed these atoms from Pt_{38} in config. T1 and relaxed the resulting Pt_{19}/CdS system. The final adsorption geometry of Pt_{19}, denoted as T_1' (see Fig. 40), has similar adsorption energy ($E_{ad} = -10.9$ eV) and similar number

of Pt-Cd and Pt-S bonds compared to Pt_{38} in config. T1. However, the lowering of E_{ad} is accompanied by severe deformation of both the substrate and the cluster, with the latter amounting to as high as 8 eV with substantially reduced number of Pt-Pt bonds (Table 3). Such a configuration, although thermodynamically stable, may not be kinetically accessible during deposition and post-deposition annealing of the Pt clusters on CdS. Overall, our calculations indicate that different initial geometry (cluster orientation and adsorption site) can lead to rather different adsorption structure and energetics, due to the strong and diverse bonding interactions at the interface.

Substantial changes in the charge distribution is observed between Pt_{38} and the CdS surface as illustrated in the electron density difference contour

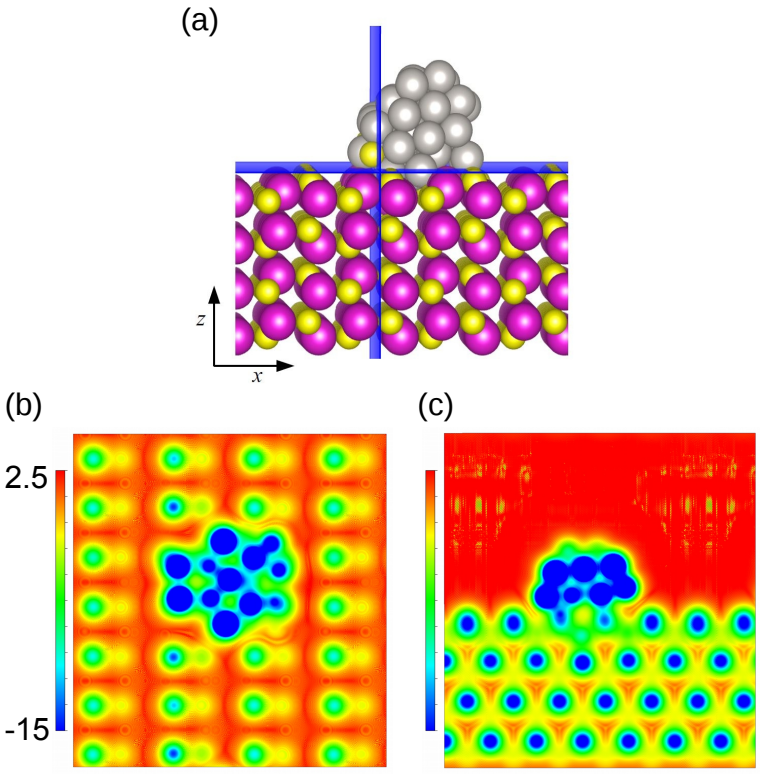

Figure 45: Contours of electrostatic surface potential of Pt_{38}/CdS on cutting planes that are normal to: (b) z-axis and (c) x-axis, as highlighted by blue in the structural model in (a). z- and x-axis are along the $[1\bar{0}10]$ and [0001] directions, respectively. Potential energies are in eV.

map for Pt_{38} on CdS($10\bar{1}0$) in config. T_1 (Fig. 42), and an electron gain of 1.38 electrons is predicted from Bader charge analysis for the supported Pt_{38} cluster. Similar to the case of Pt_{19}, $\Delta\mu_{tot}$ is always negative (Table 4), and correspondingly one expects a *downshift* of the surface potential and, in turn, the CdS band edges. Of course, the magnitude of such shift depends not only on the adsorption configuration but also on the coverage of clusters on the surface.

Contour plots of the calculated effective surface potential of Pt_{38}/CdS($10\bar{1}0$) are shown in Fig. 45, which clearly demonstrates the variation of surface potential near the region where the cluster comes into contact with the substrate.

Electronic Structure of Pt/CdS Interface. Finally, we examine the electronic structure of the Pt/CdS interface, in particular near the Fermi level. While a quantitatively accurate prediction of the energy level alignment at the interface may require the use of more advanced methods such as the GW method [77], the electronic structure predicted at the DFT level already provides useful insight on the the electronic coupling between the adsorbed Pt cluster and the CdS substrate. The projected density of states (PDOS) of Pt_{38}/CdS($10\bar{1}0$) in config. T_1 (Fig. 46) clearly indicates metallic behavior via the non-vanishing density of states at E_F, which is in between the bulk-like band edges, primarily stemming from states on the Pt cluster. A further decomposition onto individual atoms reveals that the small but finite PDOS of CdS near E_F comes mainly from the surface S atoms bonded

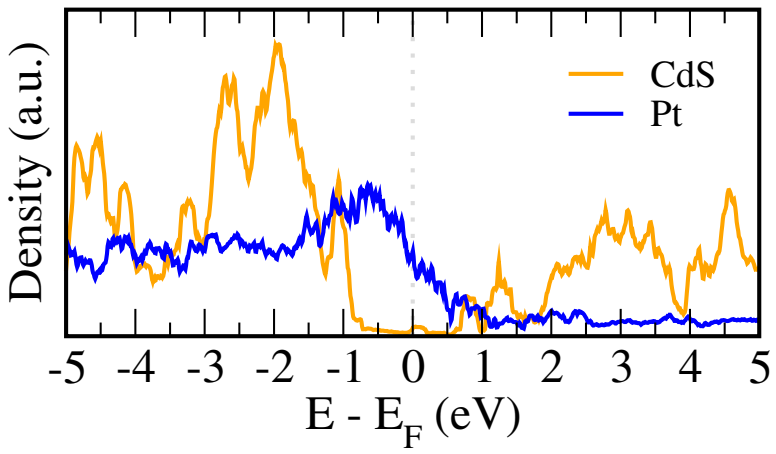

Figure 46: Projected density of states of Pt_{38}/CdS($10\bar{1}0$) in config. T_1.

to Pt. In contrast, surface Cd atoms bonded to Pt show only minor influence. The overall shape and fine features of the PDOS of CdS differ from that of the clean CdS($10\bar{1}0$) surface (Fig. 37), as a result of the severe structural deformation due to the adsorption of Pt_{38} as well as the orbital hybridization with the bonded Pt atoms.

In addition, the deformation of the supported Pt cluster results in changes in its HOMO and LUMO levels, which can be approximated by the negatives of IP and EA. Table 5 show the computed vertical IP and EA of unsupported Pt_{19} and Pt_{38} clusters and of those in adsorption configurations with the maximum and minimum structural deformation. The variation in IP and EA values is within 0.2 eV except for Pt_{38} in config. T_1, which has a decrease of EA of as large as 0.6 eV. Overall, no clear correlation is found between the change in IP or EA values and the degree of deformation. For all adsorption configurations examined here for Pt_{19} and Pt_{38} , the LUMO levels are always higher than absolute electrode potential energy of the standard hydrogen electrode (-4.44 $\pm$0.02 eV) [78], implying that their positions may be appropriate for reducing water. Whether the combined system of Pt cluster on CdS is able to split water under visible light will depend also on how the EA and IP values of the adsorbed Pt clusters, as well as the band edges of CdS substrate, will be further modified when electronic coupling at the interface is fully taken into consideration. Other factors, such as the aqueous environments where the device is in operation, also plays important roles in determining the energy level alignment at the interface [79, 80]. Nevertheless, it is already clear from our DFT calculations that strong structural and electronic interactions occur at the Pt/CdS interface and an oversimplified

Table 5: Computed vertical ionization potential (IP) and vertical electron affinity (EA) of isolated Pt clusters in both unsupported and supported geometries. Adsorption configurations with largest $E_{\mathrm{def,Pt}}$ (Pt_{19}@C_1, Pt_{38}@T_1), smallest $E_{\mathrm{def,Pt}}$ (Pt_{19}@C_4, Pt_{38}@C_2) are chosen (see Table 4). All energies are in eV.

	Pt_{19}			Pt_{38}		
	Unsupported	C_1	C_4	Unsupported	T_1	C_2
IP	6.81	6.74	6.61	6.77	6.61	6.56
EA	3.73	3.74	3.56	4.19	3.57	4.27

picture based on the energy levels of the bulk substrate (or clean surface) and unsupported clusters is not sufficient to describe the electronic structure of the interface.

4.4 Conclusions

In summary, we have investigated both unsupported and supported Pt clusters on the nonpolar CdS($10\bar{1}0$) surface using first-principles DFT calculations. The unsupported 2D bilayer and 3D Pt clusters show similar trends in cohesive energy and electron addition/removal energies (IP and EA) as functions of the cluster size. Upon adsorption on the CdS surface, the Pt clusters form multiple covalent bonds with the substrate atoms with magnitude of E_{ad} up to 4 eV (Pt_1), 10 eV (Pt_{19}) and 11 eV (Pt_{38}), accompanied by severe structural deformation of the substrate. The supported clusters undergo changes in both atomic structures and charged excitation energies. Comparative studies of the adsorption of a 2D bilayer Pt_{19} cluster and a 3D Pt_{38} cluster reveals considerable influence on the adsorption characteristics from the cluster size, shape, adsorption site and orientation, In addition, substantial charge transfer occurs at the interface, resulting in local shifts of the surface potential and band edges. The surface electronic structure is further modified due to the structural deformation of the substrate and the orbital hybridization at the cluster/substrate interface. While a higher level of theory may be necessary to accurately describe the interfacial energy level alignment and gain further insight into the photocatalytic behavior at the interface, the adsorption geometry and electronic structure predicted from DFT provides valuable insights on the bonding interactions at the interfaces beyond a simple picture based on energy levels of unsupported Pt nanoparticles and bulk or clean surfaces of CdS .

References

[1] Ph. Buffat and J-P. Borel. Size effect on the melting temperature of gold particles. *Physical Review A*, 13(6):22872298, Jun 1976.

[2] F. C. Nix and D. MacNair. The thermal expansion of pure metals: Copper, gold, aluminum, nickel, and iron. *Phys. Rev.*, 60:597–605, Oct 1941.

[3] John W. Stone, Patrick N. Sisco, Edie C. Goldsmith, Sarah C. Baxter, and Catherine J. Murphy. Using gold nanorods to probe cell-induced collagen deformation. *Nano Lett.*, 7(1):116119, Jan 2007.

[4] Joo Conde, Gonalo Doria, and Pedro Baptista. Noble metal nanoparticles applications in cancer. *J. of Drug Deliv.*, 2012:112, 2012.

[5] Qiyuan Wu, Shangmin Xiong, Peichuan Shen, Shen Zhao, Yan Li, Dong Su, and Alexander Orlov. Exceptional activity of sub-nm pt clusters on cds for photocatalytic hydrogen production: a combined experimental and first-principles study. *Catal. Sci. Technol.*, 5(4):20592064, 2015.

[6] Simon J L Billinge and Igor Levin. The problem with determining atomic structure at the nanoscale. *Science (New York, N.Y.)*, 316(5824):561–5, April 2007.

[7] Matthew J. Cliffe, Martin T. Dove, D. A. Drabold, and Andrew L. Goodwin. Structure determination of disordered materials from diffraction data. *Physical Review Letters*, 104(12), Mar 2010.

[8] Neil W. Ashcroft and N. David Mermin. *Solid State Physics*. Brooks Cole, Boston, MA, 1976.

[9] William F. Coleman and Kieran F. Lim. The effect of anharmonicity on diatomic vibration: A spreadsheet simulation. *Journal of Chemical Education*, 82(8):1263, Aug 2005.

[10] Esel'son V. B. Manzhelii V. G. Udovidchenko B. G. Soldatov A. V. Aleksandrovskii, A. N. and B. Sundqvist. Negative thermal expansion of fullerite c[sub 60] at liquid helium temperatures. *Low Temp. Phys.*, 23(11):943, Nov 1997.

[11] W.-H. Li, S. Y. Wu, C. C. Yang, S. K. Lai, K. C. Lee, H. L. Huang, and H. D. Yang. Thermal contraction of au nanoparticles. *Phys. Rev. Lett.*, 89:135504, Sep 2002.

[12] T. Comaschi, A. Balerna, and S. Mobilio. Temperature dependence of the structural parameters of gold nanoparticles investigated with exafs. *Phys. Rev. B*, 77(7), Feb 2008.

[13] Y. Q. Wang, W. S. Liang, and C. Y. Geng. Shape evolution of gold nanoparticles. *J Nanopart Res*, 12(2):655661, Mar 2009.

[14] G. Wulff. On the question of speed of growth and dissolution of crystal surfaces. *Zeitschrift fur Krystallographie und Mineralogie, 34, 5/6, pp 449-530, 1901*, 5/6(34):449–530, 1901.

[15] H. W. Sheng, M. J. Kramer, A. Cadien, T. Fujita, and M. W. Chen. Highly optimized embedded-atom-method potentials for fourteen fcc metals. *Phys. Rev. B*, 83:134118, Apr 2011.

[16] Shangmin Xiong, Eric B. Isaacs, and Yan Li. Adsorption characteristics and size/shape dependence of pt clusters on the cds surface. *The Journal of Physical Chemistry C*, 119(9):48344842, Mar 2015.

[17] Richard M. Martin. *Electronic Structure*. Cambridge University Press, Cambridge, UK, 2004.

[18] L. H. Thomas. The calculation of atomic fields. *Mathematical Proceedings of the Cambridge Philosophical Society*, 23(05):542, Jan 1927.

[19] Enrico Fermi. Un metodo statistico per la determinazione di alcune priopriet dell'atomo. *Rend. Accad. Naz. Lincei*, (6):602–607, 1927.

[20] P. A. M. Dirac. Note on exchange phenomena in the thomas atom. *Mathematical Proceedings of the Cambridge Philosophical Society*, 26(03):376, Jul 1930.

[21] D. M. Ceperley and B. J. Alder. Ground state of the electron gas by a stochastic method. *Phys. Rev. Lett.*, 45:566–569, Aug 1980.

[22] John P. Perdew and Kieron Burke. Comparison shopping for a gradient-corrected density functional. *International Journal of Quantum Chemistry*, 57(3):309319, Feb 1996.

[23] P. S. Svendsen and U. von Barth. Gradient expansion of the exchange energy from second-order density response theory. *Phys. Rev. B*, 54:17402–17413, Dec 1996.

[24] John P. Perdew, Kieron Burke, and Matthias Ernzerhof. Generalized gradient approximation made simple. *Phys. Rev. Lett.*, 77(18):3865–3868, Oct 1996.

[25] Peter Schwerdtfeger. The pseudopotential approximation in electronic structure theory. *ChemPhysChem*, 12(17):31433155, Aug 2011.

[26] G. B. Bachelet, D. R. Hamann, and M. Schlter. Pseudopotentials that work: From h to pu. *Physical Review B*, 26(8):41994228, Oct 1982.

[27] G. Kresse and J. Hafner. Ab initio molecular dynamics for liquid metals. *Phys. Rev. B*, 47(1):558–561, Jan 1993.

[28] G. Kresse and J. Hafner. Ab initio molecular-dynamics simulation of the liquid-metal-amorphous-semiconductor transition in germanium. *Phys. Rev. B*, 49(20):14251–14269, May 1994.

[29] J. E. Jones. On the determination of molecular fields. ii. from the equation of state of a gas. *Proc. R. Soc. A*, 106(738):463477, Oct 1924.

[30] Murray S. Daw and M. I. Baskes. Embedded-atom method: Derivation and application to impurities, surfaces, and other defects in metals. *Phys. Rev. B*, 29(12):64436453, Jun 1984.

[31] Julian D. Gale and Andrew L. Rohl. The general utility lattice program (gulp). *Molecular Simulation*, 29(5):291341, May 2003.

[32] Fabrizio Cleri and Vittorio Rosato. Tight-binding potentials for transition metals and alloys. *Phys. Rev. B*, 48:22–33, Jul 1993.

[33] Furio Ercolessi and James B. Adams. Interatomic potentials from first-principles calculations: the force-matching method. *Philos. Mag. Lett. A*, 58:213, 1988.

[34] David J Wales. Energy landscapes: some new horizons. *Current Opinion in Structural Biology*, 20(1):310, Feb 2010.

[35] Peter Brommer and Franz Ghler. Potfit: effective potentials from ab initio data. *Modelling Simul. Mater. Sci. Eng.*, 15(3):295304, Mar 2007.

[36] John G. Herriot and Christian H. Reinsch. Algorithm 600: translation of algorithm 507. procedures for quintic natural spline interpolation. *TOMS*, 9(2):258259, Jun 1983.

[37] A. K. Rappe, C. J. Casewit, K. S. Colwell, W. A. Goddard, and W. M. Skiff. Uff, a full periodic table force field for molecular mechanics and molecular dynamics simulations. *Journal of the American Chemical Society*, 114(25):1002410035, Dec 1992.

[38] M. W. Finnis and J. E. Sinclair. A simple empirical n -body potential for transition metals. *Philosophical Magazine A*, 50(1):4555, Jul 1984.

[39] A. P. Sutton and J.Chen. Long-range finnis-sinclair potentials. *Philos. Mag. Lett.*, 61(3):139–146, 1990.

[40] R. A. Johnson. Alloy models with the embedded-atom method. *Phys. Rev. B*, 39:12554–12559, Jun 1989.

[41] Raju P. Gupta. Lattice relaxation at a metal surface. *Phys. Rev. B*, 23:6265–6270, Jun 1981.

[42] A P Sutton, M W Finnis, D G Pettifor, and Y Ohta. The tight-binding bond model. *Journal of Physics C: Solid State Physics*, 21(1):35, 1988.

[43] D. J. Chadi. (110) surface atomic structures of covalent and ionic semiconductors. *Phys. Rev. B*, 19:2074–2082, Feb 1979.

[44] B. J. Alder and T. E. Wainwright. Studies in molecular dynamics. i. general method. *J. Chem. Phys.*, 31(2):459, 1959.

[45] Steve Plimpton. Fast parallel algorithms for short-range molecular dynamics. *Journal of Computational Physics*, 117(1):119, Mar 1995.

[46] W. J. Huang, R. Sun, J. Tao, L. D. Menard, R. G. Nuzzo, and J. M. Zuo. Coordination-dependent surface atomic contraction in nanocrystals revealed by coherent diffraction. *Nat Mater*, 7(4):308313, Mar 2008.

[47] S. Kümmel, J. Akola, and M. Manninen. Thermal expansion in small metal clusters and its impact on the electric polarizability. *Phys. Rev. Lett.*, 84:3827–3830, Apr 2000.

[48] Yan Li, Giulia Galli, and Franois Gygi. Electronic structure of thiolate-covered gold nanoparticles: Au102(mba)44. *ACS Nano*, 2(9):1896–1902, 2008.

[49] Yang-Hee Lee, Gunn Kim, Minwoong Joe, Ji-Hoon Jang, Juyeong Kim, Kwang-Ryeol Lee, and Young-Uk Kwon. Enhancement of electrocatalytic activity of gold nanoparticles by sonochemical treatment. *Chem. Commun.*, 46(31):5656–5658, 2010.

[50] Kenji Koga, Tamio Ikeshoji, and Ko-ichi Sugawara. Size- and temperature-dependent structural transitions in gold nanoparticles. *Phys. Rev. Lett.*, 92(11):115507, Mar 2004.

[51] M. Walter, J. Akola, O. Lopez-Acevedo, P. D. Jadzinsky, G. Calero, C. J. Ackerson, R. L. Whetten, H. Gronbeck, and H. Hakkinen. A unified view of ligand-protected gold clusters as superatom complexes. *Proc. Natl. Acad. Sci.*, 105(27):9157–9162, Jul 2008.

[52] Vladimir Komanicky, Hakim Iddir, Kee-Chul Chang, Andreas Menzel, Goran Karapetrov, Daniel Hennessy, Peter Zapol, and Hoydoo You. Shape-dependent activity of platinum array catalyst. *J. Am. Chem. Soc.*, 131(16):5732–5733, Apr 2009.

[53] Peichuan Shen, Shen Zhao, Dong Su, Yan Li, and Alexander Orlov. Outstanding activity of sub-nm au clusters for photocatalytic hydrogen production. *Appl. Catal., B*, 126:153–160, Sep 2012.

[54] Kaifeng Wu, Haiming Zhu, Zheng Liu, William Rodríguez-Córdoba, and Tianquan Lian. Ultrafast charge separation and long-lived charge separated state in photocatalytic cds-pt nanorod heterostructures. *J. Am. Chem. Soc.*, 134(25):10337–10340, Jun 2012.

[55] Florian F. Schweinberger, Maximilian J. Berr, Markus Döblinger, Christian Wolff, Kai E. Sanwald, Andrew S. Crampton, Claron J. Ridge, Frank Jäckel, Jochen Feldmann, Martin Tschurl, and et al. Cluster size effects in the photocatalytic hydrogen evolution reaction. *J. Am. Chem. Soc.*, pages 13262–13265, Aug 2013.

[56] F. Vila, J. Rehr, J. Kas, R. Nuzzo, and A. Frenkel. Dynamic structure in supported pt nanoclusters: Real-time density functional theory and x-ray spectroscopy simulations. *Phys. Rev. B*, 78(12):121404, Sep 2008.

[57] F. Behafarid, L. K. Ono, S. Mostafa, J. R. Croy, G. Shafai, S. Hong, T. S. Rahman, Simon R. Bare, and B. Roldan Cuenya. Electronic properties and charge transfer phenomena in pt nanoparticles on γ-al2o3: Size, shape, support, and adsorbate effects. *Phys. Chem. Chem. Phys.*, 14(33):11766–11779, 2012.

[58] Long Li, Lin-Lin Wang, Duane D. Johnson, Zhongfan Zhang, Sergio I. Sanchez, Joo H. Kang, Ralph G. Nuzzo, Qi Wang, Anatoly I. Frenkel, Jie Li, and et al. Noncrystalline-to-crystalline transformations in pt nanoparticles. *J. Am. Chem. Soc.*, 135(35):13062–13072, Sep 2013.

[59] Yandong Ma, Ying Dai, Wei Wei, Xianghong Liu, and Baibiao Huang. Ag adsorption on cd-terminated cds (0001) and s-terminated cds (0001) surfaces: First-principles investigations. *J. Solid State Chem.*, 184(4):747–752, Apr 2011.

[60] S. Dag and Lin-Wang Wang. Atomic and electronic structures of nano- and amorphous cds/pt interfaces. *Phys. Rev. B*, 82:241303, Dec 2010.

[61] G. Ramos-Sanchez and P. B. Balbuena. Interactions of platinum clusters with a graphite substrate. *Phys. Chem. Chem. Phys.*, 15(28):11950–11959, 2013.

[62] Maximilian J. Berr, Florian F. Schweinberger, Markus Döblinger, Kai E. Sanwald, Christian Wolff, Johannes Breimeier, Andrew S. Crampton, Claron J. Ridge, Martin Tschurl, Ulrich Heiz, and et al. Size-selected subnanometer cluster catalysts on semiconductor nanocrystal films for atomic scale insight into photocatalysis. *Nano Lett.*, 12(11):5903–5906, Nov 2012.

[63] P. E. Blöchl. Projector augmented-wave method. *Phys. Rev. B*, 50(24):17953–17979, Dec 1994.

[64] Charles Kittel. *Introduction to Solid State Physics*. Wiley, New York, 2004.

[65] Edoardo Aprá and Alessandro Fortunelli. Density-functional calculations on platinum nanoclusters: Pt_{13}, pt_{38}, and pt_{55}. *J. Phys. Chem. A*, 107(16):2934–2942, Apr 2003.

[66] Li Xiao and Lichang Wang. Structures of platinum clusters: planar or spherical? *J. Phys. Chem. A*, 108(41):8605–8614, Oct 2004.

[67] J. E. Sansonetti. Handbook of basic atomic spectroscopic data. *J. Phys. Chem. Ref. Data*, 34(4):1559–2259, 2005.

[68] Ren Bilodeau, Michael Scheer, Harold Haugen, and Robert Brooks. Near-threshold laser spectroscopy of iridium and platinum negative ions: Electron affinities and the threshold law. *Phys. Rev. A*, 61(1):012505, Dec 1999.

[69] A. W. Stevenson, M. Milanko, and Z. Barnea. Anharmonic thermal vibrations and the position parameter in wurtzite structures. i. cadmium sulphide. *Acta Cryst B*, 40(6):521–530, Dec 1984.

[70] D. Lincot and Gary Hodes. *Chemical Solution Deposition of Semiconducting and Non-Metallic Films (Proceedings Volume, 2003-32)*. The Electrochemical Society, New Jersey, 2006.

[71] M. Huda, Manish Niranjan, B. Sahu, and Leonard Kleinman. Effect of spin-orbit coupling on small platinum nanoclusters. *Phys. Rev. A*, 73(5):053201, May 2006.

[72] M. Seidl, M.E. Spina, and M. Brack. Semiclassical variational calculation of liquid-drop model coefficients for metal clusters. *Zeitschrift fr Physik D Atoms, Molecules and Clusters*, 19(4):101–103, 1991.

[73] Nicholas E. Singh-Miller and Nicola Marzari. Surface energies, work functions, and surface relaxations of low-index metallic surfaces from first principles. *Phys. Rev. B*, 80:235407, Dec 2009.

[74] A.S. Barnard and H. Xu. First principles and thermodynamic modeling of cds surfaces and nanorods. *J. Phys. Chem. C*, 111(49):18112–18117, Dec 2007.

[75] Vincenzo Fiorentini and M Methfessel. Extracting convergent surface energies from slab calculations. *J. Phys.: Condens. Matter*, 8(36):6525–6529, 1996.

[76] R.F. Minibaev, A.A. Bagatur′yants, and D.I.M Bazhanov. First-principles investigation of the structure and electronic properties of cds/cdse/cds and cds/cdte/cds quantum wells using a slab approximation. *Nanotechnol. Russ.*, 5(3-4):191–197, 2010.

[77] Lars Hedin. New method for calculating the one-particle green's function with application to the electron-gas problem. *Phys. Rev.*, 139:A796–A823, 1965.

[78] A. D. McNaught and A. Wilkinson. *UPAC. Compendium of Chemical Terminology, 2nd Ed.* Blackwell Scientific Publications, Oxford, 1997.

[79] Yabi Wu, M. K. Y. Chan, and G. Ceder. Prediction of semiconductor band edge positions in aqueous environments from first principles. *Phys. Rev. B*, 83:235301, Jun 2011.

[80] Neerav Kharche, James T. Muckerman, and Mark S. Hybertsen. First-principles approach to calculating energy level alignment at aqueous semiconductor interfaces. *Phys. Rev. Lett.*, 113:176802, Oct 2014.